8-2018

Investigation of Electrochemically Li-ion Active Materials for Li-ion Batteries

Daw Gen Lim
Purdue University

INVESTIGATION OF ELECTROCHEMICALLY LI-ION ACTIVE MATERIALS

FOR LI-ION BATTERIES

A Dissertation

Submitted to the Faculty

of

Purdue University

by

Daw Gen Lim

In Partial Fulfillment of the

Requirements for the Degree

of

Doctor of Philosophy

August 2018

Purdue University

West Lafayette, Indiana

THE PURDUE UNIVERSITY GRADUATE SCHOOL
STATEMENT OF DISSERTATION APPROVAL

Dr. Vilas G. Pol, Co - Chair

    School of Chemical Engineering

Dr. Jeffrey P. Youngblood, Co - Chair

    School of Materials Science and Engineering

Dr. Kejie Zhao

    School of Mechanical Engineering

Dr. Sebastian Osswald

    School of Materials Science and Engineering

Approved by:

    Dr. David Bahr

        Head of the School Graduate Program

To my parents,

Gwendolin Hooi Lee Neoh and Meng Ming Lim

my sister, Win Gel Lim

For their endless love and support

ACKNOWLEDGMENTS

Finally, many thanks to my friends who have been by my side, in particularly, Gregory Wen-Che Chang, Yumeng Wu, and Tony Ding-Wen Chung for their endless encouragement, support, and friendship over the years at Purdue University.

TABLE OF CONTENTS

LIST OF TABLES

LIST OF FIGURES

ABSTRACT

Lim, Daw Gen PhD, Purdue University, August 2018. Investigation of Electrochemically Li-ion Active Materials for Li-ion Batteries. Major Professors: Vilas G. Pol and Jeffrey P. Youngblood.

Being the battery of the 21st century, Li-ion batteries have been making headway towards replacing traditional medium to large scale energy storage devices. Recent applications ranging from EVs to grid-level energy storage, have driven the design criteria of Li-ion batteries to evolve at a rapid pace. Three major goals are low cost, high electrochemical performance, and improved safety. New targets set by the DOE to make Li-ion batteries more competitive in their new market sectors have been to decrease cost to US\$ 125 kWh^{-1} and increase gravimetric and volumetric energy density to 235 Wh kg^{-1} and 500 Wh L^{-1}, respectively [1]. This thesis presents works on the three major components of a Li-ion battery: sustainable wheat derived-carbon anodes, high capacity V_2O_5|Graphene-nanoplatelets (GNPs) composite cathodes, and rare earth nickelates (specifically $SmNiO_3$ as a potential solid-state electrolyte for improved safety.

Systematic solid-state processing, structural, and electrochemical studies were conducted on wheat-derived carbons. Coupling carbonization temperatures and structural evolution of biomass-derived carbons (in this case wheat), lithium insertion properties can be tuned, to create a high capacity and sustainable anode material. An optimal condition presents itself at a carbonization temperature of 600°C with a stable lithiation capacity of 390 mAh g^{-1}.

In the Li-ion cell, the limiting factor in the total output capacity (mAh g^{-1}) is governed mainly by the cathode materials, as cathode materials tend to be lithium-based transitional metal oxides (high density compared to anode materials). Having

one of the highest lithium storage capacity, V_2O_5 is a cathode material that suffers from low electronic conductivity and particle fragmentation upon continuous lithium insertion and extraction. In this work, sonochemistry is utilized in the synthesis of V_2O_5|Graphene-nanoplatelets (GNPs) composites to improve electronic conductivity and kinetics of lithium-insertion and extraction. Surface modification of the graphene nanoplatelets during sonication of GNPs allows for *in situ* growth of V_2O_5 nanoparticles. With the size reduction of the V_2O_5 particles and the conductive GNPs backbone, the composite achieved 248 mAh g^{-1} specific cathode capacity; retaining 83% of initial capacity after 50 cycles.

Part 1 and 2 of this study illustrate strategies to create a low-cost and high electrochemical performance Li-ion battery via sustainable material implementation, structural and morphology control, and composite formation. The third part studies the electrochemical properties of perovskite rare-earth nickelates (specifically $SmNiO_3$) and its' integration as a solid-state electrolyte in an all-solid-state lithium-ion battery. Upon insertion of Li$^+$ ion, $SmNiO_3$ undergoes Mott-transition, simultaneously allowing for a large amount of mobile Li$^+$ to be stored at the interstitial sites (approaching a ratio of one dopant per unit-cell). The combination of a lattice expansion ($\sim$10% increase) and the interstitial doping creates a perfect condition for fast Li$^+$ conduction with reduced activation energy. Initial efforts to integrate $LiSmNiO_3$ in a solid-state-cell with $LiCoO_2$|$LiSmNiO_3$|Si configuration results with initial charging capacity of 1338 mAh g^{-1}.

1. INTRODUCTION

1.1 Dissertation Organization

This dissertation focuses on the development of electrochemically active materials for potential applications in Li-ion batteries. In this section, the layout of the dissertation will be introduced. For section 1.2, the working principles of the lithium-ion battery will be presented. Follow by a discussion of what I believe to be the current Li-ion batteries trifecta, which builds the motivation for the research presented in this thesis.

Chapter 2 titled *Lithium Storage in Structurally Tunable Carbon Anode Derived from Sustainable Source*, introduces the development of various carbon anodes derived from sustainable biomass for lithium-ion secondary batteries. The chapter reports on the carbonization temperature effects on physical properties of wheat derived carbons. Comparative studies on the electrochemical performance of the as-derived carbons are then conducted. Chapter 2 also identifies a carbonization temperature for enhanced lithiation capacities, as well as future strategies to improve the electrochemical performance for the wheat-derived carbons.

Chapter 3 titled *Tailored Sonochemical Anchoring of Nano-Sized V_2O_5 Cathode Particles on Graphene Nanoplatelets for Improved Lithium-Ion Insertion*, focuses on an electrochemically active oxide cathode material (V_2O_5), with a high lithiation capacity; It then discusses on the various shortcomings and existing strategies to overcome the material shortcomings in existing literature. The chapter then reports on the usage of sonochemical process to synthesize a high capacity V_2O_5|Graphene nanoplatelets cathode composite material to improve electrical conductivity and diffusivity, for high rate capability and improved capacity.

Chapter 4 introduces thin-film perovskite rare earth nickelates, in particular $SmNiO_3$ (SNO) and its interaction with lithium-ion. The resulting Mott-transition phenomena of the SNO, which is induced by the electrochemically inserted Li^+ dopants is also elucidated. The derived electrical and electrochemical properties from the Li-ion interaction with SNO is then presented, in particular the lithium ionic conductivity. Evidence of the Mott transition behavior induced by alkali-ion species (namely Li^+ and Na^+ ions) on other perovskite rare earth nickelates are also presented. Finally integration of the SNO thin-film as a potential solid-state electrolyte is also demonstrated.

1.2   Working Principles of Li-ion Batteries

The primary components that make up a battery are the anode (negative electrode), the cathode (positive electrode), and the electrolyte; additional components include the separator and the current collectors (typically aluminum for cathode and copper for anode). Anode and cathode must be able to react with Li^+ ions reversibly, to allow the battery to work as a rechargeable (secondary) battery. The separator in a conventional liquid electrolyte cell acts as a solid electronic insulator barrier to prevent the two electrodes from short circuiting, at the same time allowing the permeation of electrolyte and the Li^+ ions. The current collector in the cell acts as an interface between the outside environment and the electrode by directing charges through an external circuit. The lithium ion battery system utilizes the oxidation and reduction processes that occur in the electrodes, to drive electronic charge through the external circuit during a discharge process, the process is reverse during charging. The phenomena for the working principle of Li-ion batteries is described as the "rocking chair" model (Figure 1.1), where Li-ions are being shuttled back and forth between the cathode (+) and the anode (−) [2,3].
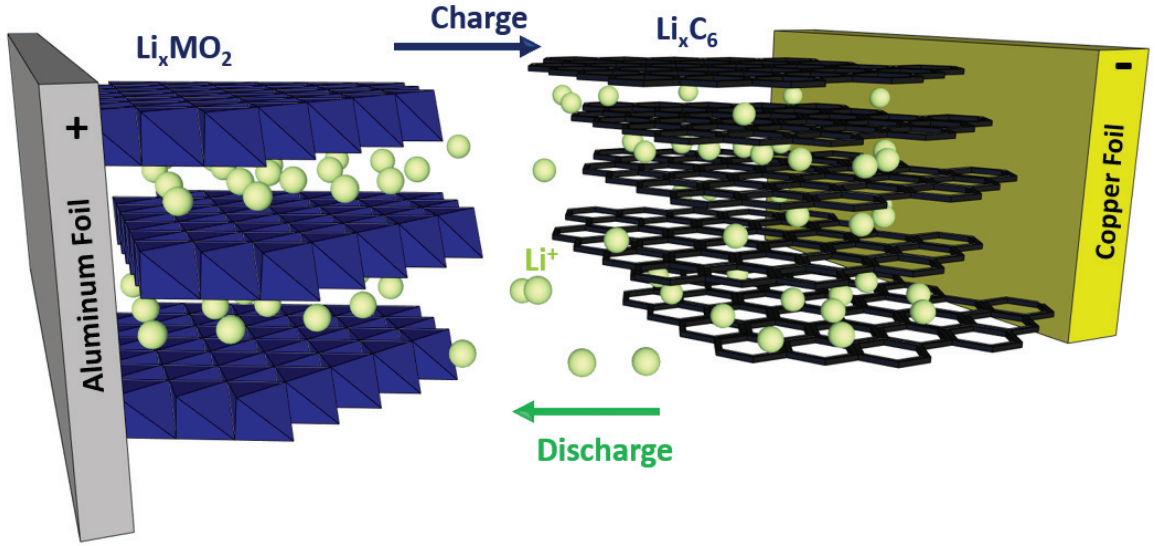
Fig. 1.1.: Schematic of the "rocking chair" model for a typical Li-ion battery, including the illustration of all the major components of the Li-ion battery, which consist of a cathode that is typically a lithium-based transition metal oxide; an anode that is typically graphitic carbon; and their respective current collectors aluminum and copper.

1.2.1 Electrochemical Potential

During the discharge process, the negative electrode loses an electron (oxidizes), producing Li^+ ions; during which the positive electrode is reduced. The cell is then driven by the chemical potential between the cathode and the anode. The chemical potential of the cell can be defined by the following [4]:

$$\mu_i = \left(\frac{\partial G}{\partial N_i} \right)_{T,P} \tag{1.1}$$

which is the change in the Gibb's free energy with respect to the change in the ith species of the electrode particle at constant temperature and pressure. The coulombic forces govern the electrons that are traveling through the closed external circuit. The electric potential and chemical potential of the cell are then related by the following:

$$-eV_{oc} = \mu_{cathode} - \mu_{anode} \tag{1.2}$$

where the electric potential of the electrode is the quotient of the cathode and anode's chemical potential difference (in eV) per electron charge (e). This essentially describe the state of discharge. For a charge process, a reversed external electric potential is applied, the cathode will oxides and the anode will be reduced, electrons flow in a reverse direction, and the Li$^+$ dissociates from the cathode, flowing back to the anode. Ideally the materials should transition into their original states. The repeat of this reversible process is the "rocking chair" process.

1.2.2 Electrochemical Transport

The electrochemical transport of Li$^+$ in an electrochemically active system is govern by the following equation [5]:

$$\frac{\partial c}{\partial t} = \nabla \cdot \overset{\leftrightarrow}{D} \nabla c + \nabla \cdot \frac{zFc}{RT} \overset{\leftrightarrow}{D} \nabla \phi \tag{1.3}$$

$$\frac{\partial \rho}{\partial t} = \nabla \cdot \overset{\leftrightarrow}{\sigma} \nabla \phi + \nabla \cdot \frac{zFc}{RT} \overset{\leftrightarrow}{D} \nabla c \tag{1.4}$$

where c is the concentration of lithium, $\overset{\leftrightarrow}{D}$ is the lithium diffusivity tensor, ρ is the electrical charge density, σ is the electrical conductivity, ϕ is the electrostatic potential, t is the time, z is the valence charge of the diffusing ionic species, F is the Faraday's constant, R is the gas constant, and T is the absolute temperature. Equations 1.3 and 1.4 corresponds to a set of modified coupled Cahn-Hilliard equations and simultaneously describe mass and charge conservation within the electrochemically active materials.

As described previously, during charge/discharge, the Li^+ ions that dissolve in the electrolyte recombine with the electrons at the electrode|electrolyte interface (cathode during charge and anode during discharge):

$$Li^+ + e^- \rightleftharpoons Li$$
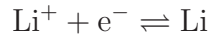
The rate of the interfacial reaction at the electrode is then described by the Butler-Volmer relation [6]:

$$J = i_\circ\left(e^{\frac{\alpha_a F \eta}{RT}} - e^{-\frac{\alpha_c F \eta}{RT}}\right) \tag{1.5}$$

where J is the current density, α_a is the anodic reaction empirical constant, α_c is the cathodic reaction empirical constant, and η is the local over-potential. The interfacial reaction then depends on the exchange current density at the interface $i_\circ$:

$$i_\circ = F k_r (c_s - c)^{\alpha_a} c^{\alpha_c} \tag{1.6}$$

where k_r is the electrochemical reaction rate constant and c_s is the lithium solubility limit of the electrode material.

1.2.3 Key Figures of Merit and Parameters in Designing and Evaluating Battery Materials

In the previous section, the electrode's thermodynamics and reaction kinetics were described. This section will introduce the various parameters and figure of merits that enable a comparison of a battery's electrochemical performance [7].

One of the primary figure of merit for selecting electrode materials for Li-ion batteries is the theoretical gravimetric capacity (mAh g^{-1} or Ah kg^{-1}). The theoretical

gravimetric capacity of an electrode material for Li-ion batteries is expressed by the following equation:

$$Q_{theoretical} = \frac{nF}{3.6 \times M_w} \tag{1.7}$$

where, n is the number of reactive electrons per formula unit, F the Faraday constant, and M_w the molar weight of the material. The number of electrons is determined by the number of Li^+ ions accommodated in a host lattice. Empirically, this equation implies that for a material with a smaller molecular weight and a larger amount of Li^+ ions accommodated per unit will yield a higher capacity.

The theoretical specific energy density (Wh kg^{-1})of the material can then be determined by the following:

$$E_{theoretical} = V_{oc}Q_{theoretical} \tag{1.8}$$

where V_{oc} (V), is the open circuit potential of the battery, and $Q_{theoretical}$ is determined from Equation 1.7. However in a full cell, where Li-metal is not used as an electrode, the theoretical energy of the battery depends on the capacity of the materials and average potential of each electrode material.

$$E_{full} = \left(\frac{1}{Q^c} - \frac{1}{Q^a}\right)^{-1} (E^c - E^a) \tag{1.9}$$

where Q^c and Q^a are the capacity of the active materials of the positive and negative electrodes, respectively; E^c and E^a are the potential of the cathode and anode, respectively.

Another important battery parameter is C-rate. A charge nC rate signifies that the battery achieves a full charge at a time of $^1/n$ hours (e.g. 0.1 C means it takes 10 hours to fully charge/discharge the entire battery).

The maximum power output of a battery (P_{max}) is defined as:

$$P_{max} = I_{max}V_{max} \tag{1.10}$$

where V_{max} is the maximum voltage, which ideally would be V_{oc} and I_{max} is the maximum discharge current. Realistically, the operating voltage (V_{cell}) tends to decreases and can be describe by:

$$V_{cell} = V_{oc} - I_{dis}R_s \qquad (1.11)$$

where I_{dis} is the discharge current and R_s is the cell's internal resistance (R_s tends to build up upon cell degradation). The power density of the battery is given by P_{max} divided by the total mass/volume of the cell. A Ragone chart can then be generated in the log-log scale, with the power density (X-axis) and energy density (Y-axis) of the cell at varying C-rates being a point in the plot. The Ragone chart provides an excellent mean to compare the different energy storage technologies.

Upon cycling, the battery experiences some amount of degradation, and is termed battery aging. The coulombic efficiency of a battery can be measured in % where it is defined as the ratio between the discharge and charge capacity for each cycle:

$$Q_{theoretical} = \frac{Q_{dis}}{Q_{ch}} \times 100 \qquad (1.12)$$

The rate of capacity lost upon cycling is then inverse proportional to the duration of the test (t_{ts}), which is normally denominated by the number of cycles,

$$\psi = \frac{1 - CE}{t_{ts}} \qquad (1.13)$$

The rate of capacity loss is a representation of the numerous degradation mechanisms that take place in a battery; this includes, the growth of the solid electrolyte interphase (SEI) layer, the degradation of the electrode material, impurities build up in the electrolyte (dissolved from electrodes-reaction), and unwanted side-reactions. All of which contributes to the capacity fade in a battery [7].

1.3   The Li-ion Batteries Trifecta

Ever since the inception of commercial Li-ion batteries by Sony in the early 1990s, Li-ion batteries have disrupted the existing energy storage market, replacing many of it's predecessor (especially Ni-MH and Ni-Cd), it is the go to battery chemistry for a lot of the portable applications [7, 8]. From physical principles, Li-ion batteries have certain fundamental advantages over other cell-chemistry; Li has the lowest reduction potential of any element, enabling it to have the highest possible cell potential; Li is also the third lightest element and has one of the smallest ionic radii for a single charged ion [7,9]. All these factors are enablers for Li-based batteries' high gravimetric and volumetric capacities, and power density. However to this date, even by having the highest operable voltage and energy density for a commercial secondary battery, Li-ion batteries still have not gain full market share in the energy-storage sector [9]. The primary inhibiting factors for Li-ion batteries growth are the need for better electrochemical performance (energy, power density, and cycle-ability), low cost, and improved safety [9–11]. A *trifecta* situation presents itself, in which by accomplishing all three, defines an ideal rechargeable battery (Figure 1.2).

The following subsections presents the discussion in brief and in relevance to the motivation for the research in this dissertation. However, it is important to note that each individual subsection in its entirety is worthy of a review article length discussion. The interplay between each subsection, presents the route to creating the ideal Li-ion battery.

1.3.1   Low Cost

Over the past two decades, many efforts have been dedicated to reducing the cost of Li-ion batteries in order to improve its competitiveness with the other battery technologies (Pb-Acid, Ni-MH, and Ni-Cd) [7,8]. Recently, the cost of Li-ion batteries in terms of US\$ kWh^{-1} has been leading the forefront of other battery technologies (from 2007 - 2015, prices have dropped from US\$ 1000 kWh^{-1} to < 300 US\$ kWh^{-1}
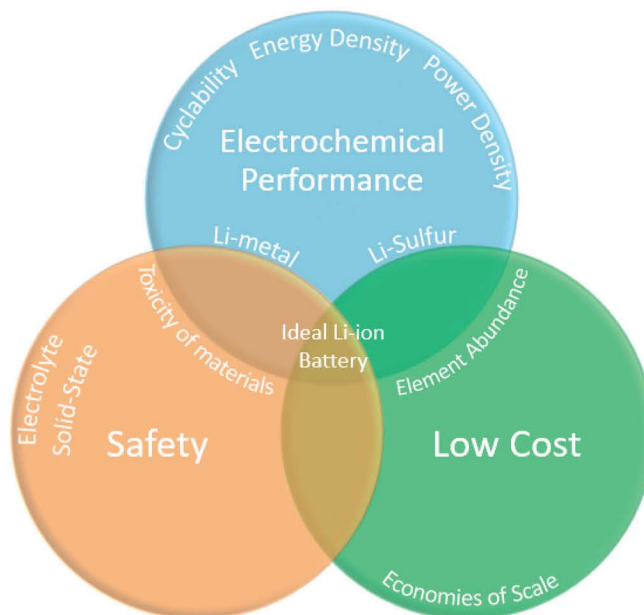
Fig. 1.2.: Illustration of the Li-ion batteries *trifecta*, in which having all three factors provides the ideal Li-ion battery.

[11–13]). Li-ion is now the only rechargeable battery other than lead acid produced at >5 GWh yr^{-1}, with a worldwide manufacturing expansion reaching hundreds of GWh yr^{-1} over the next five years [11]. However with the recent drive for large scale grid storage and electric vehicles, Li-ion batteries are compared against other energy storage technologies (e.g. internal combustion engines, fuel cells, pump hydro, etc.). The penetration of Li-ion battery into the grid storage and electric vehicle market, has set the goal for the cost of the Li-ion battery system to be reduced to $\sim\$125$ kWh^{-1} [14]. Other concerns regarding Li-ion batteries also include the shortage of Li and some transition metals currently used in Li-ion batteries, which may one day become an issue [15]. However, a significant shortage of Li has been deemed unlikely [9,16,17]; Furthermore, it has been shown that in terms of absolute quantities, the amount of Li available on the Earth's crust is sufficient to power a global fleet of electric vehicles [18]. Even so, the major cost components in a Li-ion battery is not lithium itself, but the various transition metals in the cathode material [19].

In the cell level, about 50% [13, 14, 20] of the cost comes from the fabrication of the electrodes, with the cathode being the major cost contributor. Commercially available cathodes are of the following chemistry (Table 1.1): $LiNi_xMn_yCo_{1-x-y}O_2$ (NMC), $LiNi_{0.8}Co_{0.15}Al_{0.05}O_2$ (NCA), $LiFePO_4$ (LFP), $LiCoO_2$ (LCO), $LiMn_2O_4$ (LMO), with the most expensive being LCO. Hence one of the key factors here to drive cost down is the usage of elemental abundant compound for battery components, and the search for non-cobalt based chemistry. Among the non-cobalt based cathode materials, $LiFePO_4$ is a success story; once characterized by its low-conductivity, now become the material of choice for high power applications, as the material is both cheap and has the ability to discharge at high current densities [21, 22]. As shown in Table 1.1, the different Li-based cathode materials can have different electrochemical properties, some suiting a particular application more then the other.

Table 1.1.: Electrochemical properties of various commercialized cathode materials at the present time [10], its cost [19], and its full-cell applications

Cathode Materials	Midpoint voltage vs. Li @ C/20 (V)	Specific Capacity (Ah/kg)	Cost (US$/ kg)	Applications
LCO	3.9	155	36	Mainly smaller portable electronics (3C).
LMO	4.0	100-120	10	Higher power applications such as power tools and electric motive power.
NCA	3.7	180	33	Excellent for motive power and premium electronic applications.
NMC	3.8	160	31	Portable and high power applications, including power tools and electric vehicles.
LFP	3.4	160	20	Mainly used in high power, power tools and energy storage applications.

Studies discussing other routes to reducing the cost of Li-ion batteries which are not mentioned also includes cell design (18650 vs prismatic cell), electrode processing, and materials synthesis. All of which involve the decrease usage of energy intensive processing, the removal of high cost components, and the move towards aqueous based processes [20].

Cost minimization can be performed in the cell, electrode, and materials manufacturing process; however to provide a significant cost reduction, improvement to the electrochemical performance of the cell is needed. By hindsight, this is also the

initiator of the Li-ion battery revolution that replaced its Ni-MH and Ni-Cd predecessors, where the Li-ion battery chemistry provided a significant improvement in the electrochemical properties. The various ways to improve electrochemical performance of a battery is covered in the following segment.

1.3.2 Electrochemical Performance

Electrochemical performance of a battery is indicated by the battery's energy, power density, and the cyclability of the battery. Currently, DOE has set the target at 235 Wh kg^{-1} and 500 Wh L^{-1} for energy densities by 2020 for electric vehicle applications [1,14]. This goal has been the primary direction for many of the present-day battery's research [23,24]. In the current Li-ion battery, a major limiting factor for high energy density is the specific capacity of the cathode materials. The search for an alternative cathode chemistry with high capacity and high operating voltage is of significant importance. On the other hand, a large number of anodic materials with high specific capacity and high abundance have been studied (Table 1.2) [8,9,24]. To date, many of the anodic materials in commercialized Li-ion batteries are graphitic materials. There have also been reports on the addition of small amounts of Si in the mixture to increase the total energy density of the batteries [10,24]. However it is a well known fact that Si upon lithium insertion experiences a volumetric expansion of up to $\sim 400\%$ and consequently suffers high capacity fade [8,9,23].

Table 1.2.: Properties [9] and cost [11, 19] of different anode materials. Specific capacities are listed as practical capacity, with their associated volume change. (* theoretical specific capacity)

Anode Material	Lithiation/Delithiation potential (V vs. Li/Li$^+$)	Specific Capacity (Ah/kg)	Cost (US$/ kg)	Volume Change
Graphite	0.07, 0.1, 0.19/ 0.1, 0.14, 0.23	330-360	19	10%
Si	0.05, 0.21/ 0.31, 0.47	4200	2.29	400%
Sn	0.4, 0.57, 0.69 / 0.58, 0.7, 0.78	990	10	255%
Li	0	3860*	80	N/A

General strategies to overcome the limitations of a material and its rationale for improved capacity (energy density), kinetics (power density), and stability (cyclability) have been developed (shown in Table 1.3 [9, 24]). This includes: 1) Reduction of particle size; 2) Composite formation; 3) Doping and functionalization; 4) Morphology control; 5) Coating and encapsulation; and 6) Electrolyte tuning.

Table 1.3.: General materials engineering strategies and their respective rationale to overcome the limitations of battery materials.

Strategy Routes	Rationale
Dimension Reduction	Faster ion & electron transport. Increase surface reactivity. Improved mechanical stability.
Composite Formation	Improve conductivity (conductive host/additive). Improve mechanical support.
Doping and Functionalization	Faster ion and electron transport. Improve chemical and thermal stability.
Morphology Control	Improve structural stability. Faster ion and electron transport. Modified surface reactivity.
Coating and Encapsulation	Protection from electrolyte. Electrolyte decomposition prevention. Stabilization of surface reaction. Improve conductivity (conductive coating).
Electrolyte Tuning	Formation of passivation layer on surface electrode.

With no immediate solution to the cathode chemistry, recently, it has been heavily suggested to revive the usage of Li-metal as anodes for Li-ion batteries [11, 23–26]. With the replacement of graphitic materials with Li-metal at the anode, it has been shown that at the individual cell level, this will be a ∼35% increase in gravimetric energy density and ∼50% increase in volumetric energy density (from ∼ 150 Wh kg^{-1} to ∼250 Wh kg^{-1} and from ∼250 Wh L^{-1} to ∼750 Wh L^{-1}) [11]. A major factor hindering the usage of Li-metal as an electrode is its ability to form dendrites upon cycling, as the propagation of the dendrites from anode to cathode can cause short circuiting, and inherently cause thermal runaway. This has lead to many studies focusing on strategies to mitigate Li-dendrites formation/propagation [23]. In gen-

eral, these studies aim at stabilizing the Li-metal|electrolyte interface, by creating an artificial layer or tuning the electrolyte to allow the formation of a stable layer at the interface. These layers typically homogenize the Li-ion flux by modifying the electric field at the interface, allowing for better control of Li-ion deposition at the interface, thus preventing the growth of Li-dendrites. The layer can also act as a mechanical barrier that prevents the propagation of Li-dendrites. Building from this, the next segment discusses on designs to improve the safety of Li-ion batteries, which focus on the need for breakthrough in solid-state electrolyte technologies. Solid state electrolytes act as both an electrolyte and a physical barrier to prevent Li-dendrites growth and propagation.

1.3.3   Improved Safety

There are variety of safeguard measures in a conventional Li-ion battery. This includes the robust casing of a battery, smart separators that stop permeation of electrolyte upon temperature rise, battery management systems to prevent overcharging/discharging etc. Herein, discussions are focused on improving the safety of the battery by replacing existing organic liquid electrolytes with solid-state electrolytes (SSE), and the limitations of solid-state electrolyte implementation, as well as further safety issues in a solid-state electrolyte system. Organic liquid electrolytes, offer the benefits such as high ionic-conductivity and excellent wettability on electrodes, but often suffer from low ion selectivity, inadequate electrochemical and thermal stabilities, and poor safety [27]. Replacement of liquid electrolytes with solid-electrolyte separator not only overcome some of the limitations of liquid electrolytes, but offer possibilities for developing new battery chemistry (this includes some of the high-capacity electrodes, e.g. sulfur cathodes and Li metal anodes).

Important properties that should be taken into consideration when designing solid-state electrolyte include, high ionic conductivity, negligible electronic conductivity, wide electrochemical stability window (operating voltage window), good chemical

compatibility with electrodes; excellent mechanical properties, relative ease of fabrication at large scale, low cost, and easy device integration. The various key solid-state electrolyte chemistries are shown in Table 1.4, with comments on some of their notable properties.

Table 1.4.: List of solid-state electrolytes, their class-type, room temperature conductivity (unless specified), their typical advantages and disadvantages. [23, 27, 28]

Type	Materials	Conductivity (S cm^{-1})	Advantages	Disadvantage
Oxide	Perovskite-Li$_{3.3}$La$_{0.56}$TiO$_3$ NASICON- LiTi$_2$(PO$_4$)$_3$ LISICON-Li$_{14}$Zn(GeO$_4$)$_4$ Garnet-Li$_7$La$_3$Zr$_2$O$_{12}$	10^{-5}–10^{-3}	-High chemical and electrochemical stability. -High mechanical strength. -High electrochemical oxidation voltage.	-Not flexible -Expensive to scale
Sulfide	Li$_2$S-P$_2$S$_5$ Li$_2$S-P$_2$S$_5$-MS$_x$	10^{-7}–10^{-3}	-High conductivity. -Good mechanical strength and mechanical flexibility. -Low grain-boundary resistance.	-Low oxidation stability. -Sensitive to moisture. -Poor compatibility with cathode materials.
Hydride	LiBH$_4$, LiBH$_4$-LiX (X=Cl,Br or I)	10^{-7}–10^{-4}	-Stable with Li-metal. -Good mechanical strength. and mechanical flexibility.	-Sensitive to moisture. -Poor compatibility -with cathode materials.
Thin-film	LiPON	10^{-6}	-Stable with Li-metal. -Atomically smooth surface. -Stable with cathode materials.	-Expensive to scale.
Polymer	PEO	10^{-4} (65–78°C)	-Stable with Li-metal. -Flexible. -Easy to scale up (large-area membrane). -Low shear modulus.	-Limited thermal stability. -Low oxidation voltage (<4V).

Various systems of solid-state electrolyte have been proposed, including hybrids, where a mixture of liquid and solid-state electrolytes are used. The ultimate goal is an all-solid-state Li-ion battery, which offers higher energy densities, as it has fewer requirements in terms of packaging and have a simpler structure as compared to conventional Li-ion batteries with liquid electrolytes. To achieve this, there are several key challenges that needs to be addressed, volumetric changes in electrode and electrolyte, large interfacial resistance, low mass ratio of electrode-active materials, and poor cycling stability.

One pressing issue that needs to be address is finding ways to improve interfacial ionic conductivity, as well as interface stability at anode|electrolyte and cathode|electrolyte interfaces. Another important factor affecting the interface is the mechanical properties of the solid electrolyte, in general a good solid-state electrolyte should have a low Young's modulus. During cycling of the battery, the electrodes (typically the oxide

cathodes) tend to experience structural fragmentation, resulting in capacity fade. A solid-state electrolyte that is malleable and ductile would have the ability to reduce the fragmentation of the active materials and improve interfacial contact between electrolyte and electrode (interface contact plays a significant role in interface ionic conductivity). However not all solid-state electrolytes have a low Young's modulus (especially oxide based). An alternative failure mode (which was not thought possible) has recently been observed, where Li-dendrite propagates through pre-existing interfacial defects, namely Griffith flaws [29]. It has been suggested that to suppress Li-dendrite penetration, solid state electrolyte needs to have low defect density [28]. Designs of an hierarchical interface for an all-solid-state battery are required, where the electrolyte at the Li|SSE interface is fully dense, preventing Li-dendrites penetration; and porous at the SSE|cathode interface, to allow for more utilization of cathode active loading mass [30]. Incorporate to this design can also include ALD coating to control the surface morphology of the solid-state electrolyte to allow for better interface contact at the Li|SSE interface [31].

In all, one must tailored and design the solid-state cell from ground up. Where the materials selection for electrodes has to be electro-chemo-mechanically compatible with the solid-state-electrolyte.

1.3.4 Summary

In summary, there is no general solution to all the existing problems in a Li-ion battery; However, the Li-ion battery field has had progress far from its first inception and has made many incremental breakthroughs over the past two decades. With that in mind, this dissertation, though focuses on three very different components of a battery, the overall theme is maintained by attempting to achieve a little in each segment of the *trifecta*: low cost, improved electrochemical performance, and safety.

2. LITHIUM STORAGE IN STRUCTURALLY TUNABLE CARBON ANODE DERIVED FROM SUSTAINABLE SOURCE

Authors: Daw Gen Lim[†], Kyungho Kim[†], Mayuri Razdan[†], Rosa Diaz[§], Sebastian Osswald[†], and Vilas G. Pol[†,‡]

[†]School of Materials Engineering, Purdue University, West Lafayette, 47907, USA.
[§] Birck Nanotechnology Center, Purdue University, West Lafayette, 47907, USA.
[‡] School of Chemical Engineering, Purdue University, West Lafayette, 47907, USA.

In the following work, Daw Gen Lim contributed to the material synthesis, *in situ* and *ex situ* Raman microscpetroscopy, powder X-ray diffraction, and electrochemical studies. Kyungho Kim assisted with the scanning electron microscopy images. Dr. Mayuri Razdan proof read the manuscript; Dr. Rosa Diaz assisted in the TEM and HRTEM imaging. Dr. Sebastian Osswald and Dr. Vilas G. Pol are the PIs.

Abstract

A meticulous solid-state chemistry approach has been developed for the synthesis of carbon anode from a sustainable source. The reaction mechanism of carbon formation during pyrolysis of sustainable feed-stock was studied in situ by employing Raman microspectroscopy. No Raman spectral changes observed below 160 °C (thermally stable precursor) followed by color change, however above 280 °C characteristic D and G bands of graphitic carbon are recorded. Derived carbon particles exhibited high specific surface area with low structural ordering (active carbons) to low specific surface area with high graphitic ordering as a function of increasing reaction temperature. Carbons synthesized at 600 °C demonstrated enhanced reversible lithiation capacity (390 mAh g^{-1}), high charge-discharge rate capability, and stable cycle life. On the contrary, carbons synthesized at higher temperatures (>1200 °C) produced more graphite-like structure yielding longer specific capacity retention with lower reversible capacity.

2.1 Introduction

The increased demand for efficient energy storage devices has intensified the development of advanced high-performance rechargeable batteries during the last two decades. Currently considered the state-of-the-art battery technology, lithium ion batteries (LIBs) are the energy storage solution of choice for portable consumer electronics, and are poised to enter new markets such as electric vehicles and grid storage [32, 33]. With the rising demand for LIBs, the search for inexpensive, more sustainable high-capacity electrode materials has become ever more imperative. Carbonaceous materials are still the primary anode material, with graphitic carbons accounting for the majority of all anodes utilized in commercial LIBs [34, 35].

The specific capacity of a perfectly graphitic structure cannot exceed 372 mAh g^{-1}, thus limiting the energy density of graphite-based anodes. In contrast, owing to a different storage mechanism, a variety of disordered carbons were found to exhibit

significantly higher capacities, reaching 1000 mAh g^{-1} or more [36–39]. From a cost and sustainability perspective, disordered carbons derived from biomass are of particular interest.

To date, a wide variety of biomass sources have been investigated (Table 2.1), including sugar, oak, walnut, almond, lignin [37] starch [37, 40, 41], mangrove [42], peanut [43], coffee shells [44], sisal [45], banana fibers [46], rice husk [47,48], straw [49], alginic acid [50], olive [51], and cherry stones [51, 52]. More recently, bamboo chopsticks [53], and wheat straw [54] have been used. Unfortunately, many of these precursors have their individual short comings, including the need for acid/base treatments before pyrolysis [43, 44, 46–49, 51–53]; salt baths for impregnation of catalytic metal particles [46, 51]; or high temperature treatment (>1000 °C) [42]. In addition, the resulting carbons often exhibit high capacity fade [44, 45, 49, 52] and/or suffer from poor cyclability [48]. The above studies have revealed that among all the biomass-derived carbons, starch offers the highest control over structure and properties of the resulting carbon [40, 41, 55]. In recent electrochemical studies, spherical porous carbon particles were obtained from potato starch, achieving specific capacities of 475 mAh g^{-1} after 20 cycles at 1C [40] and 513 mAh g^{-1} after 50 cycles (C-rates were not reported) [41].

In spite of the great progress in the morphological control from starch-derived carbons, to the best of our knowledge, wheat flour derived from cereal grains of the *Triticum* genus comprising mostly carbohydrates (starch), protein, minerals and minor vitamins has not been explored as potential carbon precursor for anode materials in lithium ion batteries. This comes as a surprise given the fact that in 2013, the world wheat production was around 713 million tons, which is about 25% of the global cereal grain production, ranking third compared to maize and rice [56]. Moreover, the granule size of wheat starch ranges from 1–45 μm, which is smaller and thus more favorable than that of potato starch [57]. At the same time, amylopectin-amylose-ratio, the two main components in starch, for wheat (72:28) is similar to that of potato starch (79:21) [57]. These two main components will be the primary source

Table 2.1.: Literature survey of the various biomass derived carbons, their synthesis methods and their respective half-cells reversible capacities with respect to lithium at similar C-rates (0.1C), otherwise noted.

Precursor	Synthesis	C_{rev} (mAh g^{-1})
Potato Starch Granules [40]	Baking (200 - 300 °C) + Pyrolysis (1000 °C)	540
Mangrove Charcoal [42]	Pyrolysis (1000 °C)	463
Sisal Fibers [45]	Pyrolysis (900 °C) + Hydrothermal activated (140 °C)	250
Rice Husk [48]	Autoclave (230 °C) + Pyrolysis (900 °C) + SiO2 etching NH$_4$HF$_2$	403 @0.2C
Alginic Acid [50]	HCl bath + Pyrolysis (1500 °C)	255 @0.7C
Olive Stones [51]	H$_2$SO$_4$ bath + ZnCl$_2$ impregnation + Pyrolysis (500 °C)	267 @0.2C
Cherry Stones [52]	KOH bath + Pyrolysis (500 °C)	348
Bamboo Chopsticks [53]	KOH bath + Various heating and washing process (150 °C + 60 °C) + Pyrolysis (800 °C) + HCl bath	355 @0.37C
Wheat Straw [54]	HCl bath + KOH bath + Pyrolysis (700 °C)	1470

for the structurally tunable carbon content in the wheat flour, making it a promising candidate as precursor material for lithium-ion battery anode applications. Hence, in this paper, we report on the utilization of a sustainable, inexpensive wheat flour-derived carbons as a promising anode material in lithium ion batteries. Our primary focus is the critical structure-property-relation, with emphasis on the electrochemical performance of the resulting carbons.

2.2   Experimental

2.2.1   Material Preparation

Raw wheat flour (Aashirvaad, ITC Limited) were used as feedstock precursor for carbon synthesis. Approximately 3 g of wheat flour were inserted into an alumina boat

for carbonization in a tube furnace under inert argon atmosphere, with a constant flow rate of $\sim$10 ml min^{-1}. The ramping rate was set at 5 °C min^{-1} and the holding time was 2 hrs. Carbonization temperatures were set to 300, 400, 500, 600, and 700 °C. For selected samples, a secondary high-temperature treatment (graphitization) was conducted. Two samples, carbonized at 600 °C, were further annealed for 2 hrs at 1200 and 1600 °C, respectively. The step towards structural ordering of pre-synthesized carbons was conducted in an argon atmosphere (flow rate of 100 ml min^{-1}) using a high temperature alumina tube furnace and a ramping rate of 3 °C min^{-1}.

2.2.2 Material Characterization

Thermogravimetric analysis (TGA) was performed using a TGA Q50 from TA instruments. Carbonization of wheat flour was measured under a constant Ar purge, whereas thermal stability studies of the as-produced carbons were conducted in air ($\sim$40 ml min^{-1}). All heating and cooling rates were set to 5 °C min^{-1}.

In situ Raman spectroscopy studies were carried out to study the formation mechanism of carbon from the wheat-flour employing a DXR Raman microscope (Thermo Scientific) with an Ar-ion laser (532 nm), and a 50× microscope objective with a 25-μm slit. All in situ experiments were carried out in a programmable temperature stage (Linkam THMS600) under inert Ar atmosphere with O$_2$ levels <1 ppm, and a constant argon purge of 10 ml min^{-1}. Samples were dispersed on a quartz slide and placed in the temperature stage. Each Raman spectrum was collected for $\sim$45 sec using a laser power density of 3.5 mW cm^{-2}. *Ex situ* Raman spectra of the as produced carbon samples were collected as well with the as described parameters.

Particle morphology was characterized using a scanning electron microscope (SEM, FEI XL40 at 5 kV), and transmission electron microscope (TEM, FEI Titan ETEM 80–300 at 300 kV). Surface area and pore size were analyzed using a Micromeritics Tristar 3000, the samples were outgas at 300 °C for 12 hrs.

Powder X-ray diffraction (XRD) was performed using a Rigaku (Cu source), at an acceleration voltage of 40 kV and a current of 44 mA. Data were collected in the range $2\theta = 10$–$80°$ using a step size of $5°$ min^{-1}. The Scherrer equation (2.1) was used to determine the dimension of the crystallite thickness (L_c), and L_a the cluster diameter or the in-plane coherent length.

$$L = \frac{\kappa\lambda}{\beta cos\theta} \tag{2.1}$$

Where κ is the geometrical factor, λ is the X-ray source wavelength, θ is the scattering angle in radians, and β is the full width at half maximum (FWHM) for the peaks used in radians. The (002) peak center is used to calculate L_c, and κ equals 0.9. For the dimensions of the cluster diameter (L_a), the peak center of (100) data is used and κ equals 1.84 [58]. Transmission electron microscopy (TEM, FEI Titan ETEM 80-300 at 300 kV) is used for the structuring understanding.

2.2.3 Electrochemical Studies

Electrode slurries were prepared by mixing 80 wt.% wheat-derived carbon with 10 wt.% polyvinylidene fluoride (MTI) binder and 10 wt.% of conductive carbon (Timcal SuperP). The powder mixture was then dispersed in N-methyl-2-pyrolidone (MTI) and casted on a copper foil using an automated doctor blade applicator. The electrode was subsequently dried in a vacuum oven (80 °C for ~8 hrs). Coin cells were assembled in half-cell configuration using a lithium metal electrode (MTI) and a standard electrolyte (MTI) containing 1M $LiPF_6$ in EC:DMC:DEC (1:1:1) with Celgard 2500 separator. Cell assembly was conducted in an Ar-filled glove box (H_2O and O_2 less than 1 ppm). Galvanostatic charge-discharge cycles were conducted on a Maccor 4000 series with the cycling voltage range of 0 to 3.0 V at various C-rates, C-rates were normalized to the electrode mass, assuming theoretical capacity of graphite, 372 mAh g^{-1}. Electrochemical impedance spectroscopy (EIS) were conducted on cells

at a charged state with an oscillation of 5 mV amplitude over the frequency of 100 kHz to 0.01 Hz.

2.3 Results and Discussion

Wheat flour derived carbons were synthesized using an isothermal pyrolysis process (Figure 2.1 shows a schematic of the fabrication process from precursor to as-derived carbon to battery fabrication). The as-derived carbons were subsequently mechanically milled and used as anode material for half-cell studies. To gain further insight to the carbonization process, both *in-situ* Raman (Fig. 2.2a) and TGA analysis (Fig. 2.2c) were conducted on the wheat flour.
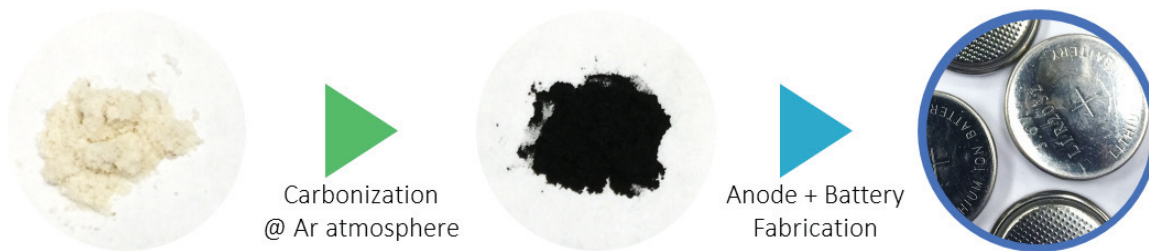
Fig. 2.1.: Schematic of lithium half-cell fabrication from wheat flour derived carbon treated at 600 °C

Figure 2.2a depicts *in-situ* Raman spectra recorded for a wheat flour during carbonization in an inert atmosphere. No spectral changes were observed at temperatures below 160 °C, confirming thermal stability of the precursor. Around 180 °C, the powder starts to decompose, as indicated by notable changes in the Raman intensity. Between 200 and 280 °C, large intensity fluctuations, likely caused by the reaction products and condensation of the evolving gases on the stage windows, inhibited reliable Raman measurements. When reaching 280 °C, the decomposition was largely completed and the characteristic D and G bands of graphitic carbon appeared at $\sim$1315 and $\sim$1585 cm^{-1}, respectively.

It was noted that the discoloration of the sample during heating was not homogenous. Changes in color were first observed in the sample area illuminated by the laser (see inset in Fig. 2.2a), suggesting that laser irradiation is affecting the carbonization process. Optical images of wheat flour taken during carbonization in the temperature stage, but without laser excitation, confirmed this assumption. No color changes were identified below 220 °C, revealing that laser-induced heating during the *in-situ* Raman characterization has lowered the carbonization temperature by 30–40 °C.

To complement *in-situ* Raman measurements, thermogravimetric analysis (TGA) was conducted to determine the corresponding sample burn-off during carbonization (Fig. 2.2c). The initial weight loss (∼10 wt. %), occurring between 60 and 100 °C, is caused primarily by moisture removal. According to TGA data, the decomposition of the wheat powder starts around 240 °C, which is in good agreement with optical studies conducted in the Raman stage. Although the primary decomposition occurs below ∼360 °C, the sample continues to lose weight until 600 °C, where the carbonization process concludes. The obtained Raman and TGA data are therefore consistent with previous studies on similar biomaterials [59–62].

Bulk samples of wheat flour were also carbonized in a tube furnace at different temperatures in the range 300–700 °C. Two samples, both carbonized at 600 °C, underwent an additional thermal annealing treatment (graphitization) at 1200 and 1600 °C, respectively.

Figure 2.3 shows SEM micrographs of the wheat flour precursor and the as-produced carbon samples. Due to charging, the as-received wheat flour (Fig. 2.3a) and the carbon synthesized at 300 °C (Fig. 2.3b) required a thin, conductive Pt coating for imaging. It can be noted that the overall porosity of the material increases when increasing the annealing temperature from 300 to 600 °C (Fig. 2.3b–2.3e). While larger pores (>40 μm) originating from the polymer precursor (Fig. 2.3a) are partially preserved, small pores form upon decomposition of the organic material. According to SEM analysis, further increase in annealing temperature from 600 to
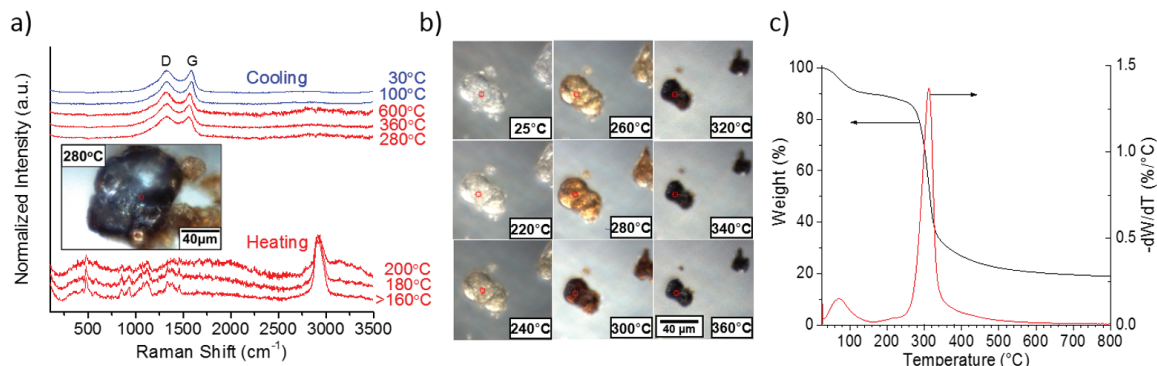
Fig. 2.2.: a) *In-situ* Raman spectra of wheat powder undergoing heating and cooling treatments in an inert atmosphere; the inset shows an optical micrograph of the sample, when D and G bands are first observed upon heating, b) *in-situ* optical micrographs of the wheat powder granules undergoing the same heating process in Raman stage, but without laser illumination, and c) thermogravimetric analysis with weight loss (left Y axis) and DTG (right Y axis) curves of as-received wheat powder.

700 °C (Fig. 2.3f), or additional graphitization steps at 1200 (Fig. 2.3g) and 1600 °C (Fig. 2.3h) did not yield significant changes in the microstructure.
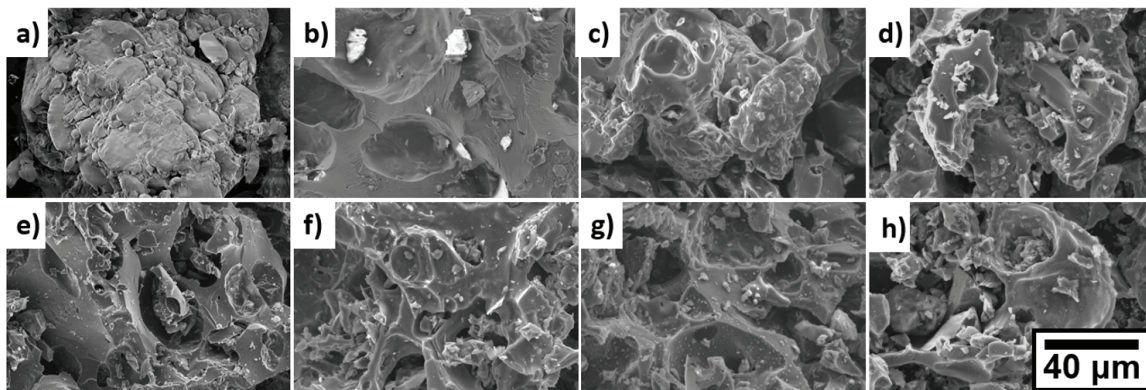
Fig. 2.3.: Scanning electron micrographs of a) as-received wheat flour and the as-processed carbons at b) 300, c) 400, d) 500, e) 600, f) 700, g) 1200, and h) 1600 °C.

To obtain further insight into the structural differences of the heat-treated wheat flour samples, we characterized all samples using Raman spectroscopy (Fig. 2.4a and 2.4b), X-ray diffraction (Fig. 2.4c), and TEM (Fig. 2.5). The Raman spectra

of all heat-treated wheat flour samples exhibit the characteristic D and G Raman bands of graphitic (sp^2) carbon. For the carbonized samples (300–700 °C), peak shape and intensity distribution are similar; with a D-to-G Raman band intensity ratio (D/G) in the range 0.8–1.0, represent the Raman features of a disordered sp^2-carbon. Additional heat treatment at higher temperatures (1200 and 1600 °C) leads to an increase in D/G ratio and higher G band frequencies. According to Ferrari et.al, during the transition from disordered carbons to nano-crystalline graphite, the intensity of the D band, which correlates to the breathing mode of the hexagonal ring structure, will increase relative to the G band; whereas the G band position, which correlates to the in plane bond stretching of the sp^2 bonds will upshift towards 1600 cm^{-1} (nano-crystalline graphite), before decreasing again to 1580 cm^{-1} (graphite) [63]. The observed spectral changes are therefore believed to occur due to the conversion of the sp^3 sites into sp^2 phase, as well as the increase in number and size of sp^2 clusters [64, 65].

Similar results were obtained by X-ray diffraction. The diffraction pattern recorded from the 300, 400, 500, 600 and 700 °C samples are comparable to that of highly-disordered carbons. The (002) and the (100) diffraction peaks, representing the interplanar and in-plane ordering of graphitic carbons, respectively, are of low intensity and are significantly broadened. The increase in carbonization temperature from 300 to 700 °C leads to higher in-plane ordering, but seem to have no significant effect on the interplanar ordering in the sample (Fig. 2.4d). At higher annealing temperatures (1200 and 1600 °C), both (002) and (100) peaks become more pronounced, indicating the stacking of the graphene layers (graphitization).

Peak center and full-width-at-half-maximum (FWHM) for the (002) and (100) peaks were used to calculate interplanar spacing (d_{002}), average crystallite thickness (L_c), and in-plane cluster diameter (L_a). Due to the high degree of disorder in low-temperature samples, average crystallite thickness (1200 and 1600 °C) and cluster diameter (600, 700, 1200 and 1600 °C) could only be determined for samples treated at higher temperatures. Fig. 2.4c shows that after initial formation of sp^2-carbons,
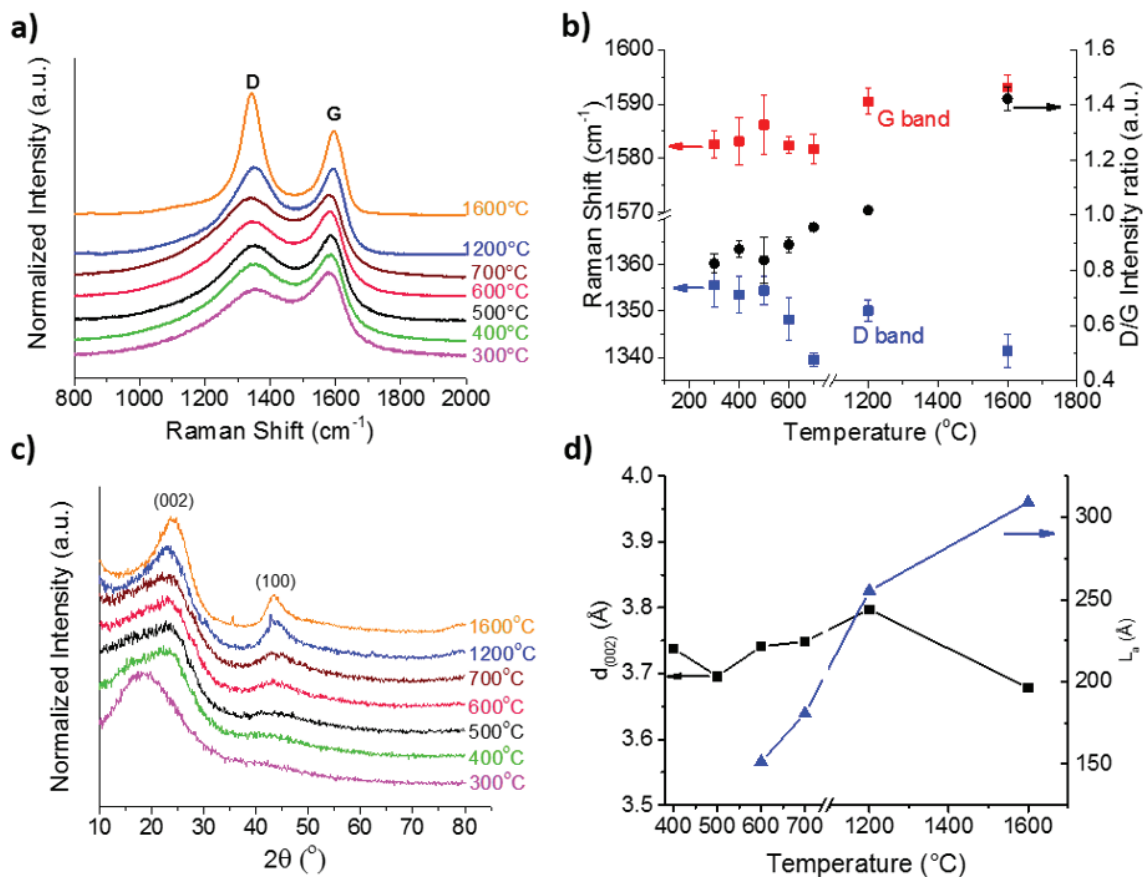
Fig. 2.4.: a) Raman spectra of the various carbon particles; b) The D and G bands center position, and the D-to-G band intensity ratio determined from the Raman spectra as a function of temperature; c) X-ray diffraction spectra of the carbon samples; d) The d_{002} spacing and the dimensions of the cluster diameter (L_a), calculated from the XRD spectra, as a function of temperature.

the (002) peak position, and thus the corresponding interplanar spacing (d_{002} in Fig. 2.4d), remain unchanged over a wide temperature range (400–700 °C). Only at higher annealing temperatures (1600 °C), thermal energy is sufficient to allow for rearranging of carbon atoms and graphitization, as indicated by the decreasing d_{002}. This is supported by the fact that L_c is only measurable at higher temperatures and increases from ~1.01 to 1.24 nm. The in-plane cluster diameter (L_a), which is determine by the (100) peak exhibits a direct correlation as a function of temperature. The cluster diameter for the low temperature derived carbon (500–700 °C) transition

from amorphous carbon (<2 nm) to nano-crystalline graphite at 1200 and 1600 °C , which is in agreement with Raman data [66].
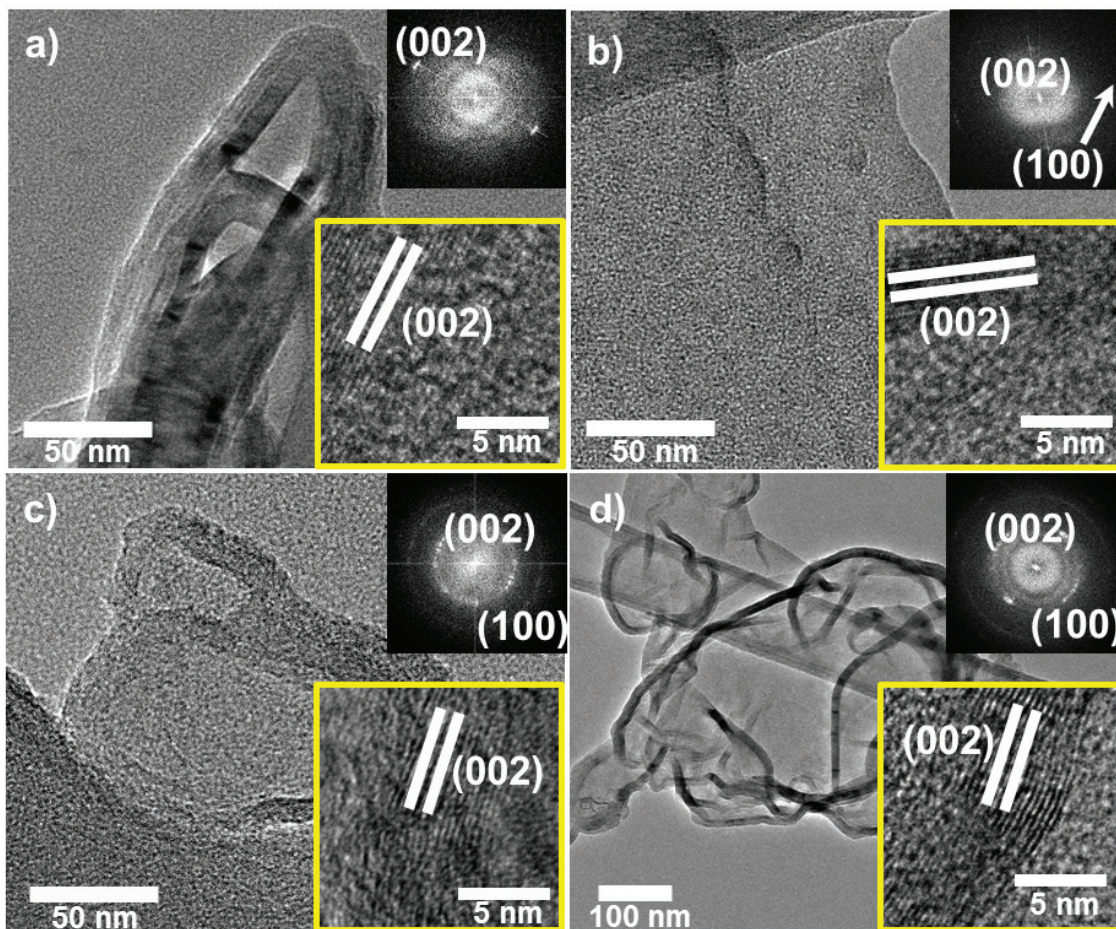
Fig. 2.5.: TEM images of the as processed carbons at a) 600 b) 700 c) 1200 d) 1600 °C. The inset (bottom right) shows the HRTEM images of the ordered regions and the amorphous regions of the carbon particles accompanied by their respective FFT image (top right). The structures illustrated in both Figure 5 a) and b) can be observed in both 600 and 700 °C derived carbons.

Ex-situ TEM studies of the carbon particles confirms that at lower carbonization temperature (Fig. 2.5a and b) the particles have lower interplanar ordering, with graphitic clusters forming on the surface of the particles. At high carbonization temperatures (Fig. 2.5c and d), an onion type structure is seen, where the carbon particles have very high graphitic layers at the surface with an amorphous core. The

interplanar spacing of the lattice can be observed in all HRTEM images, which we calculate from the FFT image to be ∼3.50 Å, which is comparable to the calculated XRD data (Fig. 2.4d).

While XRD, Raman, and TEM is useful in distinguishing the structural differences of the carbon particles, TGA in air can elucidate the oxidation resistivity of these carbon structures, indirectly representing the reactivity of these carbons. Figure 2.6 shows TGA weight loss (a) and the corresponding first order differential curves (b) of the various carbons during oxidation in air. The thermograms of the 600 and 700 °C samples are similar. Both carbons begin to oxidize around 400 °C, with the maximum weight loss and complete burn-off occurring around 510 °C and 640 °C, respectively. This suggests that during synthesis, the carbonization process is completed for all samples exposed to treatment temperatures above 600 °C, and additional heating to 700 °C has little to no effect on the resulting carbon structure.
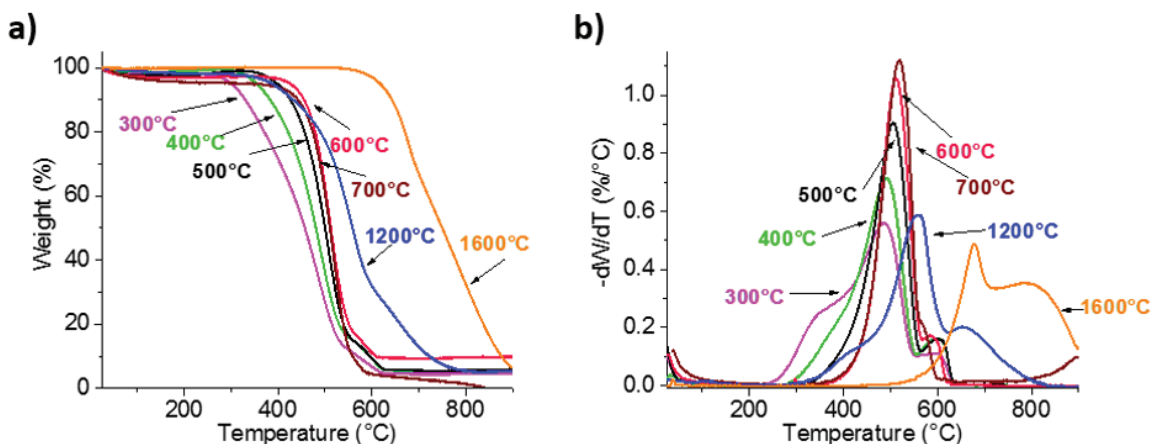
Fig. 2.6.: a) TGA measurement and b) first order differential curves of the oxidation of 300, 400, 500, 600, 700, 1200, and 1600 °C wheat flour derived carbon particles. All experiments were conducted under constant Air flow (40 mL min^{-1}) at a heating rate of 5 °C min^{-1}.

For samples produced at 300, 400, and 500 °C, the carbonization process is incomplete, resulting in additional weight losses during air oxidation well below 400 °C. The lower the synthesis temperature, the lower the onset of oxidation and the

higher the weight loss in the low-temperature region (<400 °C). Annealing at 1200 °C shifts the temperature of maximum weight loss to 560 °C, while a significant part of the sample (~30 wt. %) does not oxidize below 600 °C. High-temperature annealing at 1600 °C results in a significant up-shift in oxidation temperature. In this case, burn-off does not begin until 500 °C, with the maximum weight loss occurring at 670 °C. Weight loss observed at a higher temperature range (700–800 °C) derived carbons can be ascribed to the leaving of the complex compounds (Fig. 2.7a and b) that form from the pre-existing mineral contents in the forms of ions in the carbons after pyrolysis [67–69].
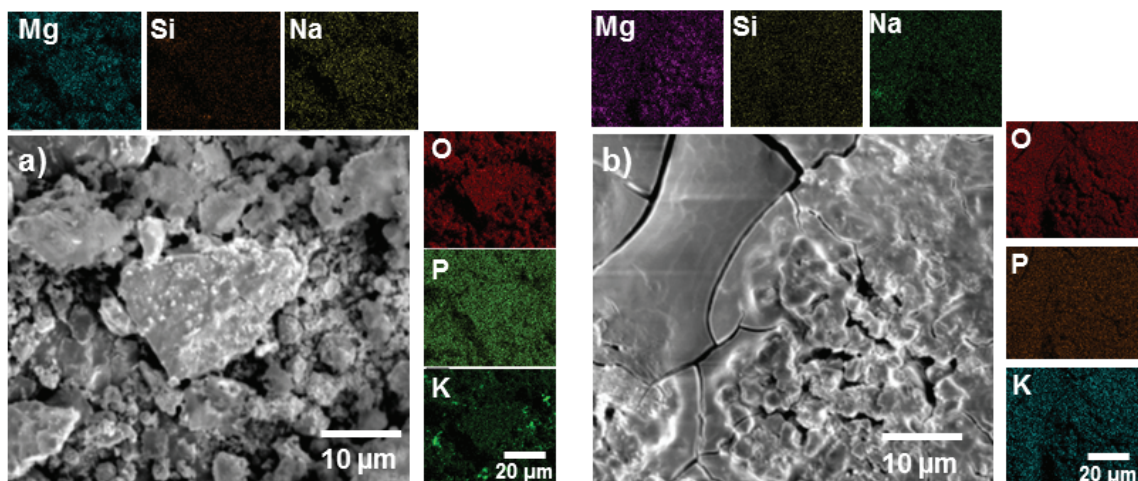
Fig. 2.7.: a) SEM images of remnant ash content for a) 600 and b) 700 °C derived carbons after TGA analysis in air oxidation environment accompanied by the respective mineral elements (inset).

Nitrogen adsorption and desorption isotherms for the 700 (Fig. 2.8a), 1200 (Fig. 2.8b) and 1600 °C (Fig. 2.8c) carbons illustrate the resulting surface area for the respective carbons to be 262.5 ± 8.4 m^2 g^{-1}, 116.8 ± 2.9 m^2 g^{-1}, and 22.7 ± 0.4 m^2 g^{-1}. From the pore size distribution plot (Fig. 2.9), at 1600 °C (Fig. 2.9c), there is a significant drop in the contribution of pores sizes <10 nm to the total pore volume, as compared to the other two samples. Whereas the 1200 °C samples (Fig. 2.9b) showed similar pore size distribution with the 700 °C derived carbons (Fig. 2.9a). The 700

°C sample also showed the lowest pore volume to surface area ratio, as compared to the other two samples, suggesting a higher number of nano- and micro-pores.
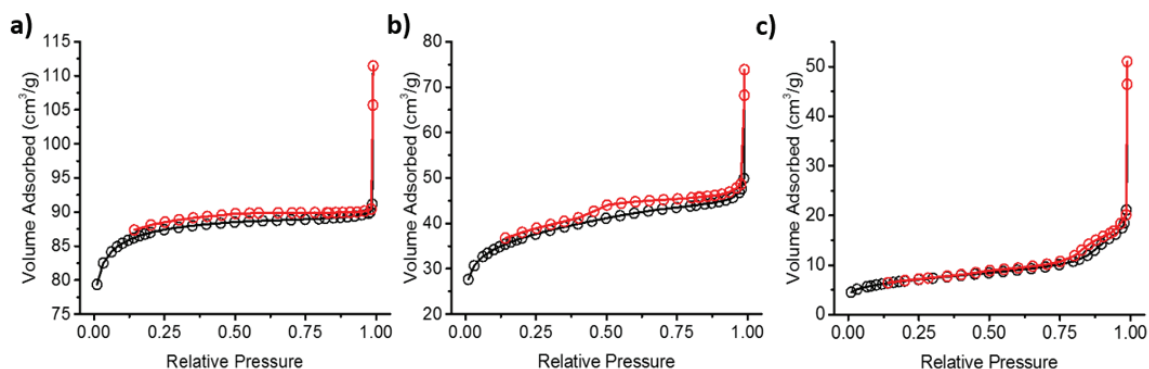
Fig. 2.8.: a) N_2 adsorption (black) and desorption (red) isotherms at 77 K for a) 700 b) 1200, and c) 1600 °C wheat flour derived carbon particles. From multi-point BET measurement, their respective specific surface areas are as follows, 262.5 ± 8.4 m^2 g^{-1}, 116.8 ± 2.9 m^2 g^{-1}, and 22.7 ± 0.4 m^2 g^{-1}.

Due to the high level of non-hydrocarbon impurities in carbons derived at <700 °C, N_2 adsorption/desorption measurements were unsuccessful, despite extensive outgassing. However, given similar XRD and Raman signatures, one can assume surface area for the 600 °C and 700 °C derived carbons to be relatively similar.
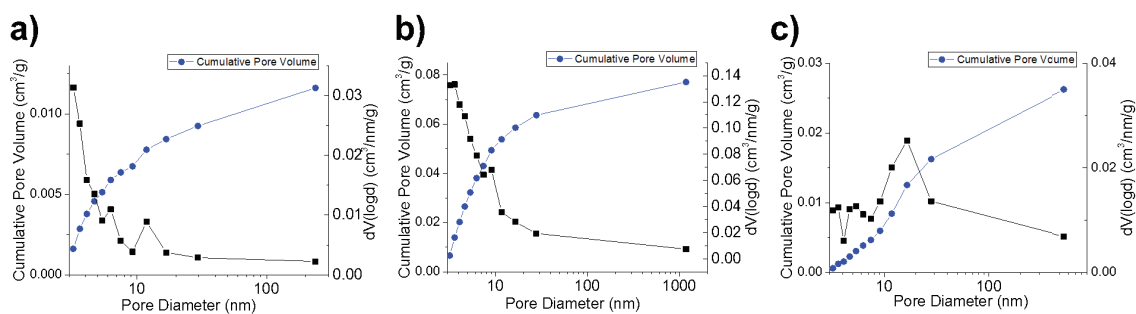
Fig. 2.9.: Pore size distribution plots for a) 700, b) 1200, and c) 1600 °C derived carbons.

The as-produced carbon samples were subjected to electrochemical testing in a half-cell configuration (vs. lithium metal), undergoing charge and discharge cycling in the range of 0–3 V at various C-rates. Carbons synthesized below 500 °C exhibited poor electrochemical performance, due to high content of non-carbon impurities, and are therefore excluded from the presented data. Figure 2.10 compares the first and second lithiation/delithiation cycle (at C/10) of the 500, 600, 700, 1200 and 1600 °C samples. The first lithiation capacity is highest for the 500 °C sample (828 mAh g^{-1}) and continues to exhibit a downward trend with increasing synthesis temperature, 600 °C (728 mAh g^{-1}), 700 °C (795 mAh g-$^{-1}$), 1200 °C (428 mAh g^{-1}), and 1600 °C (316 mAh g^{-1}). The corresponding delithiation capacities are 301 mAh g^{-1} (500 °C), 405 mAh g^{-1} (600 °C), 404 mAh g^{-1} (700 °C), 279 mAh g^{-1} (1200 °C), and 187 mAh g^{-1} (1600 °C), suggesting that carbons produced at lower synthesis temperatures are still chemically reacting due to the contained non-carbon impurities. Therefore, irreversible capacity loss (difference between lithiation and delithiation capacity) is largest for the 500 °C sample and decreases with increasing carbonization temperature. The second lithiation/delithiation cycle reveals that the SEI layer is unstable for the 500 °C sample (additional irreversible capacity), but relatively stable for the remaining samples. The reversible capacities of the as produced high temperature (1200 and 1600 °C) carbons were similar to starch derived carbons presented by Dahn [37]. Although synthesized at a lower temperature (600 and 700 °C), as compared to many of the biomass derived carbons, both 600 and 700 °C derived carbons exhibit much higher reversible capacities with relatively good reversible-to-irreversible capacity ratio (C_{rev}/C_{irr}), with the 600 °C sample exhibiting promising performance. The initial reversible-to-irreversible capacity ratio of the 600 °C sample is relatively similar [44,53], if not better [46,47] when compare to some of the biomass derived carbons.

The rate performance of the various carbons was investigated, as shown in Fig. 2.11a (absolute capacity) and Fig. 2.11b (relative capacity). It should be noted that the first 3 cycles are ascribed to SEI layer formation and were excluded from the plots
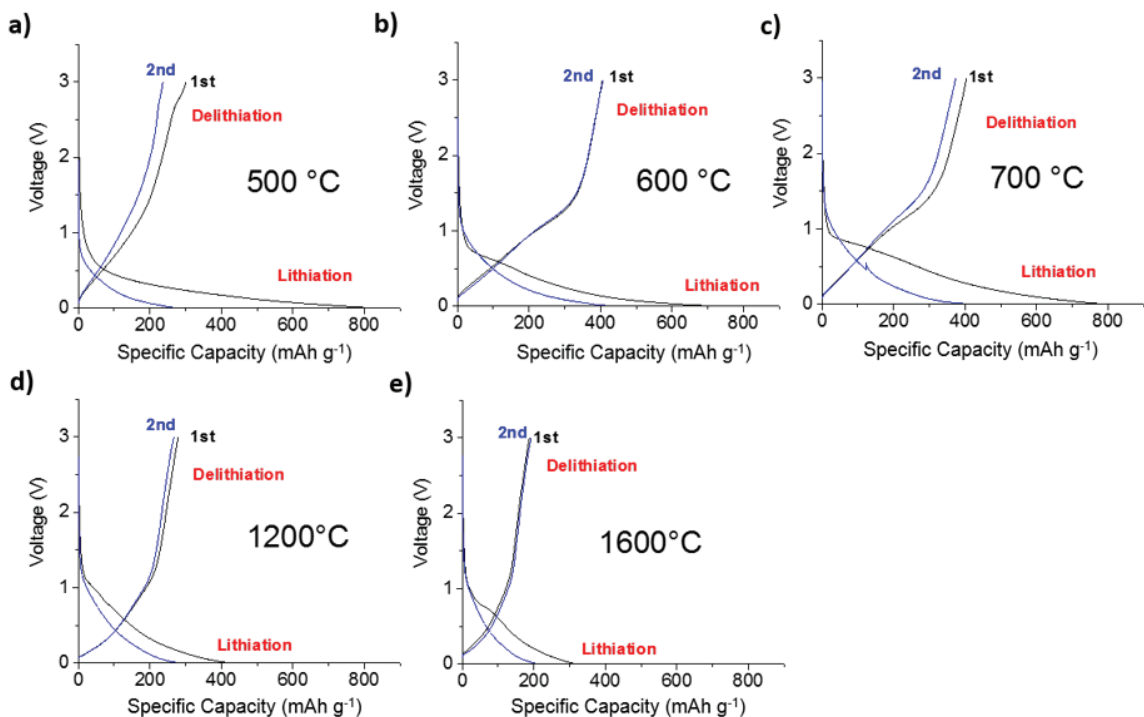
Fig. 2.10.: First and second charge-discharge characteristics of the various carbon samples prepared at different carbonization temperature a) 500 °C, b) 600 °C, c) 700 °C, d) 1200 °C, and e) 1600 °C.

for clarity purposes. The 600 °C sample shows the highest specific capacities, even at higher C-rates; capacities also recover to similar values when switching from 1C to C/10. While the annealed 1200 and 1600 °C samples exhibit lower specific capacities, their relative capacity retention is higher than that of the 600 °C. Considering the absolute and relative capacity retention during C-rate testing, the 600 °C sample exhibits the best performance.

Cycle-life testing (Fig. 2.11c) at 1C revealed that capacity of 600 °C was increasing during the first 60 cycles, reaching a final capacity which is ∼25 mAh g^{-1} higher than that of the 700 °C sample. The rise in the lithiation capacity observed in the 600 °C sample (Fig. 2.11c) can be ascribed to the delayed infiltration of electrolyte, due to the smaller pore sizes and high total pore volume [53]; whereas the rise in lithiation capacity in the 1200 and 1600 °C samples can be ascribed to the increase in defects
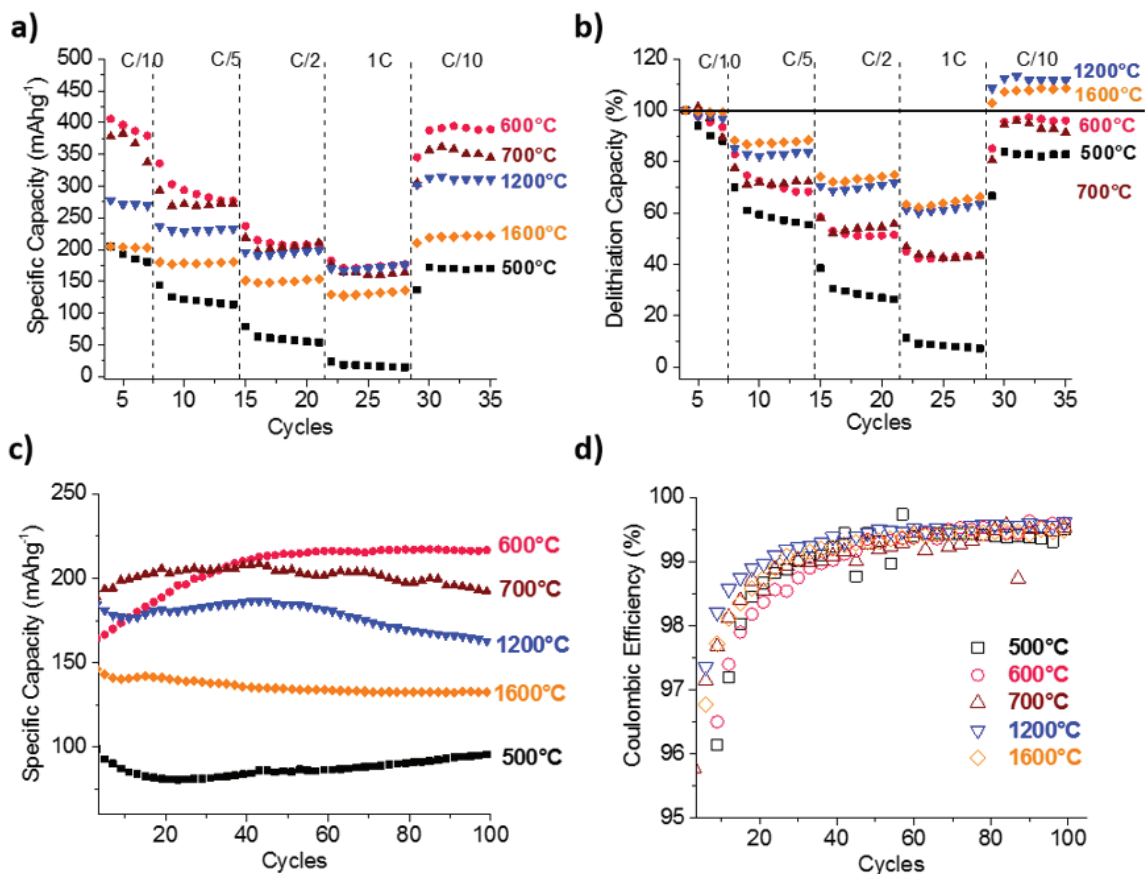
Fig. 2.11.: a) The programmed cyclic responses of the various as synthesized carbons at various C-rates (rate of charge) b) Normalization to the initial capacity of the programmed cyclic responses under various C-rates; c) Cycling performance (at 1C) of wheat flour-derived carbons; and d) Coulombic efficiency of the former cycling performance.

from the insertion/de-insertion of the lithium ions [70]. All samples showed high coulombic efficiency after ∼20 cycles (Fig. 2.11d).

Electrochemical impedance spectroscopy (EIS) studies conducted on charged cells after 30 cycles are shown in Figure 2.12. The derived kinetic parameters from the Nyquist plots are shown in Table 2.2; where the intercept at the real impedance (Z') axis in the high-frequency region, R_S is the internal resistance, which includes the solution resistance, the intrinsic resistance of the carbon materials, and the contact resistance. The first semicircle in the nyquist plot correspond to R_{SEI}, which is
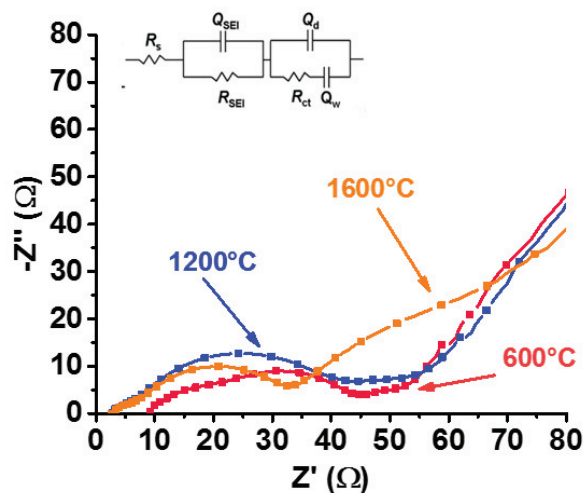
Fig. 2.12.: Nyquist plots for the 600, 1200, 1600 °C derived carbons after undergoing 30 galvanostatic cycles the equivalent circuit model is shown in the inset.

the SEI resistance, and the second semi-circle is attributed to the charge transfer resistance (R_{CT}). The Constant Phase Element (CPE) is used in the equivalent circuit model to derive the SEI capacitance (Q_{SEI}), interfacial capacitance (Q_d), and the Warburg impedance (Q_W), which measures the lithium-diffusion process within the carbon. EIS studies reveal that 600 °C derived carbons have a much higher internal resistance (R_s) as compared to the high temperature (1200 and 1600 °C) derived carbons, which can be contributed to the decrease in the Li concentrations in the solution [71] due to the formation of a relatively thick SEI layer (high R_{SEI}) and the higher intrinsic resistance of the carbon materials [47, 72]; However the 600 °C derived carbons exhibit a low charge transfer and mass transfer resistance. The 1600 °C sample showed a much higher mass transfer resistance (lower Warburg tail gradient) as opposed to the 1200 and 600 °C but has the highest electrical conductivity and lowest charge transfer resistance amongst the samples providing the good rate capability observed in the rate studies.

The large irreversible capacity loss seen in the low temperature synthesized carbons (<500 °C) has been correlated to the residual hydrogen content, which can be

Table 2.2.: Parameters values for the equivalent circuit model simulated for Fig. 2.12.

Sample	R_s (Ω)	R_{SEI} (Ω)	R_{CT} (Ω)	Q_{SEI} (S·sec^n)		Q_d (S·sec^n)		Q_w
				Y_0	n	Y_0	n	Y_0(S·sec$^{0.5}$)
600 °C	7.939	42.4	82.8	5.678×10^{-4}	0.4718	7.602×10^{-2}	0.6629	7.475×10^{8}
1200 °C	3.065	1.965	40.76	3.021×10^{-6}	1	2.187×10^{-4}	0.6902	5.158×10^{-2}
1600 °C	3.097	2.878	27.63	4.906×10^{-6}	0.9384	1.797×10^{-4}	0.7422	2.331×10^{-2}

reduced by heating to higher temperature [73]; also discussed in the thermal analysis section. Annealing at higher temperatures leads to closure of nano pores, which reduces the Li$^+$ adsorption rate dramatically. This is also supported by our BET measurements (Fig. 2.8, and Fig. 2.9), where there is an order of magnitude drop in the surface area from 700 °C to 1600 °C derived carbons (the latter being more crystalline) [74]. Although the performances of the as derived 600 °C carbons are promising, other biomass derived carbons have shown higher reversible capacities [40,49,54]; however, keeping in mind that these carbons precursors go through either acid/basic activation or cleaning process before pyrolysis.

2.4 Conclusion

This chapter presents a facile approach for the fabrication of low-cost, biomass-derived carbon from wheat flour, with promising lithium uptake. Structural studies revealed that there exists an optimal carbonization temperature around 600 °C, at which the level of disorder in the carbon exhibits high lithiation capacities. Electrochemical studies of evolving carbon produced at higher temperatures (>1000 °C) exhibited lower irreversible capacity loss, but were subject to lower reversible capacity due to closure of nano pores. Carbon samples derived at 600 °C showed capacities (390 mAh g^{-1}) exceeding that of pure graphite, as well as good cycling performance (217 mAh g^{-1} at 1C lasting for 100 cycles). The elimination of any acid or basic pre-treatment, coupled with the lower synthesis temperature make wheat-derived carbon a desirable low-cost, high capacity carbon-based anode materials. Further studies on

the particle size and existential mineral contents in the various as-derived carbons can further optimize the lithium storage and cyclability.

3. TAILORED SONOCHEMICAL ANCHORING OF NANO-SIZED V$_2$O$_5$ CATHODE PARTICLES ON GRAPHENE NANOPLATELETS FOR IMPROVED LITHIUM-ION INSERTION

Authors: Daw Gen Lim[†], Yunpu Zhao[§], Ryan A. Adams[§], Jeffrey P. Youngblood[†], and Vilas G. Pol [†], [§]

† School of Materials Engineering, Purdue University, West Lafayette, 47907, USA.
§ Davidson School of Chemical Engineering, Purdue University, West Lafayette, 47907, USA.

The text and figures presented in this chapter, in part or in full, are a reprint of the submitted manuscript, which is currently under review by *Journal of Electrochimica Acta*. Daw Gen Lim, contributed to the material synthesis, Raman microspectroscopy, powder x-ray diffraction, electrochemical studies, EM characterization and the writing of the manuscript. Yunpu Zhao assisted in the material synthesis and electrochemical characterization. Ryan A. Adams assisted in the EM characterization. Dr. Jeffrey P. Youngblood, and Dr. Vilas G. Pol are the PIs.

Abstract

Ultrasound-assisted surface modification of graphene nanoplatelets (GNPs) has made possible for in situ growth of V_2O_5 nanoparticles; homogeneously decorating inter-connected two-dimensional GNPs. The as-fabricated One-Step V_2O_5|GNPs nanocomposite allows higher electrical conductivity, as well as high Li^+ insertion/ extraction kinetics achieving the theoretical cathode capacity, 297 mAh g^{-1} (insertion/extraction of 2 Li^+ ions). Under 50 mA g^{-1} constant current density, the sonochemically tailored One-Step V_2O_5|GNPs nanocomposite achieved 248 mAh g^{-1} specific cathode capacity; retaining 83% of initial capacity after 50 cycles, with >98.4% coulombic efficiency. The hybrid cathode nanocomposite also achieved 65% capacity retention even when the current density was increased 20 times (10 to 200 mA g^{-1}). On the other hand, Two-Step (sonochemical synthesis of 200 nm V_2O_5 particles followed by its deposition on GNPs) V_2O_5|GNPs composite cathode yielded lower specific capacity (225 mAh g^{-1}) at 10 mA g^{-1} current density. Varying the GNPs wt.% also revealed that there are diminishing improvements in the electrochemical performance of the cell after 20 wt.% GNPs in the V_2O_5|GNPs nanocomposites.

3.1 Introduction

The ever-rising demands for lithium-ion batteries (LIBs), have sparked the search for materials that are high energy density, inexpensive, reliable, longer lasting, and environmentally benign [32, 34, 75]. In the Li-ion cell, the current limiting factor in the output capacity of the cell is governed mainly by the cathode material and not the anode [33, 35, 76]. Of all the various explored cathode materials, vanadium oxide (V_2O_5) has the ability to intercalate up to 3 Li^+ ions, boasting one of the highest theoretical capacities of 440 mAh g^{-1} (3 Li^+ ions) and 294 mAh g^{-1} (2 Li^+ ions) [77, 78]; as compared to other known cathode materials such as $LiCoO_2$ [75], $LiNiO_2$ [76], $LiNi_{1/3}Mn_{1/3}Co_{1/3}O_2$ [79, 80], $LiFePO_4$ [81], $LiMn_2O_4$ [82] that can only

deliver a limited practical capacity in the range of 100 to 170 mAh g^{-1}, which makes V_2O_5 a good candidate for LIBs.

However, the application of V_2O_5 electrodes in rechargeable LIBs has been impeded by its low diffusion coefficient for lithium ions [83], poor electronic conductivity in crystalline form [84], and poor structural stability (when cycled at <2 V) [85, 86]. Various strategies have been taken to improve the electrochemical performance of V_2O_5 . For example: 1) Manipulating the materials size and geometry to decrease the Li$^+$ diffusion path, e.g. nanorods [87], nanowires [88, 89], nano/microspheres [90–97], nanoribbons [98], nanotubes [99], nanosheets [100, 101]; 2) Hybridizing the V_2O_5 with various carbonaceous materials to improve conductivity, e.g. MWCNT [102, 103], graphene/graphene-nanostructures [104–106], porous carbon [107–109]; 3) Adding dopants into V_2O_5 to increase Li$^+$ insertion/extraction kinetics e.g. Mn [110]40, Sn [111], and Na [112]; 4) Modification of surfaces to improve Butler-Volmer kinetics by inducing various defects [101, 113, 114]. However, some of these nanostructures are unable to realize high capacities or suffer from capacity fading due to aggregation attributed by their high surface energies [88, 96, 99, 105, 107].

Several synthesis methods, such as sol-gel [103, 106, 109] and solvothermal [107, 115], etc. (involves multiple synthesis reactions) have been applied to the fabrication of various form of V_2O_5 /Carbon composites. Studies have shown that the sonochemical method is superior to the other techniques in the fabrication of nanocomposites by insertion of nanoparticles into mesoporous materials [116], homogenously deposit nanoparticles on various surfaces [117, 117, 118], and the preparation of amorphous products [119]. Compared to the other synthesis methods, the sonochemical route exhibits the merits of time, simplicity, and energy efficiency [120–122].

Recent studies demonstrated that 2D graphene sheets improve effective conductivity of composites, as compared to other carbon structures, e.g. CNTs, graphene nanoribbons, porous carbon, graphite [106, 123]. Using high aspect ratio plate-like structures as a backbone for a conductive network allows for better orientation control during electrode fabrication, where the graphene platelets will lie flat, exposing a

larger planar surface that is decorated with V_2O_5 nanoparticles. Herein, we present a 2D network V_2O_5 decorated graphene nanoplatelet composite, via two facile scalable sonochemical methods (Two-Step and One-Step). The goal of this facile approach aims to improve the Li-insertion and extraction kinetics in V_2O_5, by improving the overall conductivity of the material and decreasing the Li-diffusion path.

3.2 Experimental

3.2.1 Material Synthesis

VCl_3 (Sigma Aldrich) was used as the metal precursor for V_2O_5 preparation and commercially available graphene nanoplatelets (Strem Chemicals Inc.) were used as the conducting substrate. All the chemicals were utilized without any prior treatment. Ammonium hydroxide and ethanol were all supplied by Alfa Aesar. Sonication (Sonics Ultrasonic Processor) parameters for the following synthesis procedures were fixed at 20 kHz frequency, operating at a power level of 50% (375 W).

For the Two-Step process, in the typical synthesis of V_2O_5 nanoparticles, approximately 0.3 M of VCl_3 in water purified by a Barnstead MicroPure system (18.2 MΩ-cm) was prepared. While the solution is stirring vigorously, several drops of NH_4OH were added until a pH value of 3–4 was achieved. The solution was then sonicated in an ice bath for $\sim$30 mins, while adding NH_4OH drop by drop until a final pH value of $\sim$9, which forms a dark green precipitate. The precipitate was then collected via centrifugation, and subsequently washed in water and ethanol several times. The washed precipitate was then dried in a vacuum oven at 80 °C for $\sim$12 hrs. The dried precipitate was further calcined in a tube furnace at 400 °C for 4 hrs under ambient air conditions to form V_2O_5 nanoparticles. Preparation of V_2O_5 |GNPs composite: Graphene nanoplatelets (GNPs) are adopted as support for the fabrication of V_2O_5 |graphene composite. In a typical synthesis, GNPs were suspended in $\sim$100 ml of ethanol and sonicated for $\sim$10 min. Subsequently, V_2O_5 nanoparticle were suspended in $\sim$20 ml of MicroPure water, and stirred for $\sim$10 min. Both suspensions

were then mixed together under a constant sonication for ∼1 hour to form a dark green V_2O_5|GNPs composite. The graphene content was then controlled by adjusting the mass ratio of GNPs and V_2O_5 nanoparticles. The composite was collected by centrifugation and dried in a vacuum oven under 80 °C for ∼12 hours.

For the One-Step process, approximately 3 mol of VCl_3 was dissolved in 30 ml water and stirred for 10 min to form VCl_3 solution. GNPs were dispersed in 100 ml ethanol and sonicated for 10 minutes, and then the VCl_3 solution was added into the GNPs suspension, with subsequent sonication for 30 min in an ice bath until a homogeneous suspension was obtained. The suspension was heated on a hot plate with constant stirring until most of the solvent was evaporated and then dried in a vacuum oven at 80 °C overnight to get as-prepared composite. The V_2O_5|GNPs composite was obtained by annealing as-prepared composite at 400 °C for 4 hrs in Ar atmosphere followed by another 4 hrs at 400°C in ambient air. The graphene to V_2O_5 content was then controlled by adjusting the weight fraction of the GNPs to the concentration of the VCl_3 solution. In this case, 200 mg of GNPs in the solution will produce GNPs: V_2O_5 a weight ratio of ∼40 wt.%.

3.2.2   Structural Characterization

Powder x-ray diffraction (pXRD) was utilized to characterize the crystalline phase using the Bragg-Brentano method (Rigaku SmartLab X-Ray Diffractometer). A CuK X-ray source (= 0.154 nm) was used to obtain the X-ray diffraction (XRD) patterns (2θ = 10–80°) of pristine V_2O_5, pristine graphene nanoplatelets and V_2O_5|GNPs composites at a scanning rate of 5°/minute. Thermogravimetric analysis (Instrument Specialists Incorporated TGA i-1000) was conducted on V_2O_5|GNPs composites to determine the graphene content. A range of 25 °C to 1000 °C was used with 10°C/minute heating rate with 10 cm^3 min^{-1} of air and 5 cm^3 min^{-1} of argon flow. Transmission electron microscope images (TEM and HRTEM) were taken using the FETEM mode of a Titan 80–300 kV Environmental Transmission Electron

Microscope. Samples were prepared through dispersion of solid powders in ethanol via ultrasonication for 2 minutes. A few drops of the suspension were loaded onto a carbon-coated 400-mesh copper grid (Ted Pella) and dried at room temperature prior to loading into the sample holder for the machine. Scanning electron microscopy (FE-SEM) images were recorded using a Hitachi S-4800 microscope. Raman spectra of the V_2O_5 |GNPs composites, pristine graphene nanoplatelets, and pristine V_2O_5 nanoparticles, were collected (Thermo Scientific DXR) with a 532-nm laser at 3 mW cm^{-2}, using a 900 l/mm grating. Each spectrum was collected within a laser exposure time of ∼30 sec.

3.2.3   Electrochemical Characterization

The composite electrodes were prepared by with a weight ratio of 80 wt.% active material (V_2O_5 |GNPs nanocomposite), 10 wt.% conductive carbon (Super P), and 10 wt.% carboxymethylated cellulose (CMC) with a styrene-butadiene rubber (SBR) of 1:1 ratio. Using DI water as the solvent, the slurry was mixed for 30 minutes, and coated onto aluminum foil using a doctor blade. The laminate was dried in a vacuum oven at 80 °C for ∼12 hours. From the laminate, electrodes of 12 mm diameter were punched out with an active material density of about 1.5 mg cm^{-2}. Electrochemical tests and cycling are performed on a coin-type 2032 with lithium metal as the counter electrode. Celgard 2500 polypropylene was used as the separator and 1 M LiPF$_6$ in a 1:1 mixture of ethylene carbonate (EC) and diethyl carbonate (DEC) was utilized as the electrolyte. Cells were assembled in a high-purity glovebox (99.99%) with oxygen and water sensors ensuring O_2 and H_2O concentrations of <5 ppm. Electrochemical impedance spectroscopy studies (Gamry Reference-600 electrochemical workstation) were evaluated for the initial first 3 cycles from 2.0–4.0 V with an oscillation amplitude of 10 mV, over the frequency of 0.01 Hz to 106 Hz. Galvanostatic cycling was performed at room temperatures, using an Arbin BT2043

model with a voltage window of 2.0–4.0 V at various current densities. All potentials mentioned are vs. Li/Li$^+$ in this paper unless otherwise stated.

3.3   Results and Discussion

Two different sonochemical synthesis approaches were taken in the preparation of V$_2$O$_5$|GNPs nanocomposites as a comparative study, namely the One-Step and Two-Step synthesis. The schematic of the preparation processes is illustrated in Figure 3.1. Figure 3.1a, depicts the Two-Step synthesis process, where V$_2$O$_5$ nanoparticles were obtained by sonicating VCl$_3$ solution, while adding NH$_4$OH to form nano-sized V(OH)$_3$, which was then calcined in ambient air to form V$_2$O$_5$ nanoparticles. The as-synthesized V$_2$O$_5$ nanoparticles were then physically mixed with the as-purchased graphene nanoplatelets (GNPs) under sonochemical treatment.
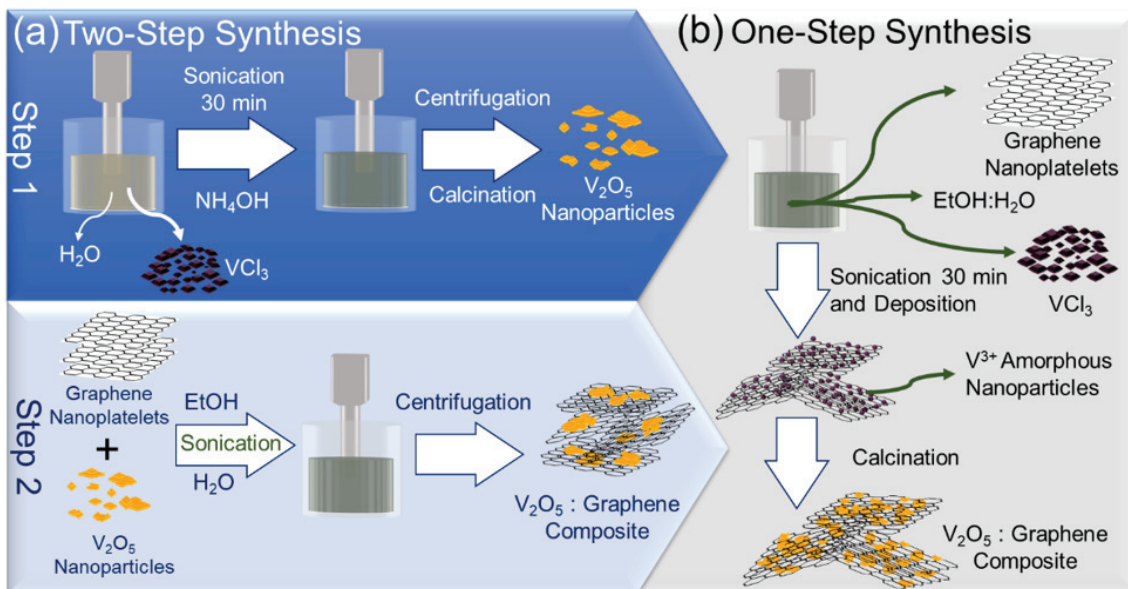
Fig. 3.1.: Schematic diagram for the preparation of V$_2$O$_5$|GNPs by (a) Two-Step synthesis, and (b) One-Step synthesis.

Figure 3.1b) shows the One-Step synthesis process, where GNPs were added in a VCl$_3$ solution dissolved in water and ethanol. The solution is then sonicated to

initiate the mixing process, followed by a deposition and calcination process. In the comparative study for both One-Step and Two-Step nanocomposites, the V_2O_5 to GNPs weight ratio is 3:2. The weight fraction of the Two-Step synthesis process is controlled by the weight of the as synthesized V_2O_5 nanoparticles and the graphene nanoplatelets before mixing. The One-Step synthesis process however is more complicated and is carefully tuned based on the concentration of the VCl_3 solution; the final product is then characterized by TGA (Figure 3.2) in ambient air, where GNPs will be oxidized into CO_2, leaving the remaining V_2O_5 nanoparticles.
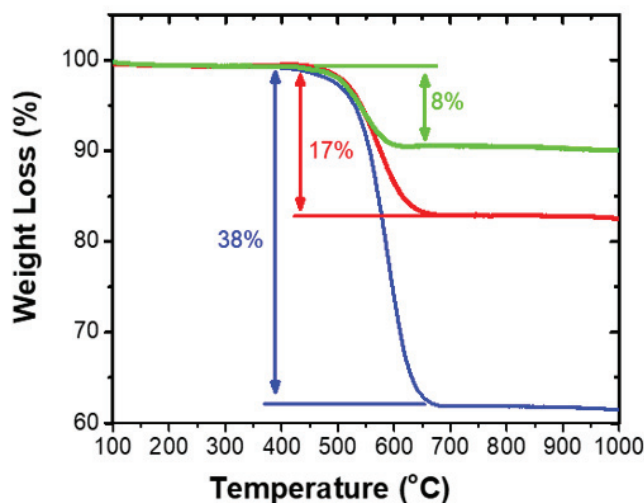
Fig. 3.2.: TGA analysis for One-Step synthesized GNPs|V_2O_5 nanocomposite with varying GNPs wt.% in air.

The morphology of the Two-Step and One-Step as-synthesized nanocomposites were characterized by SEM (Fig. 3.3a and b) and TEM (Fig. 3.3c). In Fig. 3.3a, the Two-Step synthesized nanocomposite clearly showed some uneven agglomeration of V_2O_5 nanoparticles on top of the graphene nanoplatelets after undergoing the sonochemical mixing process. Fig. 3.3b and c, depicts a much more homogeneous decoration of V_2O_5 nanoparticles on the graphene nanoplatelets, with the V_2O_5 nanoparticles having an average size of about 200 nm.
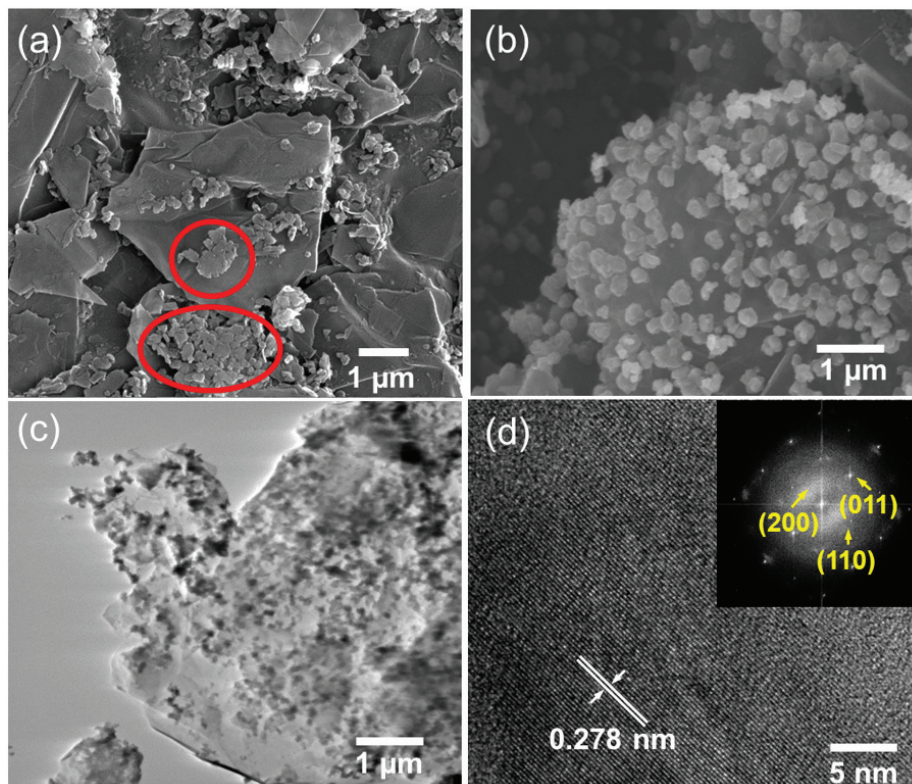
Fig. 3.3.: SEM micrographs of a) Two-Step synthesized V_2O_5|GNPs composite and b) One-Step synthesized V_2O_5|GNPs composite; c) TEM image of One-Step synthesized V_2O_5|GNPs composite; d) HRTEM of One-Step synthesized V_2O_5|GNPs composite and corresponding FFT image (inset).

The homogeneity of the distribution of V_2O_5 nanoparticles is elucidated in Figure 3.4a and b, which illustrate the mapping of elemental vanadium on the GNPs for the One-Step and Two-Step synthesized nanocomposite, respectively. The superior morphology of the One-Step synthesis process may be attributed to the high energy acoustic cavitation bubble implosion near the GNPs surfaces; creating tiny defects on the GNPs surface [119, 124]. It is also known that these extreme conditions dissociate water to form OH^- and H^+ radicals, and can react with the GNPs, which are usually effective in breaking C-C bonds [125–127]. This surface modification of the GNPs could result in various functional groups -OH, -COO-, -CO, etc., allowing the effective anchoring of the vanadium ions $(V(H_2O)_6]^{3+})$ [103, 106].

The subsequent, thermal reduction and oxidation processes result in the formation of homogeneously anchored V_2O_5 nanoparticles. To the contrary, in the Two-Step process, the simultaneous sonication of the V_2O_5 nanoparticles and GNPs, did not prevent the agglomeration of V_2O_5, resulting in non-homogeneous deposition of V_2O_5 on the GNPs substrate; but allowed the fusing of the V_2O_5 nanoparticles (indicated by circles in Fig. 3.3a). Though defects would have been created on the GNPs surface, these defects were too small to trap the large agglomerated/fused nanoparticles. Hence, after the continuous sonochemical treatment, inhomogeneous large aggregates of V_2O_5 nanoparticles were found on the GNPs surfaces.
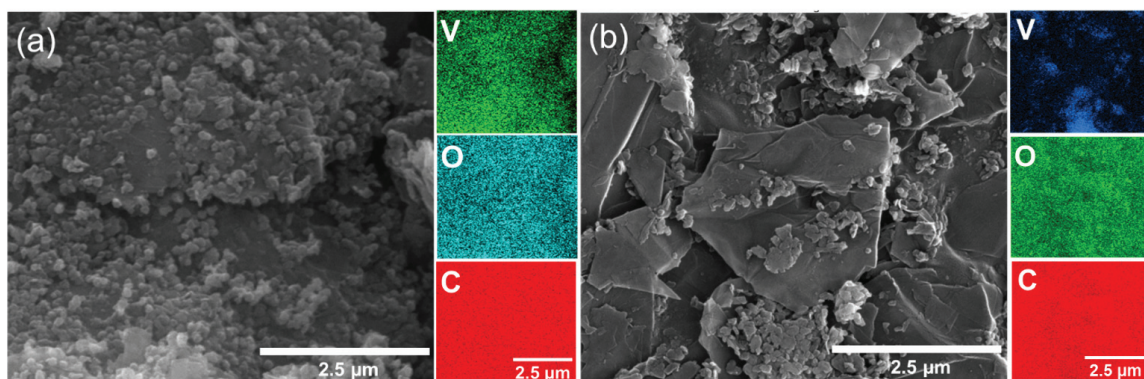
Fig. 3.4.: SEM micrograph and their respective EDS maps of a) One-Step and b) Two-Step synthesized V_2O_5|GNP composite clearly showing the distribution of V_2O_5 nanoparticles.

HRTEM (Fig.3.3d) for the One-Step synthesized V_2O_5|GNPs composite shows a V_2O_5 (011) crystal plane with an interlayer spacing of about 2.78 Å. The corresponding fast Fourier-transform (FFT) pattern of the image can be indexed to the diffraction spots of the Pmmn V_2O_5 structure. The orthorhombic crystal structure of the V_2O_5 nanoparticles is further confirmed by both XRD patterns and Raman spectra shown in Figure 3.5a and b. Commercially purchased graphene nano-platelets and V_2O_5 nanoparticles were also characterized by XRD and Raman, as a reference to our as-synthesized composite materials. From the XRD patterns of the One-Step and Two-Step synthesized V_2O_5|GNPs nanocomposites, it is observed that the

V_2O_5 nanoparticles have a preferred (110) planar configuration. Based on the Scherrer equation, both samples crystallites are found to be $\sim$20 nm.
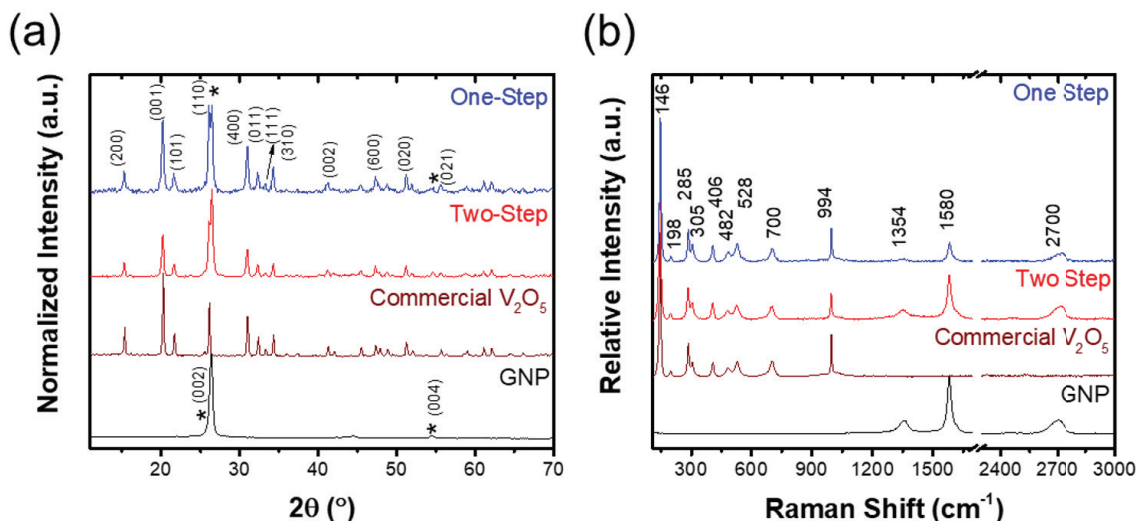
Fig. 3.5.: a) X-ray diffraction patterns and b) Raman spectra of One-Step and Two-Step synthesized V_2O_5|GNPs composite; and commercially purchased samples as material reference.

Figure 3.5b illustrates the Raman spectra of the nanocomposites, the as-purchased graphene nanoplatelets, and V_2O_5 nanoparticles. The orthorhombic phase of V_2O_5 typically has nine characteristic peaks [128–131]; the peak shift, vibrational modes, and the respective bond species are tabulated in Table 3.1. The peaks of relative interest in the V_2O_5 Raman spectra are the predominant low wavenumber peak at 145 cm^{-1}, resembling the translational modes of the V_2O_5 unit, which reflects the long-range planar ordering of V_2O_5 sheets; and the peak at 995 cm^{-1}, which corresponds to all in-phase stretching vibration of the shortest apical V-O bonds. Additionally, the nanocomposite samples have two extra peaks at $\sim$1350 cm^{-1} and 1580 cm^{-1}, which belongs to the graphene nanoplatelets (GNPs). In comparison, the collected GNPs Raman signal is much higher in the Two-Step as compared to the One-Step, which is attributed to the homogeneously decorated GNPs; preventing much of the GNPs Raman scattering.

Table 3.1.: Typical Raman shift and their vibrational modes between the atom species of the orthorhombic V_2O_5 phase.

Raman Shift (cm^{-1})	Raman Mode	Bonds
146	$B_{1g}+B_{2g}$	V-O-V
198	A_g+B_{2g}	V-O
285	B_{2g}	O_3-V-O_2
305	A_g	V-O
406	A_g	V-O_2-V
482	A_g	V-O
528	A_g	V-O_2
700	B_{2g}	V-O_1
994	A_g	V=O

The typical charge/discharge curves of the One-Step nanocomposite at a fixed current density of 50 mA g^{-1} at various cycle stages are shown in Fig. 3.6a; the One-Step synthesized nanocomposite achieved a relatively high discharge capacity of $\sim$225 mAh g^{-1} after 40 cycles. The differential capacity plot from the second conditioning cycle of the One-Step and Two-Step synthesized nanocomposite is illustrated in Fig. 3.6b, showing the 3 evident cathodic peaks (3.39, 3.19, and 2.32 V); which indicates the multistep reduction process of the V^{5+} ions in the V_2O_5 lattice, indirectly corresponding to the phase change from α-$Li_xV_2O_5$ ($0 < x < 0.35$) to -$Li_xV_2O_5$ ($0.35 < x < 0.7$), then δ-$Li_xV_2O_5$ ($0.7 < x < 1$), and finally γ-$Li_xV_2O_5$ ($1 < x < 2$). Subsequently, the peaks located at 2.54, 3.22, and 3.43 V are attributed to the extraction of the Li-ions allowing for the transformation of γ-$Li_xV_2O_5$ ($1 < x < 2$), to δ-$Li_xV_2O_5$ ($0.7 < x < 1$), to -$Li_xV_2O_5$ ($0.35 < x < 0.7$), and finally α-$Li_xV_2O_5$ ($0 < x < 0.35$) [77, 78, 85, 86, 107, 132].

Comparing both differential capacity plots, the peak differential current for the One-Step is much higher ($\sim$4$\times$) than that of the Two-Step nanocomposites, indicating that the homogeneously distributed V_2O_5 nanoparticles on the GNPs have resulted in higher charge transfer and demonstrate less polarization [87]. This is also evident in the impedance spectra (Fig. 3.7). The impedance spectra show that there is an extra semicircle in the medium frequency region for the Two-Step as opposed to the
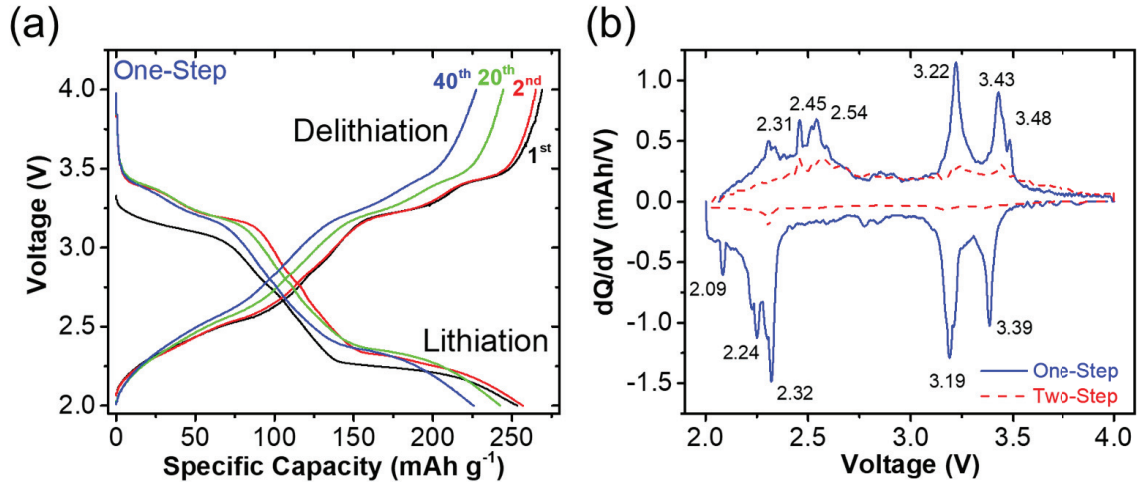
Fig. 3.6.: a) A typical galvanostatic lithiation, delithiation curve for One-Step synthesized V_2O_5 |GNPs nanocomposite at 50 mA g^{-1}; b) Differential capacity plot for both One-Step and Two-Step synthesized V_2O_5 |GNPs nanocomposites.

One-Step nanocomposite. Hence, two-different equivalent circuit models have been used to model the behavior, as shown in Fig. 3.7 inset a) One-Step and b) Two-Step [106, 133].

The total resistance of the cell is characterized by the following parameters: R_s is the internal resistance of the cell, R_e is the resistance of the electrolyte, R_{ct} is the charge transfer resistance at the particle surface. A constant phase element is used in the model due to particle surface morphology, where Q_s is the capacitance arising from the adsorption of Li$^+$ on the particle surface, Q_d is the double layer capacitance due to the accumulation of charged species in the electrolyte at the interface. W is the Warburg impedance due to the Li-ion diffusion within the particle and C_L is the insertion capacitance. The additional C_4 R_4 is inserted into the circuit for the Two-Step V_2O_5 |GNPs nanocomposite to simulate the extra semicircle in the medium frequency region. Based on the fitting of the impedance spectra, both cells showed similar internal resistance at 2.6 and 3.2 Ω, for One-Step and Two-Step nanocomposites cells, respectively. The additional R_4 term in the Two-Step V_2O_5 |GNPs nanocomposite, suggest that another surface charge transfer takes place
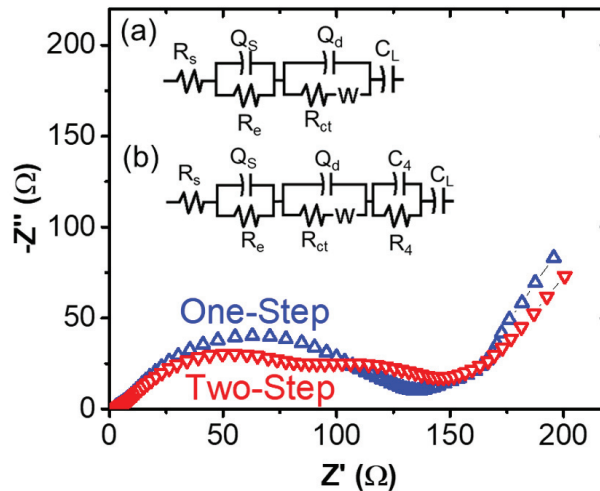
Fig. 3.7.: Impedance spectra (Nyquist plots) for One-Step and Two-Step synthesized V_2O_5 |GNPs composite at an OCV of 3V after the 3rd cycle. Inset shows the equivalent circuit model for a) One-Step and b) Two-Step synthesized V_2O_5 |GNPs nanocomposite. Parameters of the model are listed in Table 3.2.

due to the large inhomogeneous V_2O_5 particles on the surface of the GNPs, which is much higher than the One-Step nanocomposite (132.6 and 123.8 Ω, respectively). The Warburg impedance of Two-Step (W= 0.03801 S·sec$^{0.5}$) synthesized nanocomposite is also higher (lower Warburg tail gradient) than the One-Step (W= 0.04023 S·sec$^{0.5}$) synthesized nanocomposite. From the simulated equivalent circuit model, it is conclusive that the One-Step synthesized nanocomposite shows better overall electronic conductivity as well as a shorter diffusion path for the Li$^+$ ions. The improved conductivity for the One-Step synthesized V_2O_5 |GNPs nanocomposite is also comparable [106], if not better [105, 107] than other carbonaceous hybrids.

Lithiation behavior at low current density (10 mA g^{-1}) of the One-Step (Fig. 3.8a), and Two-Step (Fig. 3.8b) shows the One-Step nanocomposite achieved the theoretical capacity of 294 mAh g^{-1}, where 2 Li$^+$ ions are intercalated, and when discharged at a higher rate (200 mA g^{-1}), showed ∼65% of capacity retention (195 mAh g^{-1}); whereas the Two-Step synthesized capacity shows only 45% of the capacity retention (relative to theoretical capacity 294 mAh g^{-1}). The rate capability of the

Table 3.2.: Parameter values for the equivalent circuit model simulated for Fig. 3.7

Parameters		Sample	
		One-Step	Two-Step
R_s (Ω)		2.571	3.232
R_e (Ω)		2.764	3.468
R_{ct} (Ω)		123.8	87.6
R_4 (Ω)		N/A	45
Q_s (S·sec^n)	Y_0	6.622×10^{-5}	2.293×10^{-6}
	n	0.7177	0.9354
Q_d (S·sec^n)	Y_0	1.501×10^{-6}	7.133×10^{-5}
	n	0.9897	0.7202
C_4 (S·sec^n)	Y_0	N/A	1.579×10^{-3}
	n	N/A	0.8075
C_L (F)		5.592	0.8086
W (S·sec$^{0.5}$)		0.04023	0.03801

One-Step and Two-Step synthesized V_2O_5 |GNPs nanocomposites are compared in Fig. 3.8c, showing a relative discharge capacity (relative to capacity achieved at 10 mA g^{-1}) utilization of 65% and 59% at higher current densities (200 mA g^{-1}), respectively. Both the One-Step and Two-Step V_2O_5 |GNPs nanocomposites still achieved higher initial discharge capacity (at a voltage range of 2–4 V) as compare to various nanostructured V_2O_5 / Hybrid studies (shown in Fig 3.10).

From the cyclic studies (Fig. 3.8c), the One-Step and Two-Step synthesized nanocomposite achieve a capacity of 248 mAh g^{-1} and 224 mAh g^{-1} under constant current density of 50 mA g^{-1}. After 50 cycles of continuous cycling, the One-Step showed a higher capacity retention of 83%; whereas the Two-Step synthesized nanocomposites degraded to 70%. The decay rate for the One-Step and Two-Step nanocomposite is $\sim$0.34 %/cycle and 0.6%/cycle, respectively. Both samples achieved a coulombic efficiency of $\sim$98.4%.

Further studies were then conducted on the One-Step synthesized V_2O_5 |GNPs nanocomposite with varying GNPs wt.%. The weight fraction for the GNPs and V_2O_5 were determined by TGA analysis (Figure 3.2), where the following samples: 10%, 20%, and 40% corresponds to the approximate weight loss (8%, 17%, and 38%,
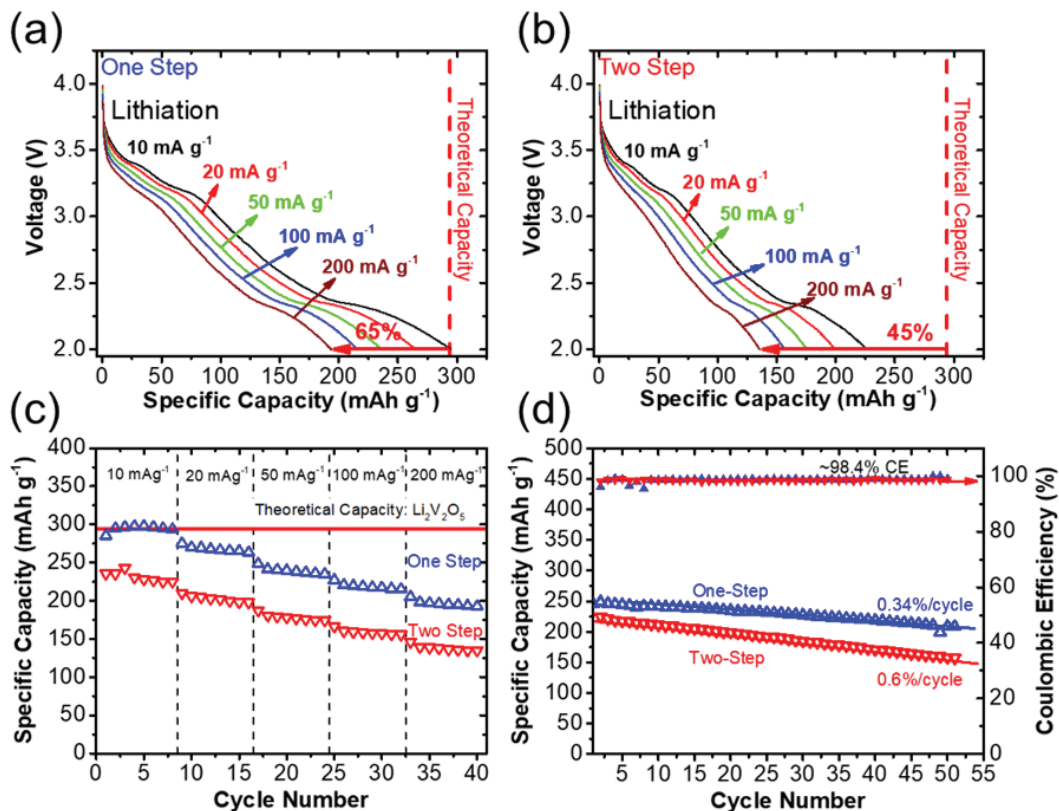
Fig. 3.8.: Discharge profiles of a) One-Step and b) Two-Step synthesized V_2O_5|GNPs nanocomposites c) Lithiation behavior for both the One-Step and Two-Step V_2O_5|GNPs nanocomposites at different current densities; d) Cyclic performance of One-Step and Two-Step synthesized V_2O_5|GNPs nanocomposites at a fixed current density of 50 mA g^{-1}.

respectively) that occurs during the oxidation of GNPs, which determines the GNPs to V_2O_5 weight ratio. The initial impedance spectra for the varying V_2O_5: GNPs nanocomposites were collected (Fig. 3.9a), utilizing the same equivalent circuit model shown in Fig. 3.7a), the simulated parameters (Table 3.3) illustrate that there is a decrease in the total resistance of the cell, with increasing GNPs content. From the model, it is observed that the key parameter affecting the total resistance of the cell is the charge transfer resistance (R_{ct}); where a significant decrease in the charge transfer resistance is observed between 10 and 20 wt.% GNPs contents (438.6 and 266.2 Ω, respectively), but from 20 to 40 wt.% (266.2 and 127.4 Ω, respectively)
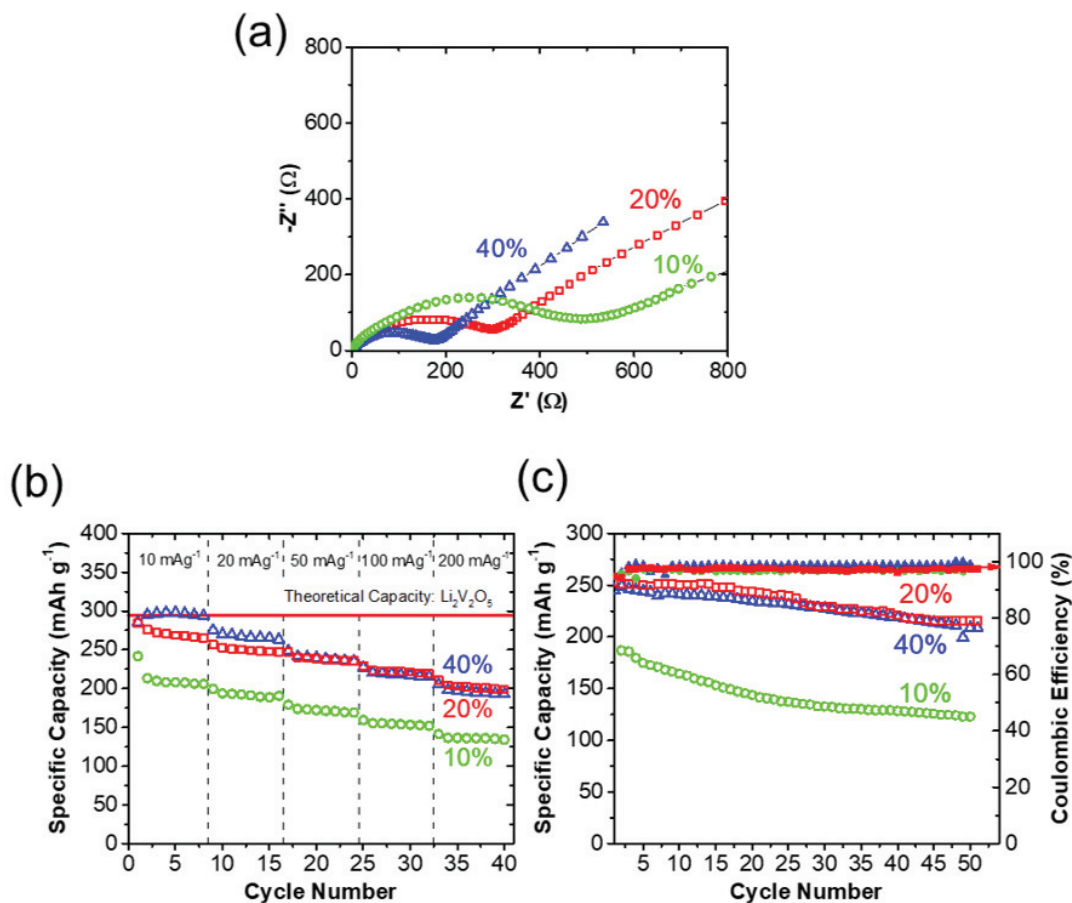
Fig. 3.9.: a) Electrochemical impedance spectra (Nyquist plots) for the One-Step V_2O_5|GNPs nanocomposites with varying GNPs wt.%. at an OCV of 3V for the initial cycle; parameters of the model are listed in Table 3.3; b) Lithiation behavior at varying current densities; c) Cyclic performance at 50 mA g^{-1} for One-Step V_2O_5|GNPs nanocomposites with varying GNPs wt.%.

a diminishing GNPs wt.% to charge transfer capability is observed. This trend is also true for the Warburg impedance, where the Warburg impedance plateau after 20 wt.% GNPs. From the rate capability and cyclic study (Fig. 3.9b and 3.9), it is observed that the 10% GNPs|V_2O_5 One Step nanocomposite is struggling to achieve a higher capacity. It is also observed that the 20% performs comparably to the 40% GNPs|V_2O_5 One-Step nanocomposite, especially at higher C-rates.

Table 3.3.: Parameter values for the equivalent circuit model simulated for Fig. 3.9a

Parameters		Sample		
		10%	20%	40%
R_s (Ω)		1.866	1.885	1.526
R_e (Ω)		56.94	17.41	32.6
R_{ct} (Ω)		438.6	266.2	127.4
Q_s (S·sec^n)	Y_0	5.424×10^{-6}	1.217×10^{-5}	1.764×10^{-5}
	n	0.8964	0.871	0.8289
Q_d (S·sec^n)	Y_0	3.198×10^{-5}	4.32×10^{-5}	5×10^{-5}
	n	0.7477	0.7251	0.7635
C_L (F)		5.406	5.473	6.21
W (S·sec$^{0.5}$)		5.23×10^{-3}	6.905×10^{-3}	8.122×10^{-3}

Overall the 2D graphene nanoplatelet backbone demonstrated higher electrical conductivity for the composite, as compared to the other carbonaceous materials e.g. Graphene nanoribbon [105], CNTs [103], and carbon-coated [107]. Subsequently, utilizing the One-Step synthesis process V_2O_5 nanoparticles homogeneously anchored on the surface of the inter-connected 2D graphene nanoplatelets, allow higher charge transfer and an improved Warburg impedance; effectively achieving the theoretical capacity (insertion/extraction of 2 Li$^+$ ions) for the nanocomposite. From varying the GNPs wt.%, it is observed that there is a critical GNPs wt.%, that allows for the lower percentage used of GNPs in the composite, but still achieving a desirable electrochemical performance. However, the exposed V_2O_5 nanoparticles on the graphene nanoplatelets are subjected to large electrochemical induced mechanical stresses from the high current densities [134], which can lead to pulverization, or enabling particles to dislodge from the surface of the graphene sheet. This is more evident when V_2O_5 nanoparticles were anchored to a curved surface (CNT), resulting in a large decay rate of 15%/cycle [103]. Present studies leave much to be desired for enabling fast Li$^+$ extraction/insertion, in the electrodes, while allowing high capacity utilization. The comparison of the various strategies in Fig. 3.10 may provide a better direction to enable the synthesis of V_2O_5 materials that are able to meet such demands.
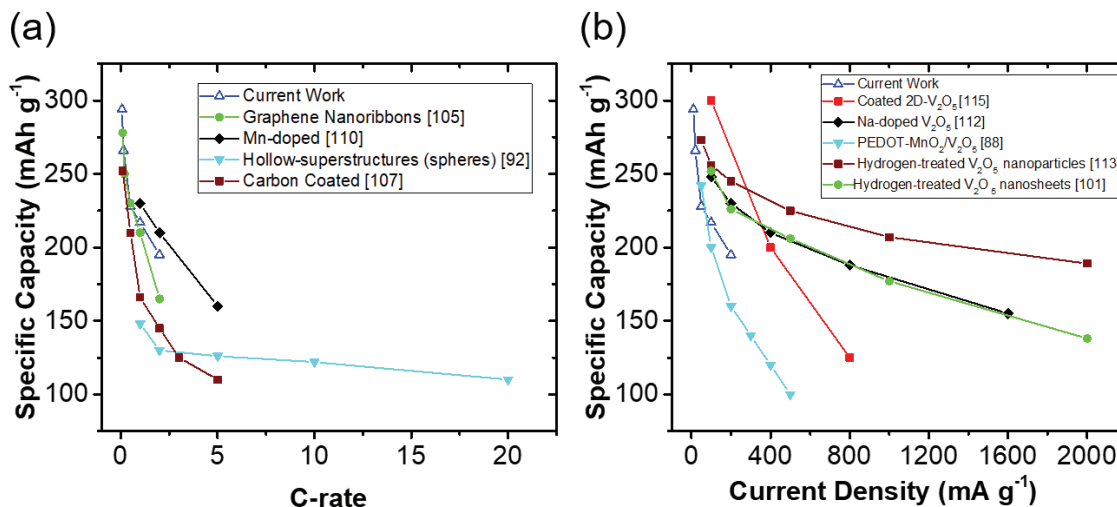
Fig. 3.10.: Rate capabilities measured in a) C-rates, and b) Current density of various V_2O_5 nanostructures and Hybrids, compared to our existing work. All cells compared here are cycled against a lithium electrode at a 2–4 V window.

3.4   Conclusion

A tailored sonochemical approach to synthesize V_2O_5 decorated 2D graphene nanoplatelets with improved lithium storage properties have been demonstrated. By inducing defects on the surface of graphene nanoplatelets via sonochemistry, homogeneously anchored V_2O_5 nanoparticles have enabled the composite to achieve high utilization of its Li-ion storage sites (294 mAh g^{-1}) for more than 5 cycles. When cycled at C/2, the material exhibits a low decay rate of 0.34%/cycle. The improvements are attributed to the increase in electronic conductivity and shorten Li$^+$ ion diffusion path in the composite material. However, exposed surface nanostructures and weak bonding have limited the rate capabilities of the material, due to large chemo-mechanical stresses from high rate insertion/ extraction of Li$^+$ ions. By varying the GNPs content, a critical wt.% of GNPs:V_2O_5 is determined (20 wt.%), where there is a diminishing improvement in the electrochemical performance. Further studies on controlling the V_2O_5 nanoparticles and its adhesion to the GNPs will allow for better rate capabilities.

4. INVESTIGATION OF SmNiO$_3$ LITHIUM-ION ELECTROCHEMICAL PROPERTIES AND ITS FEASIBILITY AS A THIN-FILM SOLID-STATE ELECTROLYTE.

The text and figures presented in this chapter, in part or in full, are a reprint of the submitted manuscript titled:

Strongly Correlated Perovskite Lithium-ion Shuttles, which is currently under review by the *Proceedings of the National Academy of Sciences of the United States of America* (PNAS).

Authors: Yifei Sun[a], Michele Kotiuga[b], Dawgen Lim[a], Badri Narayanan[c], Mathew Cherukara[d], Zhen Zhang[a], Yongqi Dong[d], Ronghui Kou[d], Cheng-Jun Sun[d], Qiyang Lu[e,f], Iradwikanari Waluyo[g], Adrian Hunt[g], Hidekazu Tanaka[h], Azusa N. Hattori[h], Sampath Gamage[i], Yohannes Abate[i], Vilas G. Pol[j], Hua Zhou[d], Subramanian KRS Sankaranarayana[k], Bilge Yildiz[e,f,l], Karin M. Rabe[b], Shriram Ramanathan[a]

a) School of Materials Engineering, Purdue University, West Lafayette, Indiana 47907, USA

b) Department of Physics and Astronomy, Rutgers, The State University of New Jersey, NJ 08854, USA

c) Materials Science Division, Argonne National Laboratory, Argonne, Illinois 60439, USA

d) X-ray Science Division, Advanced Photon Source, Argonne National Laboratory, Argonne, Illinois 60439, USA

e) Laboratory for Electrochemical Interfaces, Massachusetts Institute of Technology, Cambridge, Massachusetts 02139, USA

f) Department of Materials Science and Engineering, Massachusetts Institute of Technology, Cambridge, Massachusetts 02139, USA

g) National Synchrotron Light Source II, Brookhaven National Laboratory, Upton, NY 11973, USA

h) Institute of Scientific and Industrial Research, Osaka University, Osaka, 567-0047, Japan

i) Department of Physics and Astronomy, University of Georgia, Athens, Georgia 30602, USA

j) Davidson School of Chemical Engineering, Purdue University, West Lafayette, Indiana 47907, USA

k) Center for Nanoscale Materials, Argonne National Laboratory, Argonne, Illinois 60439, USA

l) Department of Nuclear Science and Engineering, Massachusetts Institute of Technology, Cambridge, Massachusetts 02139, USA

In this particular work, I, Daw Gen Lim, am solely in charge of the various electrochemical lithium insertion and stability studies of the as-fabricated thin-films. The thin-films were then sent for various characterizations to enable an inform decision for the designs and feasibility studies of the thin-film Li-ion battery. Y.S. and S.R. conceived the ion doping process and coordinated the project. Y.S., Z.Z., A.N.H, and T.H fabricated the thin films. B.N., M.C., and S.K.R.S.S. performed the ab initio molecular dynamics simulations and the nudged elastic band calculations for computing activation barriers. M.K. and K.M.R. performed first principles DFT calculations. Y.S., Z.Z., Y.D., and H.Z. performed X-ray diffraction and X-ray reflectivity measurements. Y.S., C.S., H.Z., R.K., and Q. L., performed the X-ray absorption measurements, Q.L. was supervised by B.Y. and I. W.; A.H. provided technical support as the beam-line scientist. Y. A and S.G. performed the terahertz time-domain nano-spectroscopy. Y.S. performed optical studies. Y.S. and S.R. prepared the draft of the manuscript and all authors discussed the results and commented on the manuscript. Due to the cohesive integration of the findings and the countless discussions contributed by all the authors, the manuscript is best presented at its

present form. Following the as-presented manuscript, an additional feasibility study of LiSmNiO$_3$ as a solid-state electrolyte for Li-ion batteries component is covered in this chapter; this is not delve into in the manuscript.

Abstract

Solid state ion shuttles are of broad interest in electrochemical devices, non-volatile memory, neuromorphic computing and bio-mimicry utilizing synthetic membranes. Traditional design approaches are primarily based on substitutional doping of dissimilar valent cations in a solid lattice, which has inherent limits on dopant concentration and thereby ionic conductivity. Here we demonstrate perovskite nickelates as Li-ion shuttles with simultaneous suppression of electronic transport via Mott transition. Electrochemically lithiated SmNiO$_3$ (Li-SNO) contains a large amount of mobile Li$^+$ located in interstitial sites of the perovskite approaching one dopant ion per unit cell. A significant lattice expansion associated with interstitial doping allows for fast Li$^+$ conduction with reduced activation energy. We further present a generalization of this approach with results on other rare-earth perovskite nickelates as well as dopants such as Na$^+$. The results highlight the potential of quantum materials and emergent physics in design of ion conductors. Further integration of the LiSmNiO$_3$ into a thin-film battery of LiCoO$_2$|LiSmNiO$_3$|Si chemistry also showed promising results with initial charging capacities reaching 1338 mAh g^{-1}.

4.1   Introduction

Solid state ionic shuttles or conductors are of interest in energy storage, voltage-driven ion channels for neuromorphic computing, and various iontronics technologies wherein ionic injection and transport is coupled with electronic band structure modification in complex semiconductors [135, 136]. For the case of lithium-ions, the ideal conductor should have a large concentration of mobile Li$^+$ and optimized migration channels with minimal activation energy for diffusion [137]. To date, Li$^+$ conduc-

tors make up a diverse set of materials [138–142], among which oxide conductors are prominent [143]. For instance, typical oxide-based Li^+ conductor classes include LISICON-like [144], NASICON-like [145], LiPON [146], glass [147], perovskite [148], and garnet [149]. Fundamentally, Li^+ conduction in a perovskite lattice follows the percolation pathway in A-site vacancy and its conductivity is sensitive to the structure and mobile Li^+ concentration [150–152]. As an example, A-site deficient lithium lanthanum titanate ($Li_{3x}La_{2/3-x\square 1/3-2x}TiO_3$ ($0 < x < 0.167$)) with different amounts of Li^+ substitution, has been investigated. The optimal composition corresponds to x=0.11, i.e., $Li_{0.34}La_{0.51}TiO_{2.94}$ (LLTO), which results in room temperature bulk conductivity of 10^{-3} S cm^{-1} and activation energy of 0.4 eV. Efforts have been devoted to further enhance ionic conductivity of LLTO via heteroatom doping, including A-site substitution by Al^{3+} [153] Sr^{2+} [153] Nd^{3+} [154], and oxygen-site substitution by fluorine [155]. However, the general strategy of heteroatom doping still suffers from fundamental limitations on the extent of Li^+ dopants that can be incorporated substitutionally and are mobile at given temperature [156]. Therefore, new approaches to design high performance oxide Li^+ conductors are of great interest.

Here, we report a new class of Li-ion shuttles based on emergent electron localization in rare-earth perovskite nickelates. As a representative system, $SmNiO_3$ (SNO) with perovskite structure (ABO_3) is electronically conducting due to the single electron occupancy of the e$_g$ orbital of Ni^{3+} (e$_g^1$) [157]. Upon electron filling, the Ni in pristine SNO experiences crossover to Ni^{2+} with a highly localized state (e$_g^2$) and colossal suppression of electronic conductivity due to electron-electron Coulomb interaction [158–160]. Instead of cation substitution, the heteroatoms that are electron donors occupy the interstitial sites of host lattice and have weak bonding to coordinated ligands. Recent work has demonstrated the potential of proton-doped correlated nickelate materials as electric field sensors [161]. Besides hydrogen, alkaline or alkaline-earth metals such as Li possessing larger ionic radius, can also be regarded as electron donors, which effectively modulate the material properties [162]. However their controlled doping, impact on lattice, electrochemical transport behavior,

and atomistic migration pathways are as yet unknown and is extremely important to understand given the large difference in ionic radii compared to protons.

We demonstrate a design principle for solid state Li^+ conductors based on perovskite nickelate thin films (Figure 4.1). Pristine SNO with a single itinerant electron in the e_g orbital of Ni shows high electronic conductivity (Figure 4.1a). After lithiation via electrochemical poling (Figure 4.1b), SNO undergoes an electron filling-induced Mott transition to form a strongly correlated insulating system (Figure 4.1c). The doping, electron localization, and reduction of Ni valence (Ni^{3+} to Ni^{2+}) lead to the enlargement of the lattice volume, which elongates the Ni-O bond. The expanded structure allows for a three-dimensional interconnected Li^+ diffusion tunnel. Further, unlike conventional substitutional doping that has structural modulation limits on the extent of dopant accommodation, the concentration of mobile Li^+ in SNO reaches a much higher level, due to the large density of interstitial sites. The interstitial Li^+ is weakly bonded with oxygen ions, and exhibits fast conduction behavior across the expanded diffusion bottlenecks. We then present evidence for generalizing the electron doping principle with other members of the rare-earth nickelate family.
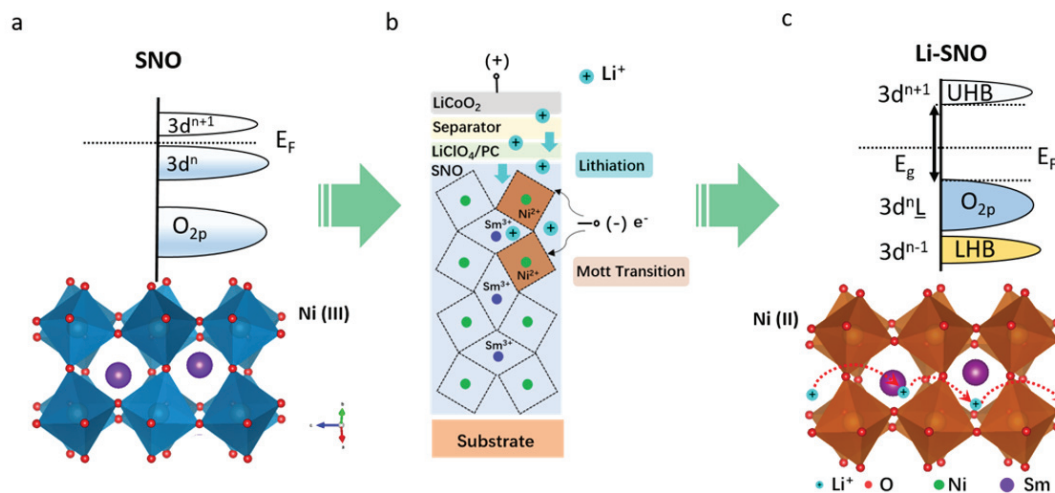
Fig. 4.1.: Lithiated strongly correlated nickelate as ionic conductor a) Electronic configuration of pristine $SmNiO_3$ (SNO). The SNO shows ABO_3 perovskite structure with electron itinerant configuration in e_g orbital of Ni (III). b) A self-designed electrochemical cell for lithiation of SNO. c) Electronic configuration of lithiated SNO (Li-SNO). The electron filling leads to large on-site coulombic interaction U, suppressing the electronic conduction pathway. Large amount of Li^+ occupy into interstitial site of unit cell. The electron localization induced perovskite lattice expansion facilitates unique Li^+ interstitial transport, which enables Li-SNO as potential lithium-ion conductor. Figure prepared by Y.S.

4.2 Experimental

4.2.1 Growth of $SmNiO_3$ thin films

$SmNiO_3$ (SNO) thin films of various thickness $(80 - 200\,nm)$ were grown on $LaAlO_3$ (LAO) substrate using magnetron sputtering combined with post-annealing in high pressure high purity oxygen atmosphere. The deposition condition is 40/10 sccm Ar/O_2 mixture at total pressure of 5 mTorr from two metallic Ni (DC) and Sm (RF) targets (Fig. 4.2a). The stoichiometry of Sm/Ni was confirmed by energy-dispersive X-ray spectroscopy (EDS) equipped with field emission scanning electron microscopy (FE-SEM). The as-deposited samples were annealed in a high-pressure vessel under 1,500 psi of pure O_2 (99.99%) at 500 °C for 24 h in a tube furnace. Film thickness

is ~100 nm prepared for the characterization studies. (Fig. 4.2b–d). Experiments conducted by Y.S. and Z.Z.

4.2.2   Growth of EuNiO$_3$ and NdNiO$_3$

NdNiO$_3$ (NNO) and EuNiO$_3$ (ENO) films with 50 nm thickness were deposited on LaAlO$_3$ (LAO) and NdGaO$_3$ (NGO) substrates from the sintered NNO and ENO ceramic targets, respectively by pulsed laser deposition (ArF excimer, λ=193 nm) with the laser fluence of ~1 J cm^{-2} and the frequency of 3 Hz. Film growth rate was about 0.4 nm/min. The film thickness is ~100 nm. The base pressure in the PLD chamber was less than 1×10^{-6} Pa, the growth temperature was room temperature (~300 K), and the oxygen pressure was set to 30 Pa. The as-deposited samples were then transferred to a home-built high pressure vessel system. The vessel was then inserted into a tube furnace and ramped to 500 °C for 24 h with 1,500 psi pure O^2. Experiments conducted by A.N.H, and T.H.

4.2.3   Lithium Doping Process in SmNiO$_3$

1 M of LiClO$_4$ (Sigma Aldrich) is dissolved in polyethylene carbonate (PC) in an argon filled glovebox with oxygen and moisture levels at <0.5 ppm. A drop of 1M LiClO$_4$ | PC was dispersed on SNO | LAO thin film. A commercial LiCoO$_2$ supported on current collector Al foil was used as lithium source for lithiation. As separator, a piece of polymer membrane (Celgard 2500) is placed underneath the LiCoO$_2$ | Al foil avoiding the direct contact to SNO | LAO thin film. A positive bias is applied to the LiCoO$_2$ | Al foil and thin film serves as the ground electrode for lithiation process. Experiments conducted by Y.S. and D.L.
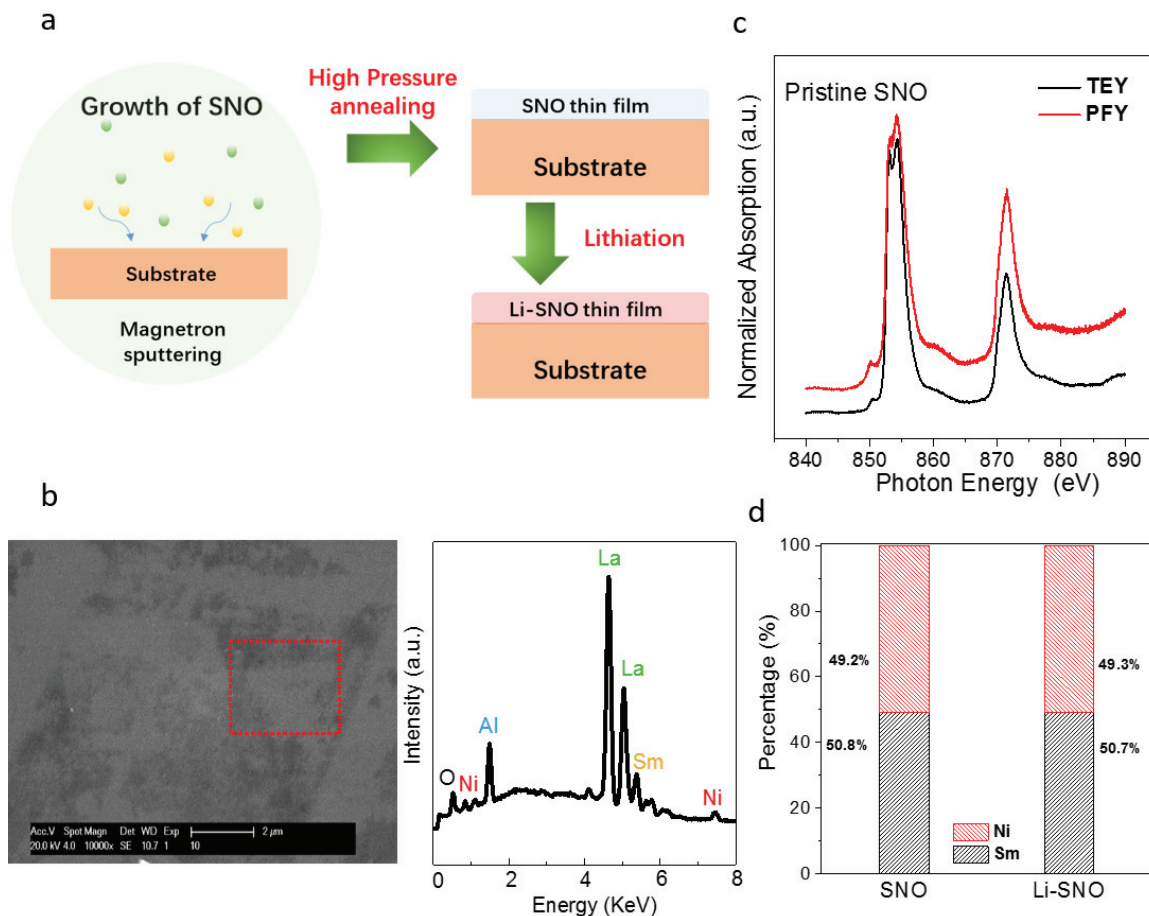
Fig. 4.2.: Schematic of film growth protocol and properties. a) Schematic of growth of $SmNiO_3$ (SNO) thin film. The SNO was deposited by magnetron sputtering and the perovskite phase forms after high pressure annealing process. b) SEM image of pristine SNO/LAO and EDX spectra of selected area of pristine SNO. c) XAS of Ni $L_{2,3}$-edge on SNO thin films. Ni $L_{2,3}$-edge XAS collected in both total-electron-yield (TEY) and partial-fluorescence-yield (PFY). The probing depth is less than 10 nm for TEY and ∼0.1 μm for PFY. A sharp peak at ∼853 eV and a broader peak at ∼855 eV in Ni L_3-edge on both modes are detected. Almost no difference in Ni oxidation states between the surface and the bulk of the thin films could be observed, indicating the homogeneity of the pristine film. d) The cation atomic ratio in the sample upon lithiation by EDX. The lithiation shows negligible influence on the atomic ratio of the cations. Figure 4.2b is prepared by Y.S. Figure 4.2c and d is prepared by Y.S. and Q.L. with supervision from B.Y., I. W., and A.H.

4.2.4 Conductivity Measurements

The as-annealed and lithiated thin films were first cleaned with toluene/ acetone/ isopropanol solutions and dried with argon gas. The electrical conductivity measurements of thin films were performed using a Keithley 2635A in laboratory air environment. The in-plane ionic conductivity of thin film was carried out using AC electrochemical impedance spectroscopy (EIS) at frequencies ranging from 1 MHz to 1 Hz on a Solartron 1260/1287 instrument. As blocking electrodes, an array of platinum bars were deposited onto the films using a metal shadow mask in CHA e-beam evaporator instrument. The distance between two electrodes (L) is much larger than the thickness (H) of thin film to prevent the current constriction effect [163]. A represents the conducting area. The ionic conductivity (S) of thin film can be calculated based on:

$$S = \frac{1}{R} \times \frac{L}{A} \tag{4.1}$$

The R value can be obtained via fitting the EIS curve with an equivalent circuit model. Experiment was conducted by Y.S. and D.L.

4.2.5 Electrochemical Test for Film Cyclability

A closed sandwich half-cell structure consisting of Li | 1M LiPF$_6$ in EC: DEC (1:1) (Sigma Aldrich) — Polymer membrane (Celgard 2500) | Li-SNO (200 nm) | Pt | LAO where bar-shaped (2 mm×10 mm) platinum electrode (100 nm in thickness) is deposited on LAO using an e-beam instrument (CHA). Commercial Li metal disc served as another electrode. Galvanostatic charge discharge is then conducted on the cell with a current density of 5 μA cm^{-2} and a cut off voltage from 0.5 V to 4.2 V for a total cycle of 50 cycles. All tests were performed in an argon filled glovebox with oxygen and moisture levels at <0.5 ppm. Experiments conducted by D.L.

4.2.6 X-ray Photoelectron Spectroscopy

The X-ray photoelectron spectroscopy (XPS) characterization was conducted on a Kratos X-ray Photoelectron Spectrometer equipped with non-monochromatic dual anode X-ray gun with Al Kα (1486.6 eV). The spectra is calibrated with C$_{1s}$ peak at 286.4 eV. Experiment conducted by Y.S.

4.2.7 Terahertz Time-Domain Nano-Spectroscopy (THz-TDNS)

THz-TDNS was employed to assess the change in carrier density that accompanies the Mott transition of SNO. The THz-TDNS is based on scattering-type scanning near-field microscope (s-SNOM) coupled with 1550 nm fiber laser and InGaAs THz emitter and detector. Experiments conducted by Y. A and S.G.

4.2.8 Surface Morphology Measurements

The scanning electron microscopy (SEM) images were collected on FEI XL40 field emission scan electron microscopy (FE-SEM) equipped with Energy-dispersive X-ray spectroscopy (EDS) detector. Experiments conducted by Y.S.

4.2.9 Synchrotron X-Ray Measurements

Synchrotron X-ray reflection (XRR) and X-ray diffraction (XRD) of the SNO samples were conducted at an insertion device beam-line, using X-ray energy of 20 keV at sector of 12ID-D and 33-ID-C at the Advanced Photon Source in Argonne National Laboratory, USA. Experiments conducted by Y.S., Z.Z., Y.D. and H.Z.

4.2.10 X-ray Absorption Spectroscopy

The Ni K-edge X-ray spectra (XAS) were performed using linear polarized X-rays at the undulator beamline 20-ID-C of the Advanced Photon Source (APS), Argonne

National Laboratory. The Si (111) monochromator with resolution $\delta E/E = 1.3 \times 10^{-4}$ was used. The spectra were collected in fluorescence mode using a 12-element Ge solid-state detector. Ni metal foil placed to intercept a scattered beam was used as an online check of the monochromator energy calibration. Experiments conducted by Y.S., H.Z., C.S., H.Z., and R.K.

Ni $L_{2,3}$-edge and O K-edge X-ray absorption spectra (XAS) were collected by using both total electron yield (TEY) through drain current measurements and partial fluorescence yield (PFY) modes at the CSX-2 (23-ID-2) beam-line of National Synchrotron Light Source II (NSLS-II), Brookhaven National Laboratory. PFY spectra were collected using a Vortex silicon drift detector. All the XAS measurements were performed at room temperature in an ultra-high-vacuum chamber (base pressure $\sim 10^{-9}$ Torr). A more detailed description of the beam-line and end-station can be found elsewhere [164]. All the hard X-ray absorption spectra were analyzed by using the Athena and Artemis programs [165, 166]. Experiments conducted by Q.L. with supervision from B.Y. I. W. and A.H., whom provided technical support as the beam-line scientist.

4.2.11 *Ab initio* Molecular Dynamics Simulation of Lithium Diffusion

Ab initio molecular dynamics (AIMD) simulations are performed in the framework of DFT+U within the generalized gradient approximation (GGA) using the projector-augmented wave formalism as implemented in Vienna *Ab initio* Simulation Package (VASP) [167, 168]. We treat the exchange correlation using Perdew-Burke-Ernzerhof (PBE) functional [169], with the pseudopotentials: Sm_3 (valence: $5s^2 5p^6 6s^2 4f^1$), Ni_{pv} (valence: $3p^6 4s^2 3d^8$) and O (valence $2s^2 2p^4$) supplied by VASP, and rotationally invariant form of DFT+U Hubbard correction [170], with U = 4.6 eV, and J = 0.6 eV. The computational supercell consists of 4 unit cells ($2 \times 2 \times 1$ repetitions of the unit cell; 80 atoms) of monoclinic SNO with space group $P2_{1/n}$. Periodic boundary conditions are employed along all the directions. The plane wave energy cut off is set at 520

eV and the Brillouin zone is sampled at the Γ-point alone. First, we thermalize the SNO supercell at various temperatures ranging from 300 K–2500 K, and zero pressure using AIMD simulations in the isobaric-isothermal ensemble (NPT) for 10 ps with a timestep of 0.5 fs. In these simulations, the atomic positions, cell volume, and the cell shape are all allowed to vary via the Parrinello-Rahman scheme [171]; constant temperature conditions are maintained using a Langevin thermostat [172]. Next, we insert a Li into the thermalized SNO lattice (at a given temperature) such that it is tetrahedrally coordinated with four arbitrarily chosen oxygen atoms (each Li-O separation is $\sim$2.1 Å). We monitor the migration of Li in the SNO lattice using AIMD simulations at constant volume (and cell shape) at various temperatures (i.e., using NVT ensemble). In each of these simulations, the constant temperature conditions are maintained (at a desired temperature value) using Nosé-Hoover thermostat [172] as implemented in VASP. To compute the barriers associated with Li migration in SNO lattice, we performed climbing image nudged elastic band (CI-NEB) [173, 174] calculations for various representative pathways. All CI-NEB calculations are performed on a $2\times2\times1$ supercell of monoclinic SNO and at the same level of theory as the AIMD simulations. Simulations conducted by B.N., M.C., and S.K.R.S.S.

4.2.12 First Principles Electronic Structure Calculations

First principle calculations were carried out within the density functional theory (DFT)$+U$ approximation with the Vienna *Ab-initio* Simulation Package (VASP) code [167, 168] using the projector augmented plane-wave (PAW) method of DFT [175] and the supplied pseudopotentials: Sm$_3$ (valence: $5s^25p^66s^24f^1$), Ni$_{pv}$ (valence: $3p^64s^23d^8$), O (valence $2s^22p^4$), and Li$_{sv}$ (valence: $1s^22s^1$).To treat the exchange and correlation, the Perdew-Burke-Ernzerhof (PBE) functional was used within the generalized gradient approximation (GGA) [169] and the rotationally invariant form of DFT$+U$ of Liechtenstein et al. [170] with U = 4.6 eV and J = 0.6 eV. For structural determination of pristine SNO, we started with the *Materials Project* structure added

a small monoclinic distortion ($\beta \approx 90.75°$) and allowed the cell and ionic positions to relax until the forces were less than 0.005 eV/Å on each ion. All calculations were carried out with the tetrahedral method with Blöchl corrections [176], a $6\times6\times4$ Monkhorst-Pack k-point mesh for the $\sqrt{2}\times\sqrt{2}\times2$ supercell, and a plane-wave energy cutoff of 520 eV. When simulating SNO-Li, neutral lithium atoms were added. We began with one added lithium and found the low energy structure allowing all internal coordinates to relax as well as the lattice in the (110) direction. Place lithium atoms at similar positions in the $\sqrt{2}\times\sqrt{2}\times2$ supercell (with 4 Ni), we calculated the electron structure of SNO-Li with lithium concentrations of 1, 2, 3 or 4 lithium to the monoclinic $\sqrt{2}\times\sqrt{2}\times2$ supercell with a G-type magnetic ordering, resulting in an electron doping concentration of $^1/_4$, $^1/_2$, $^3/_4$, 1 e$^-$/SNO, respectively. In each case, we allowed the internal ionic positions to relax as well as the lattice in the (110) direction, using the same force tolerance as before. Simulation conducted by M.K. and K.M.R.

4.2.13 Solid-State Thin-film Lithium-ion Battery Testing

The solid state cell with a sandwich structure consisting of Au | Si | Li-SNO (200 nm) | LiCoO$_2$ (100 nm) are deposited on NbSrTiO$_3$. The LiCoO$_2$ and Li-SNO were deposited using magnetron sputtering (see 4.2.1, and 4.2.3). Si and Au dots (2 μm diameter and 100 nm in thickness) were deposited using an e-beam instrument (CHA). Galvanostatic charge discharge is then conducted on the cell using a Versastat (Princeton Applied Research) with a current density of 0.159 A cm^{-2} and a cut off voltage from 2.5 V to 4V for a total cycle of 50 cycles. The cell measurements were collected in laboratory air environment. Experiment conducted by D.L.

4.3 Results and Discussion

4.3.1 Perovskite Rare Earth Nickelates and its Interaction with Lithium/ Sodium-Ion

Suppression of electronic transport in SNO upon lithiation can be seen in the evolution of film resistivity (Figure 4.3a). The pristine SNO shows low resistivity of around 0.6 mΩ cm and a thermal insulator-metal transition (MIT) point at $\sim$140 °C indicating good film quality. Lithiation for one minute significantly enhances the film resistivity by three orders of magnitude to $\sim$10^3 mΩ cm, along with a visual color change.
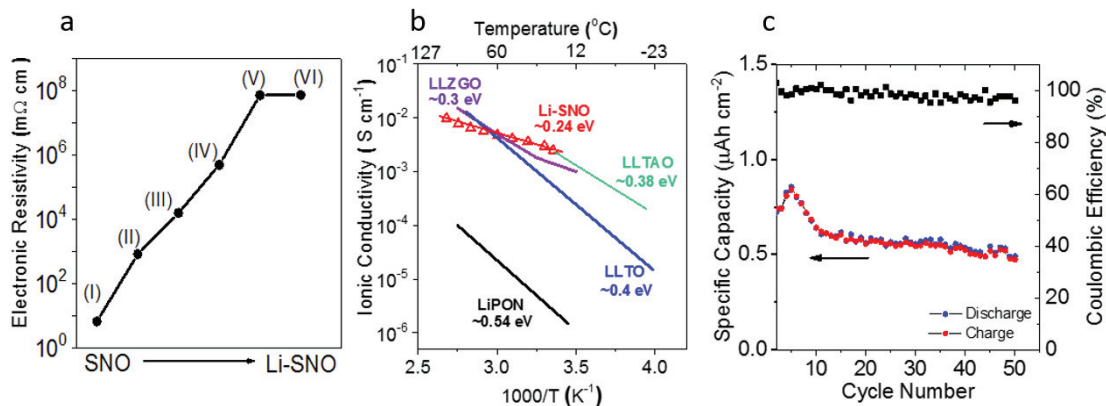
Fig. 4.3.: a) Lithiation induced resistivity evolution of SNO as the function of lithiation time ((I) to (VI) for 0 min, 1 min, 5 min, 30 min, 2 hours and 24 hours, respectively). The Li-SNO becomes transparent and electronically insulating upon 2 hour lithiation. b) The Arrhenius ionic conductivity plots of Li-SNO and other representative conductors are shown in inset. c) Cycling performance of the charge discharge process of Li-SNO half-cell. Figure prepared by Y.S. and D.L.

As lithiation proceeds, the film becomes much more transparent and the resistivity continues to increase to $\sim$10^8 mΩ cm and then nearly saturates, indicating significant suppression of electron flow (denoted as Li-SNO). This massive electronic conduction cut-off originates from the filling-controlled Mott transition. Direct real-space nano-

imaging at terahertz frequencies also highlights this carrier suppression effect (Figure 4.4).
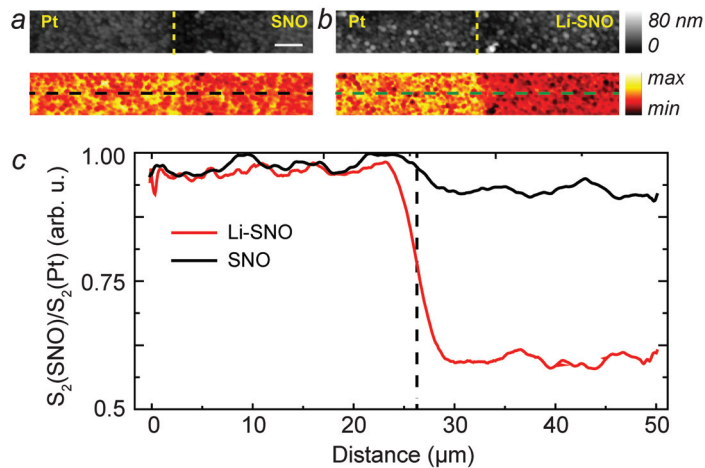
Fig. 4.4.: Terahertz time-domain nano-spectroscopy of SNO film. a-c) Near-field broadband THz (0.6–1.6 THz) time-domain nano-imaging of SNO films before and after Li doping. In both the Li-doped and undoped samples, the topography images show the reference metal Pt surface (20 nm in height) on the left and SNO film on the right with the dashed yellow lines showing the boundary between them. In pristine SNO, the second harmonic amplitude image (s_2) shows similar THz scattering contrast between the undoped SNO surface and the reference Pt surface. On the other hand, the image contrast between the Li-SNO with respect to the Pt surface is noticeable. The normalized line profiles ($s_2(SNO)/s_2(Pt)$) displays a small relative amplitude (~0.95) of SNO, whereas amplitude contrast in Li-SNO drops to ~0.60 (dashed black line depicts the Pt-SNO boundary). These relative scattering amplitude contrasts can be explained by the Drude response of free carriers to the time-dependent electric field of the THz beam where higher carrier concentrations lead to a high scattering by the probe tip with nearly flat spectrum [177]. As such, the nearly unity normalized amplitude in pristine SNO implies presence of free carriers in SNO indicating metallic behavior of at THz frequencies. The striking drop in the normalized amplitude in the case of the Li-SNO implies the strong suppression of free carriers arising from the Mott transition. Scale bar is 5 μm. Figure prepared by Y. A and S.G.

Figure 4.3b shows the Arrhenius conductivity plots of Li-SNO and other representative oxide Li$^+$ conductors. Li-SNO has room temperature ionic conductivity of 3.1×10^{-3} S cm^{-1} with low activation barrier of ~0.24 eV, comparable to even organic liquid systems. The cycling performance of the lithiation-delithiation process (Figure

4.3c and Figure 4.5a) demonstrates an average coulombic efficiency of 96.8 %. Upon cycling, the Li-SNO maintained transparency throughout the experiments, indicating that under galvanostatic lithiation, of up to 4.2 V, the material remains stable. These studies demonstrate the shuttling of Li ions across the perovskite lattice under electric fields.
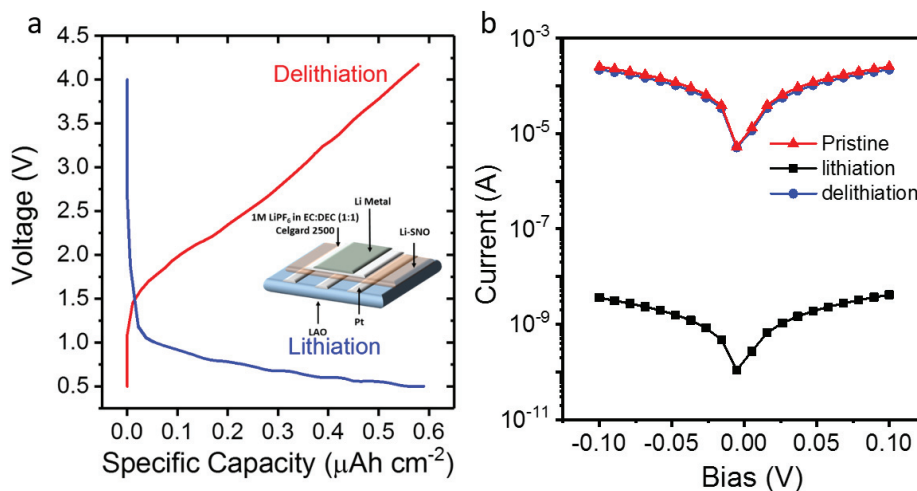
Fig. 4.5.: Lithiation and delithiation behavior for Li-SNO. a) Representative lithiation and delithiation cycle on SNO by galvanostatic measurement. The electrochemical cyclability of Li-SNO was evaluated in a Li-metal cell, with Li metal as working electrode and Li-SNO as counter electrode (schematic shown in inset figure). The charge-discharge curve illustrates the full lithiation and delithiation behavior of the Li-SNO material. b) Representative lithiation and delithiation cycle on SNO by potentiostatic measurement. 30 min lithiation (3.0 V) significantly enhanced the film resistivity by more than 4 orders of magnitude. Successive delithiation (-3.0 V) for 3 hours could successfully modulate the resistivity of film back to its original state, indicating full delithiation. Figure prepared by Y.S. and D.L.

Collective phenomena due to strong electron-electron correlations leads to these striking observations in the perovskite nickelate. In Li-SNO, the transport bottleneck from the flexible tilting of the NiO_6 octahedra controls the unique interstitial Li^+ diffusion across adjacent hopping sites. The larger Ni^{2+} radius combined with the electron localization effect synergistically increase the Ni-O bond length and result

in volume expansion of the perovskite unit cell, which significantly reduces the Li$^+$ transport barrier.

To show that lithiation does indeed lead to reduction of the Ni sites, we measured XPS spectra of Ni (2p$_{3/2}$) peak and Li (1s) peak (Figure 4.6). The Ni peak shifts to lower binding energy after lithiation, demonstrating the increase in the fraction of Ni (II) and decrease in the fraction of Ni (III) in Li-SNO. As the lithiation proceeded, the Li$_{1s}$ peak intensity gradually increased, indicating increasing content of Li$^+$ (Li$^+$: Ni $\sim$0.86 for fully doped Li-SNO).
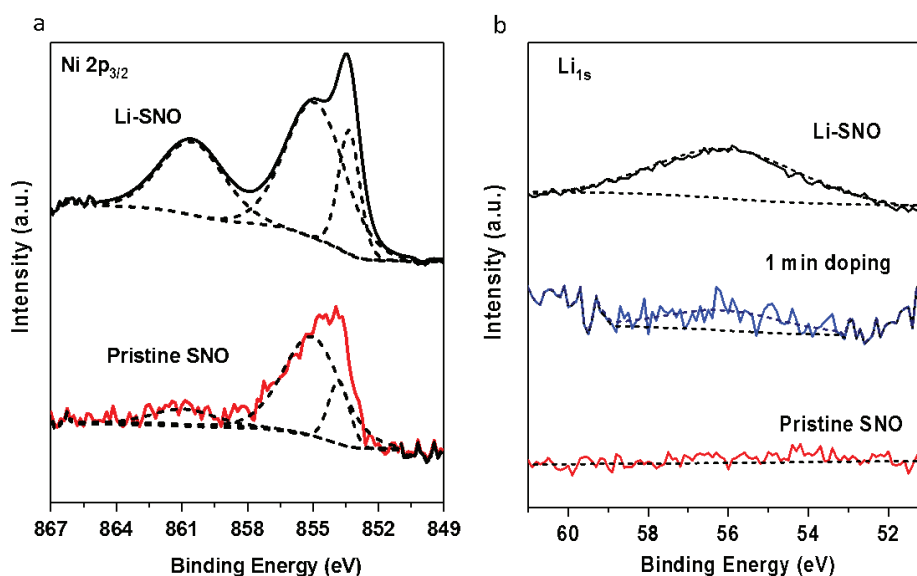
Fig. 4.6.: Electronic configuration evolution upon lithium intercalation. a-b) X-ray photoelectron spectroscopy (XPS) characterization of (a) Ni 2p$_{3/2}$ and (b) Li 1s. Due to multiplet splitting, the valence state of Ni cannot be explained by a single binding energy peak. However, the major Ni (2p$_{3/2}$) peaks shift to lower binding energy regime after lithiation, qualitatively suggesting the emergence of Ni^{2+}. The binding energy peak at 56 eV can be ascribed to Li$_{1s}$. The concentration Li$^+$ of in Li-SNO is estimated to be (Li/SNO=0.86/1). The XPS Atomic Sensitivity Factors used for calculation are: Li (1s): 0.02; Ni (2p$_{3/2}$): 3.0. Figure prepared by Y.S.

To further illustrate the detailed change in the electronic structure upon lithiation, we characterize the films with X-ray absorption near edge spectroscopy (XANES). In the normalized Ni K-edge XANES (Figure 4.7a), the pre-edge (feature A) points to

the covalence between O_{2p} and Ni_{3d} orbital. The rest of absorption features essentially stem from two different coordination shells, e.g., the first shell (in feature B,D,E) is formed by octahedral oxygen coordination while the second shell (feature C and C) is due to rare-earth atoms in a pseudocubic coordination [178]. The intensity of feature A (inset of Figure 4.7a) significantly decreased after lithiation, indicating the Ni valence decrease. Ni L_3-edge spectra of SNO also shows drastic changes after lithiation with diminished peak at $\sim$855 eV, stressing the transition of Ni^{3+} to Ni^{2+} (Figure 4.7b) [179].

A detailed comparison of pre-edge area (Ni K-edge) clearly shows that the lithiation process decreases the concentration of ligand hole ($3d^8$ L in the ground state of Ni, where L denotes a hole state generated in ligand p orbital) by 40% [178]. Further study on the O K-edge spectra (Figure 4.7c) indicates a reduced O-projected density of unoccupied states due to lithiation induced electron filling, suggesting the formation of Ni^{2+}.

The rest of the holes within O^{2-} could bond with Li^+ and facilitate its transport. The first derivative plot (Figure 4.8a-b) of the Ni K-edge XANES presents a shift of the pre-edge and absorption edge toward lower energy by 1.65 eV for the 2 hour-lithiated sample. Previous studies have shown a slope shift of 1–2 eV/electron charge for Ni-containing oxides with octahedral coordination [180]. An effective change in valence of -1 for the Ni ions is seen here. Such lithiation induced phase transition phenomena can propagate through the film thickness (Figure 4.9).
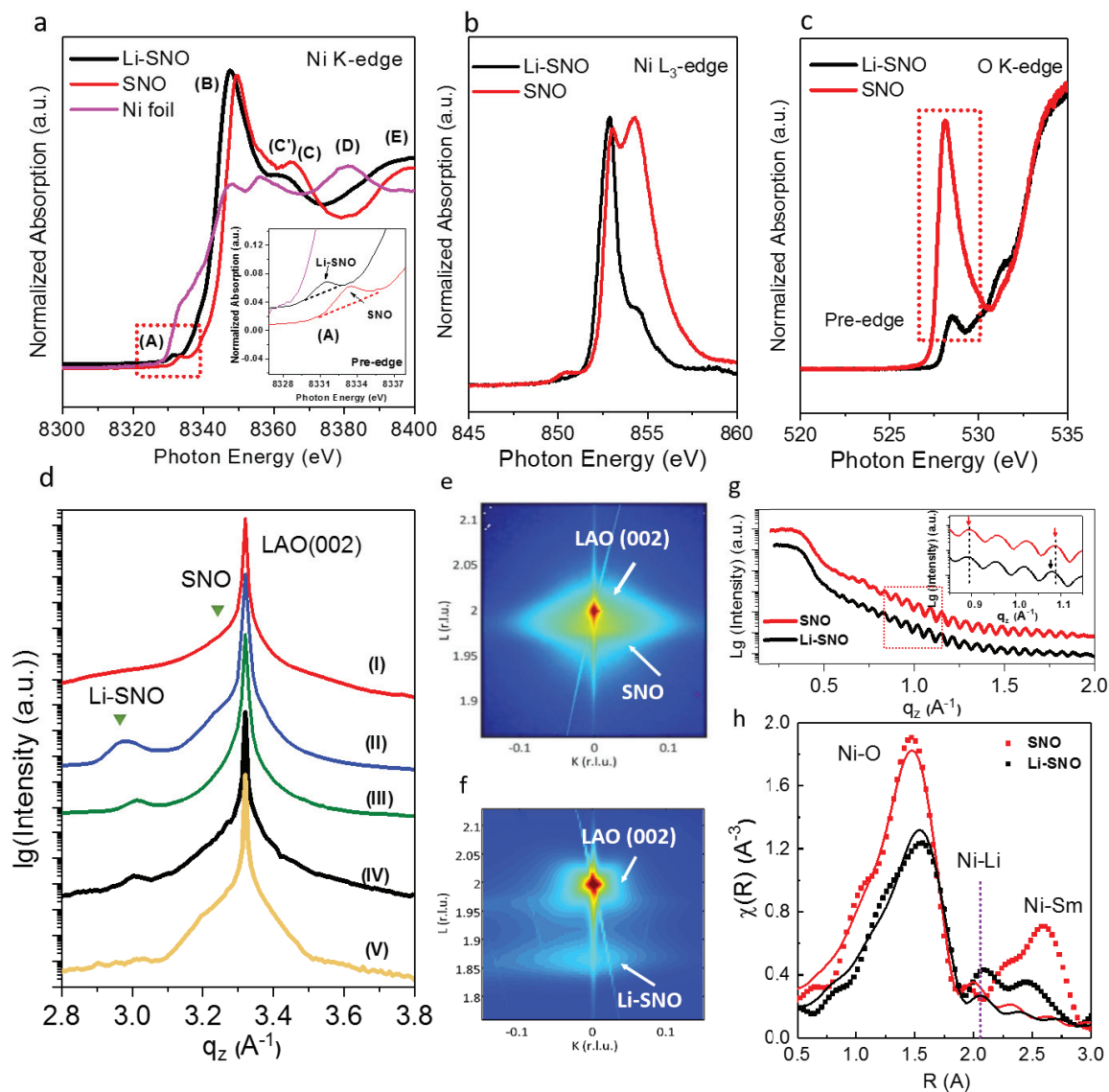
Fig. 4.7.: Electronic and structural configuration of Li-SNO. a) Ex-situ normalized Ni K-edge b) Ni L_3-edge c) O K-edge of X-ray absorption near-edge spectroscopy (XANES) characterization of pristine SNO and Li-SNO. As a reference, the spectrum of Ni foil was used for energy calibration. d) In-situ synchrotron x-ray diffraction (XRD) pattern of SNO upon charge-discharge cycles. (I) Pristine SNO, (II) Li-SNO, (III) 1 cycle, (IV) 20 cycles, and (V) 50 cycles. e-f) 2-D Reciprocal space mapping (RSM) around the pseudocubic (002) reflection of (e) pristine SNO and (f) Li-SNO. g) Synchrotron X-ray reflectivity (XRR) pattern comparison of SNO and Li-SNO. h) Fourier transform of the Ni K-edge EXAFS (dots) and the fitting (lines) of SNO and Li-SNO. Figure 4.7 a, d, e, f, g, and h prepared by Y.S., Z.Z., Y.D., H.Z., C.S., and R.K. Figure 4.7 b and c prepared by Y.S. and Q.L.
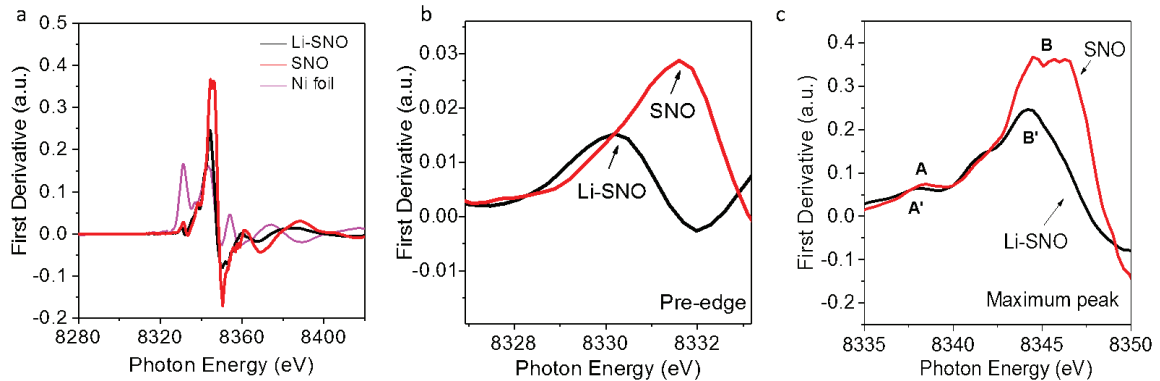
Fig. 4.8.: First derivative XANES of Ni K-edge of pristine SNO and Li-SNO. a) First derivative of normalized XANES of SNO and Li-SNO. Nickel metal is used as reference. b) Zoom in of pre-edge of first derivative of the normalized XANES spectra. The decrease of pre-edge intensity suggests that injected electron fills the unoccupied oxygen ligand holes. c) Zoom in of the maximum peak of first derivative of the normalized XANES spectra. The energy separation between the pre-edge excitonic feature and the first strong absorption maximum is an inverse function of the Ni-O bond length. After lithiation, such splitting becomes smaller by 1.1 eV, indicating the increase of Ni-O bond length. Figure prepared by Y.S., C.S., H.Z., and R.K.

The lithiation of SNO initially leads to the interstitial intercalation of Li^+ and electron localization, which further results in structural distortion. In order to obtain quantitative information on the lattice parameter evolution of SNO upon lithiation, synchrotron X-ray diffraction (XRD) was performed and the corresponding pattern is shown in Figure 4.7d. Pristine SNO has a pseudocubic lattice constant of 3.799 Å which is quite close to that of the LAO substrate (3.790 Å) [181]. As seen in Curve I of Figure 4.7d, the SNO exhibits a shoulder ((220) peak, orthorhombic notation) located at $q_z=3.29$ Å^{-1} close to LAO (002) peak (pseudocubic notation). Lithiation induces the appearance of peaks at $q_z=2.98$ Å^{-1} corresponding to $\sim$9.1% out-of-plane lattice dilatation (Curve II in Figure 4.7d). 2-D reciprocal space mapping (RSM) around the pseudocubic (002) reflections of pristine SNO and Li-SNO (Figure 4.7e-f) further confirm lattice expansion of $\sim$9% in Li-SNO. The lithiation induced thin film lattice expansion was further seen in synchrotron X-ray reflectivity (XRR) (Figure 4.7g). As compared to the pristine state, a significantly decreased oscillation period of

Li-SNO can be observed, due to the increase of film thickness. This significant lattice expansion due to NiO_6 octahedral distortion can then be correlated to the reduced diffusion activation energy [182].
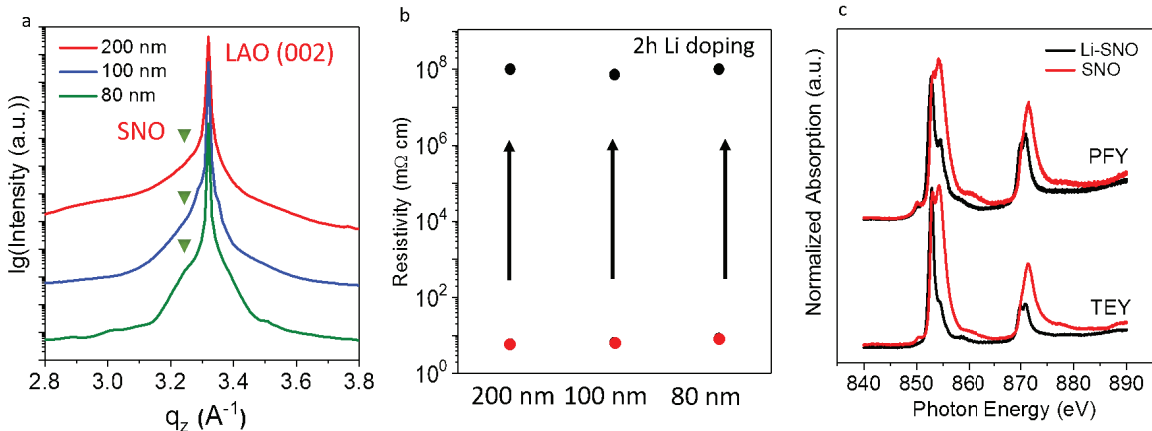
Fig. 4.9.: Film thickness effect on lithiation. a) Synchrotron x-ray diffraction (XRD) patterns of SNO thin films with thickness of 80 nm, 100 nm and 200 nm. All the films exhibit SNO features close to LAO (002) peak. b) Lithiation induced resistance enhancement on SNO with different thicknesses. The samples show increase of resistance up to 7 orders of magnitude after 2 hours lithiation. c) Ni $L_{2,3}$-edge of X-ray absorption spectroscopy on SNO and Li-SNO thin films under PFY and TEY modes. While the TEY mode probes the near-surface region (probing depth less than 10 nm), the PFY mode provides information of the bulk ($\sim$0.1 μm). The similar evolution upon lithiation could be found on both TEY and PFY spectra, indicating the homogeneity of lithiation across the thin film cross section. Figure 4.9 a and b prepared by Y.S., Z.Z., Y.D., and H.Z. Figure 4.9 c prepared by Y.S. and Q.L.

It further can be seen in the first derivative plot of the Ni K-edge XANES spectra (Figure 4.8c) that the energy separation between A and B feature is $\sim$16.45 eV for pristine SNO which is larger than that of Li-SNO ($\sim$15.35 eV). The significant change in energy splitting suggests that lithiation enhances the lattice distortion and increases the Ni-O bond length. The fitted Fourier transformed extended X-ray absorption fine structure (EXAFS) spectra (Figure 4.7h and Figure 4.10) gives a local picture of the Ni coordination shells. The first peak (A) at $\sim$1.5 Åis from the Ni-O coordination shell, and the feature at 2.6 Å stems from the Ni-Sm shells. Lithiation not only

leads to the decrease of the Ni-O peak intensity but also shifts the peak position toward larger radius, which is in part due to the larger Ni(II) ions in SNO [183]. The fitting results demonstrate that the Ni-O bond length expands by 0.08 Å due to the Li doping (from 1.95 Å to 2.03 Å). Noticeably, a distinct feature around 2.2 Å was found in Li-SNO which we ascribed to an additional Ni-Li shell between Ni-O and Ni-Sm, further strengthening our hypothesis that Li^+ occupies interstitial sites. In-situ synchrotron XRD experiments were performed to detect the structural evolution during cycling (Figure 4.7d). The diffraction peak at q_z=2.98 $Å^{-1}$ shifts to 3.03 $Å^{-1}$ (Curve III in Figure 4.7d). Multiple cycles make the SNO thin film disordered (weak Laue fringes between q_z=2.8–3.1 $Å^{-1}$ in curve IV and V in Figure 4.7d); the high electronic resistance of Li-SNO, however, is still maintained.
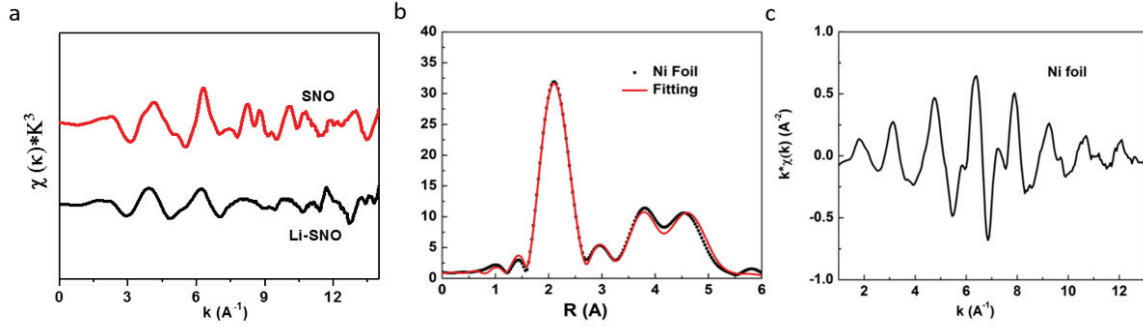
Fig. 4.10.: EXAFS of Ni K-edge of pristine SNO and Li-SNO. a) Ni-K-edge EXAFS for the pristine SNO and Li-SNO. b) Ni EXAFS for the Ni foil. c) Fourier transform of the Ni foil K-edge EXAFS (dots) and the fitting (lines). The data in the k range of 2.5–12 Å^{-1} were used for Fourier transform. The R-range of the fit is 1.1~2.2 Å, and only the Ni-O path is included in the fitting. The fitting parameters for different samples are summarized in Table 4.1. The passive electron reduction factor S_0^2 is 0.853. The ΔE, ΔR and σ^2 values were treated as free parameters for fitting. All the R-factors are much lower than 0.02, indicating the reliability of the fitted results. For pristine SNO, the Fourier transfer amplitude near 1.5 Å corresponds to the Ni-O bond, while the Fourier transfer amplitude near 2.6 Å corresponds to the Ni-Sm bond. After lithiation, the intensity of the Ni-O feature is weakened with shift to the right. CN decreases from 5.56 to 4.52, indicating an increase in structural disorder. A distinct Fourier transfer amplitude appears near 2.2 Å on Li-SNO (the dash vertical line in Figure 4.7h), which is located between the Ni-O distance and the Ni-Sm distance. This implies that an additional shell between the O shell and the Sm shell does exist around the central Ni atom. This additional shell can be reasonably attributed to interstitially distributed Li dopants. Figure prepared by Y.S., H.Z., C.S., H.Z., and R.K.

Table 4.1.: Fitting structural parameters obtained by the FEFFIT code. Table prepared by Y.S., H.Z., C.S., H.Z., and R.K.

Parameter	$R_{\text{Ni-O}}$ (Å)	ΔE	σ^2-O($\times 10^{-4}$ Å^2)	CN	R-factor
SNO	1.95±0.011	-2.43±1.273	57.0±12.38	5.56±0.546	0.009
Li-SNO	2.03±0.018	-2.93±1.818	80.4±27.91	4.52±0.755	0.004

Notes: R, E, σ, CN, and R denote deviation form the theoretical bond length, edge shift, temperature dependent mean squared displacement of the half path length, average coordination number, and fractional misfit, respectively.

Based on first-principles based density functional theory (DFT) calculations, as lithium is added to SNO, its valence electron localizes on a Ni site, thus converting it to a Ni^{2+}. The Li valence electron occupies a previously unoccupied Ni-O state and does not introduce a lithium state near the Fermi energy. In fact, once a Ni site is converted to Ni^{2+} the remaining unoccupied e_g states are pushed away from the occupied e_g states due to electron-electron correlations, leading to a much larger band gap once all of the nickel are converted to Ni^{2+} (Figure 4.11a).
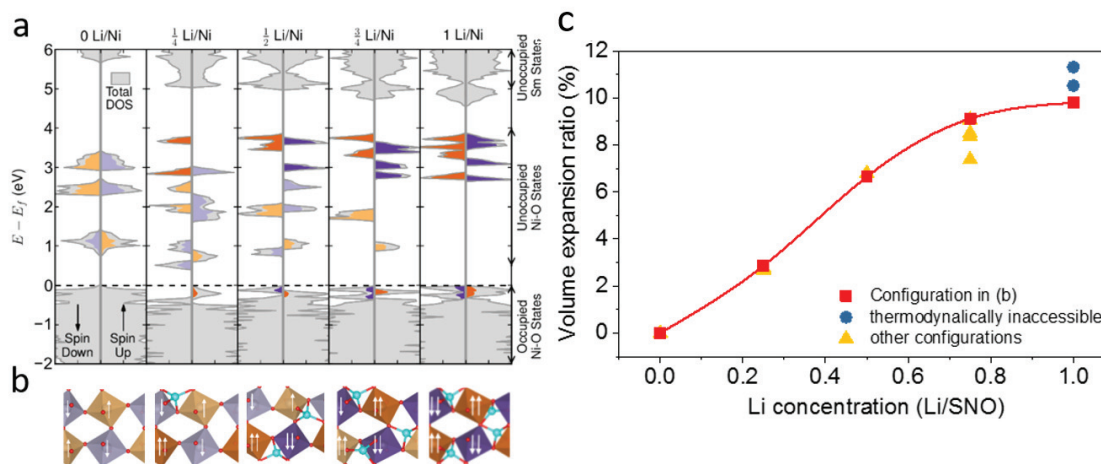
Fig. 4.11.: First principles simulation of Li-SNO and interstitial diffusion. a)Total density of states of SNO with 0–1 intercalated Li/SNO (grey). The projected DOS (PDOS) of the unoccupied Ni e_g states are shown in color. The lighter hues indicate e_g states of Ni^{3+} and the darker hues of Ni^{2+} including the newly occupied e_g states due to the localization of the added electron from the intercalated lithium below the Fermi energy. The character of the localized electrons is primarily oxygen, consistent with the reduction of the O-K pre-edge seen in the XANES characterization. b) $\sqrt{2} \times \sqrt{2} \times 2$ SNO supercells with 0–1 Li/SNO showing the tetrahedral coordination of the Li. The arrows indicate the occupancy of the Ni e_g states and the color of the octahedra correspond to the PDOS above. c) The lattice volume evolution as a function of Li/SNO concentration while allowing the (110) direction to relax. The red points correspond to the geometries shown in (b), the blue points to kinetically inaccessible configurations and the yellow to geometries with different lithium positions occupied (Figure 4.13). Figure prepared by M.K. and K.M.R.

Structural optimization calculations using DFT show that at a concentration of 1:4 Li^+:Ni the lowest-energy intercalated Li^+ ion is tetrahedrally coordinated by four oxygens from adjacent corner-sharing NiO_6 octahedra. These octahedra are canted toward each other with an out-of-phase tilt angle between them such that the LiO_4 tetrahedron is face-sharing with one NiO_6 octahedron and edge-sharing with the other (Figure 4.11b and Figure 4.13d-f). The added Li valence electron causes an increase to the volume of the NiO_6 octahedron that contains a Ni^{2+} ion, which is not necessarily the closest Ni to the intercalated Li^+, as the localized electron need not sit on one of the adjacent NiO_6 octahedra. At a concentration of 1:1 Li^+:Ni, the lowest energy structure has intercalated Li^+ tetrahedronally coordinated in the face-edge sharing configuration described above as well as Li^+ between two octahedra canted toward each other with an in-of-phase tilt angle between them such that the LiO_4 tetrahedron is edge-sharing with both NiO_6 octahedron (Figure 4.13g-i). Informed by the experimental characterization and the molecular dynamics calculations presented below, however, this system seems to be kinetically inaccessible. Restricting our attention to geometries where the Li^+ remains in the face-edge sharing tetrahedra, the calculated overall volume expansion for 1 Li/Ni is $\sim$10%, which is consistent with diffraction data (Figure 4.11c). For the series of geometries shown in Figure 4.11b, the average Ni-O bond length increases 0.07 Å (from 2.002 Å of SNO to 2.074 Å of Li-SNO), the coordination number decreases by around one (6 to 5), and the average Ni-Li bond length is $\sim$2.1 Å, in good agreement with the EXAFS results (Table 4.1). The lattice expansion mechanism associated with donor doping from Li described here is similar to the lattice expansion caused by donor doping by oxygen vacancies in oxides [184]. The larger the extent of localization of the electron on the redox active metal cation, the larger the expansion in the structure [185].
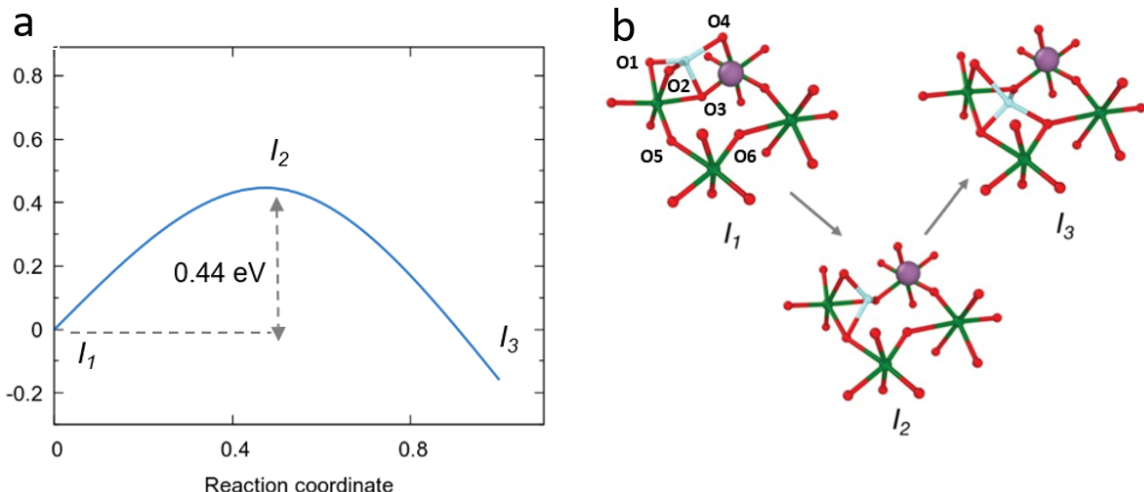
Fig. 4.12.: a-b) Atomic scale pathways and the associated barriers for Li migration in SNO lattice calculated using CI-NEB calculations within the framework of DFT+U. The potential energy along the most preferred pathway is shown for Li migration between two adjacent O-tetrahedral sites, when the neighboring tetrahedral sites are either above/below the ring formed by Ni atoms and the shared O-corners of four adjacent NiO_6 octahedra (as shown in atomic plots). Shown in b), initially the Li atom is tetrahedrally coordinated by 4 O atoms of two adjacent NiO_6 octahedra (as shown by I1), namely O1, O2, O3 and O4. Among these, O1 and O2 belong to one NiO_6 octahedron, O4 belongs to another, while O3 is the shared corner between the two octahedra. The average Li-O bond distance in this initial tetrahedral configuration is $\sim$2 Å; while Li-O5, and Li-O6 separations are $\sim$3.6 Å and $\sim$4.1 Å respectively. The Li-O3 bond rotates about the two NiO_6 octahedra, causing distortion of the O-tetrahedra formed by O1, O2, O3 and O4; note during this rotation, the Li-O3 and Li-O2 bonds remains intact with separation of $\sim$1.8 Å – 2.0 Å, while the other Li-O separations increase gradually. The rotation of Li-O3 causes the Li to come in close proximity to O5 and O6; (I2), the Li-O5 and Li-O6 separation distances reduce to $\sim$2.0 Å and $\sim$2.5 Å respectively. Concurrently, the Li-O1 and Li-O4 bonds break with their separation distances increasing to $\sim$2.8 Å – 3.1 Å. Eventually, Li settles into the tetrahedron formed by O2, O3, O5 and O6 with Li-O bond distances $\sim$1.9 Å –2.1 Å (I3). Figure prepared by B.N., M.C., and S.K.R.S.S.
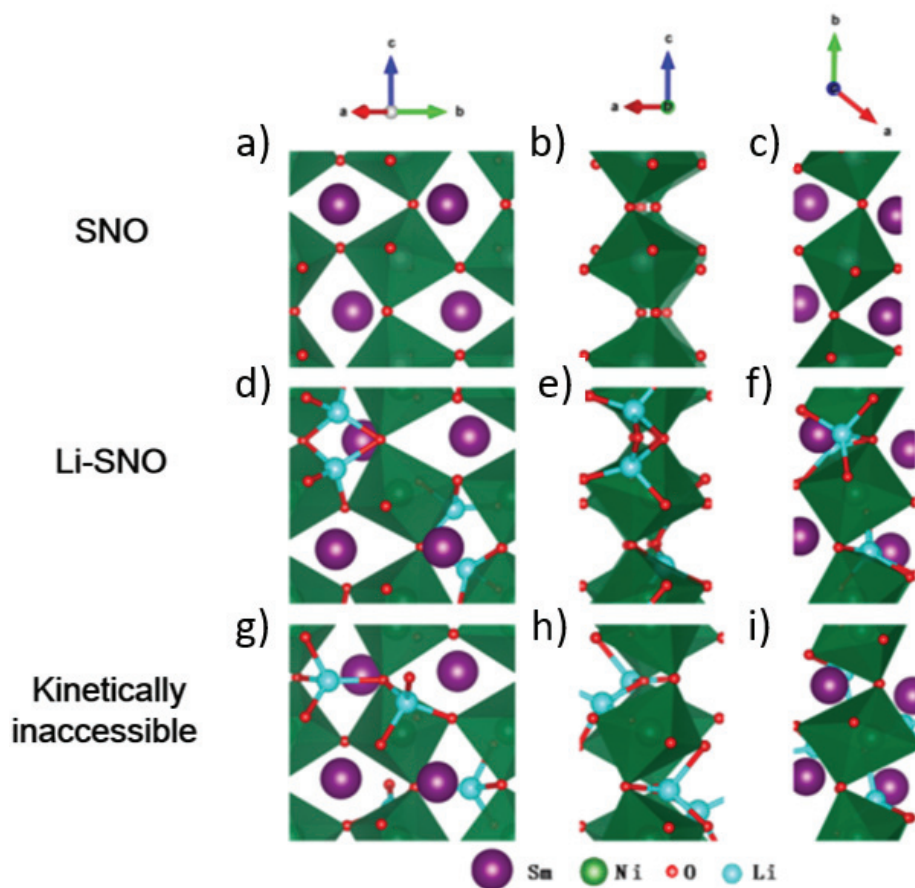
Fig. 4.13.: a-i) Other guesses of Li position and migration pathway of Li in Li-SNO. The structure of SNO (a-c) , Li-SNO (d-f) , and a kinetically inaccessible geometry of Li-SNO (g-i) are shown along the crystallographic axes. Note that a||(110), b||(-100) and c||(001). In panels (b), (e), and (h) the samarium (Sm) have been omitted for clarity.Kinetically inaccessible geometry: even though this is the lowest energy structure, it has Ni-O bond length of 2.95 Å. This value is not supported by the EXAFS data or the AIMD simulations. Moreover, comparing this structure to the structure of SNO and the structure of Li-SNO we see the much longer Ni-O bond when looking along the (001) direction. The fully doped system with the largest volume expansion has Li that are tetrahedrally coordinated in edge-edge configurations and is the system that is lowest in overall energy; however, informed by the AIMD calculations, this system appears to be kinetically inaccessible. Figure prepared by B.N., M.C., and S.K.R.S.S.
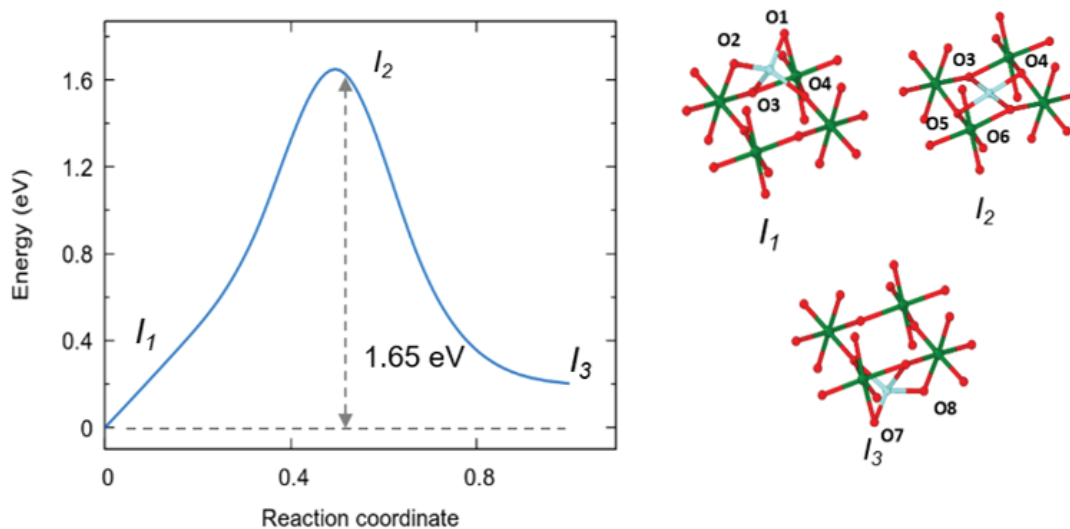
Fig. 4.14.: Another possible migration pathways between two tetrahedral sites that requires the Li atom to cross through the ring formed by the 4 Ni, and 4 shared O corners are associated with a higher energetic barrier. Similar to the pathway shown in Figure 3, initially, Li atom sits in a tetrahedron formed by O1, O2, O3 and O4 atoms (average Li-O $\sim$2.1 Å) (I1). Li-O3 and Li-O4 bonds rotate about the NiO_6 octahedra causing cleavage of Li-O1, and Li-O2 bonds. Consequently, Li forms new bonds with O5 and O6 atoms (Li-O bond length $\sim$1.7–2.1 Å) (I2). This configuration is, however, largely planar and does not have the tetrahedral arrangement preferred by Li. This causes the Li-O5 and Li-O6 to rotate further, thereby breaking the Li-O3 and Li-O4 bonds, and bringing the Li closer to O7 and O8. This continues until a LiO_4 tetrahedron with O5, O6, O7 and O8 atoms form (I3). In this pathway, the motion of Li is also hindered by the presence of Sm atom in the empty space between the four corner-sharing NiO_6 octahedra; this obstruction, along with the necessity of higher number of bond breaking/formation (as compared to pathway in Figure 3) results in the higher energetic barrier. Figure prepared by B.N., M.C., and S.K.R.S.S.

Ab-initio molecular dynamics (AIMD) and DFT calculations were performed to understand Li migration pathways through the SNO lattice and the associated barriers. During a typical AIMD run at a modest temperature of 300 K, we observe frequent Li hopping from one tetrahedral site to a nearby one. Climbing image nudged elastic band (CI-NEB) calculations within the framework of DFT+U for an isolated Li hop in an unstrained SNO lattice reveal an energetic barrier of $\sim$0.44 eV (Figure 4.11d). The optimal diffusion pathway involves migration of Li between two

tetrahedral sites above the ring formed by the four Ni, and four shared O corners. This hopping is facilitated by the rotation of a Li-O bond about two corner-shared NiO_6 octahedra, and consequent distortion of the initial LiO_4 tetrahedron (Figure 4.11e and Figure 4.15). This barrier is further lowered by ~15% (~0.39 eV) when considering an overall volume expansion of 10% as shown in the XRD data. Recent *ab-initio* modeling suggests concerted migration of multiple Li ions can proceed with energy barriers that are much lower than isolated Li hops, owing to strong ion-ion interactions at high Li concentrations [186]. Future studies therefore may focus on exploring the effects of concentration dependence of ion diffusivity coupled with strain.
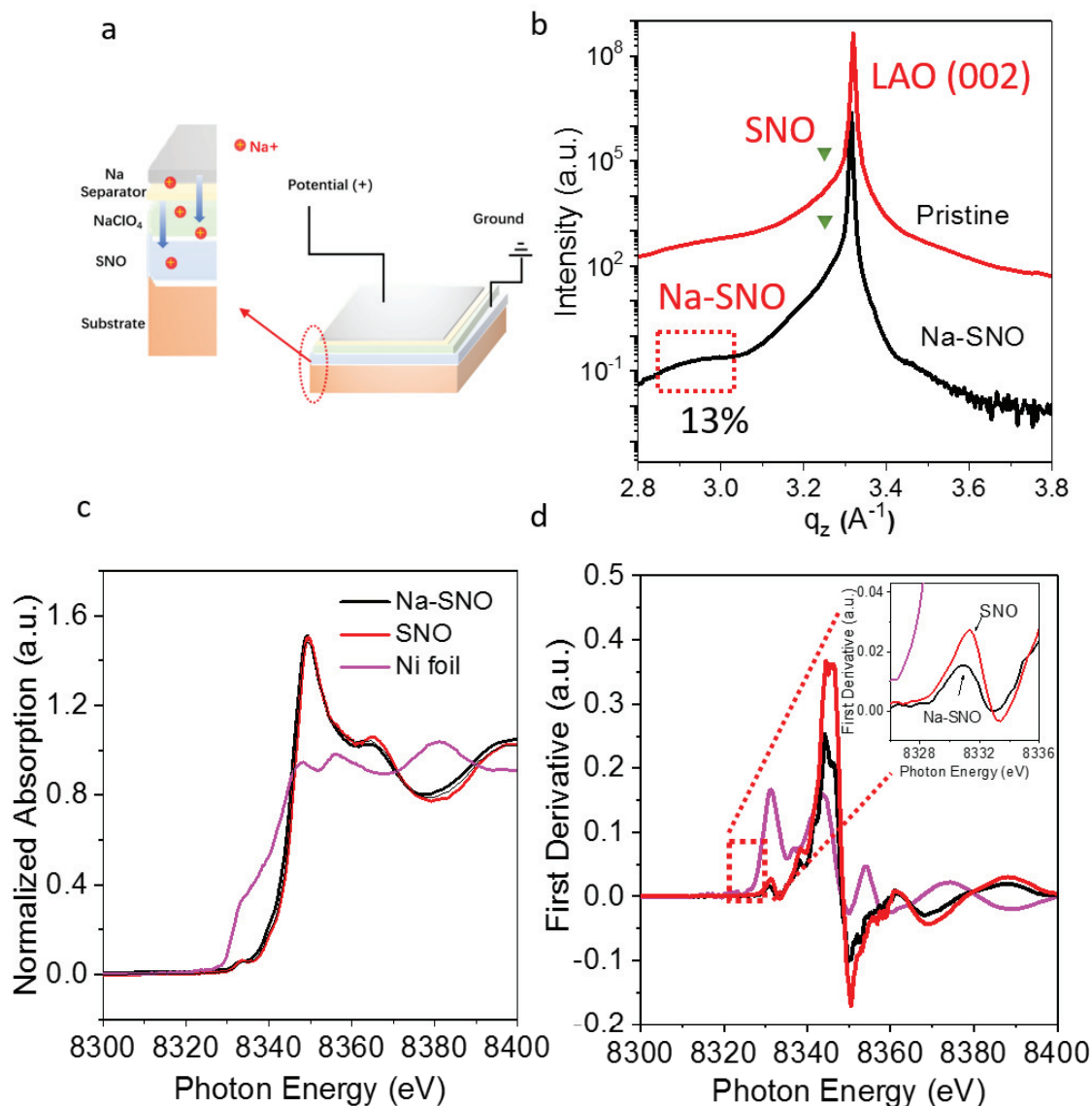
Fig. 4.15.: Sodium (Na) intercalation in SNO a) Na$^+$ intercalation approach. Na$^+$ intercalation into SNO was performed by using similar setup as lithiation apparatus. Sodium (Na) disc and 1M NaClO$_4$ in ethylene carbonate (PC) solution were chosen as Na doping reservoir and electrolyte, respectively. b) Synchrotron x-ray diffraction (XRD) pattern of the SNO after Na injection. Na injection leads to a weak peak located at q$_z$= 2.93 Å^{-1} corresponding to ~13% lattice expansion, which can be ascribed to the larger radius of Na$^+$ compared to Li$^+$. c) *ex-situ* normalized Ni K-edge XANES characterization of pristine SNO after Na injection. A Ni foil was used as a reference. d) The first derivative of the normalized absorption spectrum shown in Figure 4.15 c. The chemical shift was determined as 1 eV, indicating similar electron localization phenomenon as Li-SNO. Figure 4.15 a prepared by Y.S. Figure 4.15 b prepared by Y.S., Z.Z., Y.D., and H.Z. Figure 4.15 c d prepared by Y.S., C.S., H.Z., and R.K
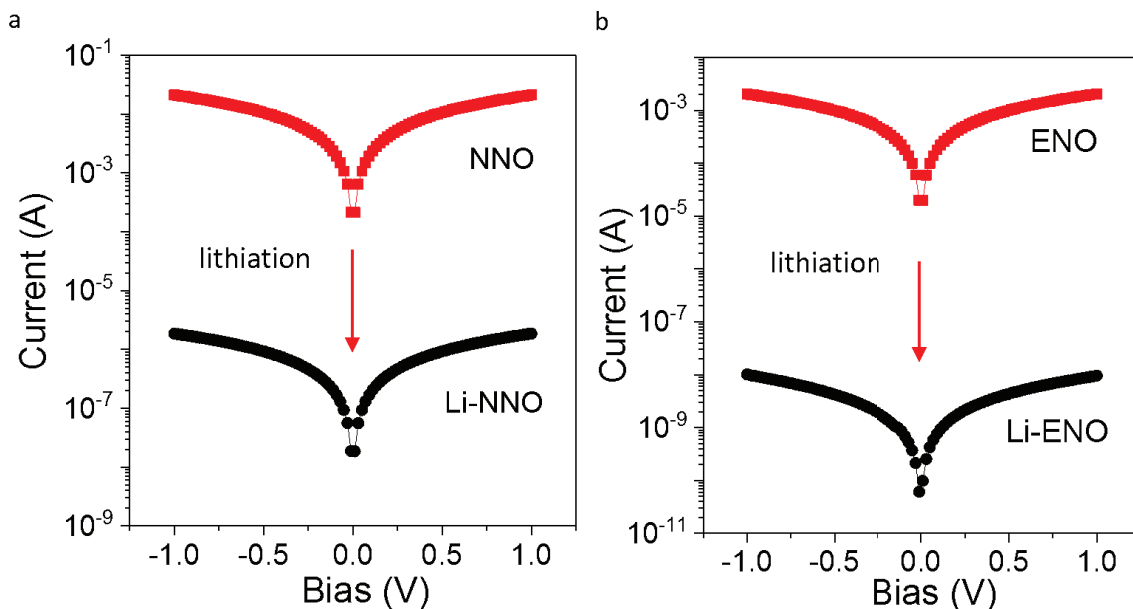
Fig. 4.16.: Li intercalation in $NdNiO_3$ (NNO) and $EuNiO_3$ (ENO) thin films. a) I-V curve of NNO thin films on LAO substrate before and after Li intercalation. Lithiation (at 3 V for 2 hours) modulates the resistance of NNO film by 4 orders of magnitude, indicating the carrier localization. b) I-V Curve of ENO thin films on $NdGaO_3$ substrate before and after Li intercalation. Lithiation (at 3 V for 2 hours) reduces the electronic conductance of ENO film by 6 orders of magnitude, indicating general behavior of the perovskite nickelates to Li doping. Figure prepared by Y.S.

The way the expanded bond lengths support faster Li mobility in this system is in analogy with the larger mobility and reduced migration barriers of oxygen atoms in tensile strained oxides [187,188]. Studies of Na^+ intercalation into SNO (4.15) as well as Li^+ doping experiments in related rare-earth perovskite nickelate systems ($EuNiO_3$ (ENO) and $NdNiO_3$ (NNO)) further suggest the generality of the electrochemical poling strategy to design ion shuttles in strongly correlated oxides (Figure 4.16).

4.3.2 Feasibility Studies on deploying SmNiO$_3$ as a Solid-State Electrolyte (SSE) for Lithium-ion Cell

Upon elucidating Li$^+$ interaction with SmNiO$_3$, the deployment of LiSmNiO$_3$ as a solid-state electrolyte for Li-ion battery requires an intricate design; the design has to meet the strict criteria of electro-chemo-mechanical compatibility between LiSmNiO$_3$ and its respective cathode and anode is of importance. In terms of electrochemical compatibility, the redox instability of the solid state electrolyte at either the anode or cathode can form SEI at one or the other interface, this is dependent upon the alignment of the SSE's valence band relative to the anode's conduction band, and the SSE's conduction band relative to the cathode's equilibrium energy eU_0, where U_0 is the open-circuit potential of the battery. In general, the SSE requires a bandgap $\Delta E_g > eU_0$, to achieve complete redox stability [189]. From the DFT calculations (Fig 4.11), Li-SNO has a bandgap of 3.1 eV, which is very narrow, as compared to other SSEs (LIPON $\sim$6 eV, LLZO$\sim$5.1 eV, and LGPS $\sim$3.6 eV [189]). This is further demonstrated in Figure 4.5a, when Li-SNO starts delithiating at 1.5 V against Li-metal. Clearly suggesting that Li-SNO would have a small potential window making it unsuitable for high voltage (>4 V) applications. A full solid-state device was then fabricated where the cell consists of LiCoO$_2$|Li-SNO|Si (Figure 4.17 inset). The device was successfully charged to 2.68 V before completely failing, achieving a specific gravimetric capacity of 1338 mAh g^{-1}, where Li$_x$Si, $x \approx 2.6$. The failure of the device, suggest a delamination of the Li-SNO across the Li-SNO|LiCoO$_2$ and Si|LiSNO interface, which can be contributed by the volume changes during lithiation and delithiation of Li-SNO and Si; $\sim$10% (Figure 4.11c) and $\sim$300%, respectively. Alternative failure modes would be the build up of an insulating SEI layer between the Li-SNO|LiCoO$_2$ interface. Future studies on the interface of the electrodes will determine the reason behind the failure of the solid-state battery.
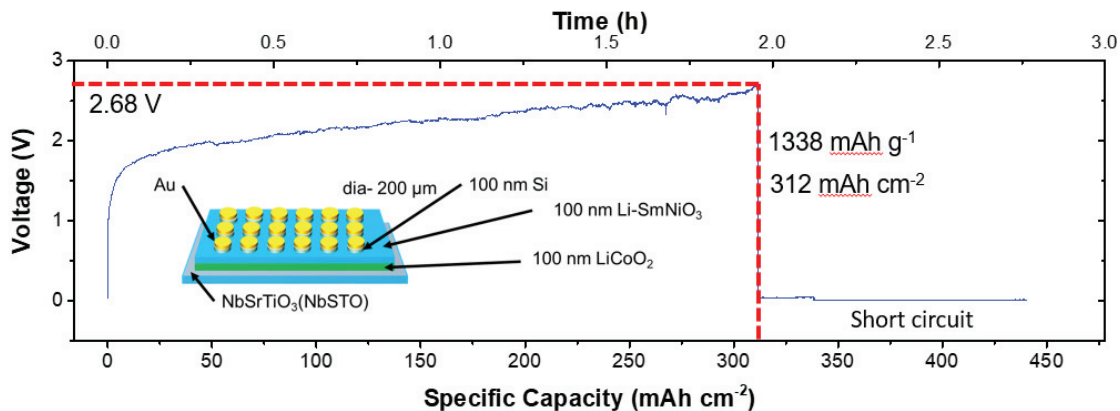
Fig. 4.17.: Solid-state lithium-ion full-cell of Au|Si|Li-SNO|LiCoO$_2$ sandwich-architecture. Galvanostatic charging of the as fabricated device from 2 – 4 V.The device failed at 2.68 V, with a specific gravimetric capacity of 1338 mAh g^{-1}. Figure prepared by D.L.

4.4 Conclusion

We demonstrate that cations such as Li$^+$, Na$^+$ can be reversibly incorporated into perovskite nickelate lattices under voltage bias in electrochemical cells. Strain due to ion incorporation in interstitial sites enables rapid diffusion with reduced activation barriers. The Mott transition that occurs concurrently due to the electron doping suppresses electronic transfer enabling selective ionic transport with tunable resistance states. The initial successful charging of the LiCoO$_2$|Li-SNO|Si illustrate the successful migration of Li$^+$ from the LiCoO$_2$ cathode through the Li-SNO to the Si anode, achieving a specific gravimetric capacity of 1338 mAh g^{-1}. However, further integration of LiSmNiO$_3$ as a solid-state electrolyte requires strict engineering design of cell, and extensive screening of electrodes, in-terms of electrochemical and chemo-mechanical compatibility.

5. SUMMARY

This dissertation presents an overall theme towards designing a Li-ion battery of the future with the attempt to solve the Li-ion batteries *trifecta* (good electrochemical performance, low cost, and improved safety). Starting from materials selection, process engineering, to device design and fabrication; specifically wheat-derived carbonaceous anodes, vanadium oxide cathode composites, and rare-earth nickelate solid-state electrolyte candidates.

In Chapter 2, a facile approach for the fabrication of low-cost, biomass-derived carbon from wheat flour, with promising lithium uptake was presented. Structural studies revealed that there exists an optimal carbonization temperature around 600 °C, at which the level of disorder in the carbon exhibits high lithiation capacities. Electrochemical studies of evolving carbon produced at higher temperatures (>1000 °C) exhibited lower irreversible capacity loss, but were subject to lower reversible capacity due to closure of nano pores. Carbon samples derived at 600 °C showed capacities (390 mAh g^{-1}) exceeding that of pure graphite, as well as good cycling performance (217 mAh g^{-1} at 1C lasting for 100 cycles). The elimination of any acid or basic pre-treatment, coupled with the lower synthesis temperature make wheat-derived carbon a desirable low-cost, high capacity carbon-based anode materials.

Chapter 3, utilizes aqueous sonochemical processing to synthesize V_2O_5 decorated 2D graphene nanoplatelets. The nanocomposites demonstrated improved lithium storage properties, as well as higher electronic conductivity. By inducing defects on the surface of graphene nanoplatelets via sonochemistry, homogeneously anchored V_2O_5 nanoparticles have enabled the composite to achieve high utilization of its Li-ion storage sites (294 mAh g^{-1}) for more than 5 cycles. When cycled at C/2, the material exhibits a low decay rate of 0.34%/cycle. The improvements are attributed to the increase in electronic conductivity and shorten Li^+ ion diffusion path in the

composite material. However, exposed surface nanostructures and weak bonding have limited the rate capabilities of the material, due to large chemo-mechanical stresses from high rate insertion/ extraction of Li^+ ions. By varying the GNPs content, a critical wt.% of GNPs:V_2O_5 is determined (20 wt.%), where there is a diminishing improvement in the electrochemical performance.

Lastly in Chapter 4, We demonstrate that cations such as Li^+, Na^+ can be reversibly incorporated into perovskite rare-earth nickelate lattices under voltage bias in electrochemical cells. Strain due to ion incorporation in interstitial sites enables rapid diffusion with reduced activation barriers. The Mott transition that occurs concurrently due to the electron doping suppresses electronic transfer enabling selective ionic transport with tunable resistance states. The initial successful charging of the $LiCoO_2$|Li-SNO|Si illustrate the successful migration of Li^+ from the $LiCoO_2$ cathode through the Li-SNO to the Si anode, achieving a specific gravimetric capacity of 1338 mAh g^{-1}.

REFERENCES

[1] United States Advanced Battery Consortium et al. Usabc goals for advanced batteries for evs-cy 2020 commercialization.

[2] MB Armand. "intercalation electrode" in materials for advanced batteries. In *NATO CONFERENCE SERIES, Series VI: Material Science*, volume 145. Plenum Press, 1980.

[3] M Lazzari and B Scrosati. A cyclable lithium organic electrolyte cell based on two intercalation electrodes. *ChemInform*, 11(29), 1980.

[4] W Weppner and Robert A Huggins. Determination of the kinetic parameters of mixed-conducting electrodes and application to the system li3sb. *Journal of The Electrochemical Society*, 124(10):1569–1578, 1977.

[5] Marc Doyle, Thomas F Fuller, and John Newman. Modeling of galvanostatic charge and discharge of the lithium/polymer/insertion cell. *Journal of the Electrochemical society*, 140(6):1526–1533, 1993.

[6] John OM Bockris, Amulya KN Reddy, and Maria Gamboa-Aldeco. Electrodics. *Modern Electrochemistry 2A: Fundamentals of Electrodics*, pages 1035–1400, 2000.

[7] Christian Julien, Alain Mauger, Ashok Vijh, and Karim Zaghib. *Lithium batteries: science and technology*. Springer, 2015.

[8] Yoshio Masaki, J Brodd Ralph, and K Akiya. *Lithium-ion batteries: science and technologies*. New York, USA: Springer, Cambridge University, 2010.

[9] Naoki Nitta, Feixiang Wu, Jung Tae Lee, and Gleb Yushin. Li-ion battery materials: present and future. *Materials today*, 18(5):252–264, 2015.

[10] George E Blomgren. The development and future of lithium ion batteries. *Journal of The Electrochemical Society*, 164(1):A5019–A5025, 2017.

[11] Paul Albertus, Susan Babinec, Scott Litzelman, and Aron Newman. Status and challenges in enabling the lithium metal electrode for high-energy and low-cost rechargeable batteries. *Nature Energy*, page 1, 2017.

[12] Björn Nykvist and Måns Nilsson. Rapidly falling costs of battery packs for electric vehicles. *nature climate change*, 5(4):329, 2015.

[13] O Schmidt, A Hawkes, A Gambhir, and I Staffell. The future cost of electrical energy storage based on experience rates. *Nature Energy*, 2(8):17110, 2017.

[14] Linda Gaines and Roy Cuenca. Costs of lithium-ion batteries for vehicles. Technical report, Argonne National Lab., IL (US), 2000.

[15] Hanna Vikström, Simon Davidsson, and Mikael Höök. Lithium availability and future production outlooks. *Applied Energy*, 110:252–266, 2013.

[16] Paul W Gruber, Pablo A Medina, Gregory A Keoleian, Stephen E Kesler, Mark P Everson, and Timothy J Wallington. Global lithium availability. *Journal of Industrial Ecology*, 15(5):760–775, 2011.

[17] Jamie Speirs, Marcello Contestabile, Yassine Houari, and Robert Gross. The future of lithium availability for electric vehicle batteries. *Renewable and Sustainable Energy Reviews*, 35:183–193, 2014.

[18] Camille Grosjean, Pamela Herrera Miranda, Marion Perrin, and Philippe Poggi. Assessment of world lithium resources and consequences of their geographic distribution on the expected development of the electric vehicle industry. *Renewable and Sustainable Energy Reviews*, 16(3):1735–1744, 2012.

[19] Paul A Nelson, Kevin G Gallagher, Ira D Bloom, and Dennis W Dees. Modeling the performance and cost of lithium-ion batteries for electric-drive vehicles. Technical report, Argonne National Laboratory (ANL), 2012.

[20] David L Wood, Jianlin Li, and Claus Daniel. Prospects for reducing the processing cost of lithium ion batteries. *Journal of Power Sources*, 275:234–242, 2015.

[21] Sung-Yoon Chung, Jason T Bloking, and Yet-Ming Chiang. Electronically conductive phospho-olivines as lithium storage electrodes. *Nature materials*, 1(2):123, 2002.

[22] Jongwoo Lim, Yiyang Li, Daan Hein Alsem, Hongyun So, Sang Chul Lee, Peng Bai, Daniel A Cogswell, Xuzhao Liu, Norman Jin, Young-sang Yu, et al. Origin and hysteresis of lithium compositional spatiodynamics within battery primary particles. *Science*, 353(6299):566–571, 2016.

[23] Dingchang Lin, Yayuan Liu, and Yi Cui. Reviving the lithium metal anode for high-energy batteries. *Nature nanotechnology*, 12(3):194, 2017.

[24] Jang Wook Choi and Doron Aurbach. Promise and reality of post-lithium-ion batteries with high energy densities. *Nature Reviews Materials*, 1(4):16013, 2016.

[25] Yanpeng Guo, Huiqiao Li, and Tianyou Zhai. Reviving lithium-metal anodes for next-generation high-energy batteries. *Advanced Materials*, 2017.

[26] Bin Li, Ying Wang, and Shubin Yang. A material perspective of rechargeable metallic lithium anodes. *Advanced Energy Materials*, 2018.

[27] Arumugam Manthiram, Xingwen Yu, and Shaofei Wang. Lithium battery chemistries enabled by solid-state electrolytes. *Nature Reviews Materials*, 2(4):16103, 2017.

[28] Kian Kerman, Alan Luntz, Venkatasubramanian Viswanathan, Yet-Ming Chiang, and Zhebo Chen. practical challenges hindering the development of solid state li ion batteries. *Journal of The Electrochemical Society*, 164(7):A1731–A1744, 2017.

[29] Robert D Schmidt and Jeffrey Sakamoto. In-situ, non-destructive acoustic characterization of solid state electrolyte cells. *Journal of Power Sources*, 324:126–133, 2016.

[30] Kun Kelvin Fu, Yunhui Gong, Gregory T Hitz, Dennis W McOwen, Yiju Li, Shaomao Xu, Yang Wen, Lei Zhang, Chengwei Wang, Glenn Pastel, et al. Three-dimensional bilayer garnet solid electrolyte based high energy density lithium metal–sulfur batteries. *Energy & Environmental Science*, 10(7):1568–1575, 2017.

[31] Xiaogang Han, Yunhui Gong, Kun Kelvin Fu, Xingfeng He, Gregory T Hitz, Jiaqi Dai, Alex Pearse, Boyang Liu, Howard Wang, Gary Rubloff, et al. Negating interfacial impedance in garnet-based solid-state li metal batteries. *Nature materials*, 16(5):572, 2017.

[32] J-M Tarascon. Key Challenges in Future Li-Battery Research. *Philosophical Transactions of the Royal Society of London A: Mathematical, Physical and Engineering Sciences*, 368(1923):3227–3241, 2010.

[33] Vinodkumar Etacheri, Rotem Marom, Ran Elazari, Gregory Salitra, and Doron Aurbach. Challenges in the development of advanced Li-ion batteries: a review. *Energy & Environmental Science*, 4(9):3243–3262, 2011.

[34] Peter G. Bruce, Bruno Scrosati, and JeanMarie Tarascon. Nanomaterials for rechargeable lithium batteries. *Angewandte Chemie International Edition*, 47(16):2930–2946, 2008.

[35] J-M Tarascon and Michel Armand. Issues and challenges facing rechargeable lithium batteries. *Nature*, 414(6861):359–367, 2001.

[36] Hong Li, Zhaoxiang Wang, Liquan Chen, and Xuejie Huang. Research on Advanced Materials for Liion Batteries. *Advanced Materials*, 21(45):4593–4607, 2009.

[37] Weibing Xing, J S Xue, Tao Zheng, A Gibaud, and J R Dahn. Correlation between lithium intercalation capacity and microstructure in hard carbons. *Journal of The Electrochemical Society*, 143(11):3482–3491, 1996.

[38] J. S. Gnanaraj, M. D. Levi, E. Levi, G. Salitra, D. Aurbach, John E. Fischer, and Agnes Claye. Comparison between the electrochemical behavior of disordered carbons and graphite electrodes in connection with their structure. *Journal of The Electrochemical Society*, 148(6):A525–A536, 2001.

[39] Juan Yang, Xiang-yang Zhou, Jie Li, You-lan Zou, and Jing-jing Tang. Study of nano-porous hard carbons as anode materials for lithium ion batteries. *Materials Chemistry and Physics*, 135(2):445–450, 2012.

[40] Wenbin Li, Mingming Chen, and Chengyang Wang. Spherical hard carbon prepared from potato starch using as anode material for Li-ion batteries. *Materials Letters*, 65(23):3368–3370, 2011.

[41] Hongqiang Wang, Qifa Dai, Qingyu Li, Jianhong Yang, Xinxian Zhong, Youguo Huang, Anna Zhang, and Zhixiong Yan. Preparation of porous carbon spheres from porous starch. *Solid State Ionics*, 180(26):1429–1432, 2009.

[42] Tao Liu, Ruiying Luo, Wenming Qiao, Seong-Ho Yoon, and Isao Mochida. Microstructure of carbon derived from mangrove charcoal and its application in Li-ion batteries. *Electrochimica Acta*, 55(5):1696–1700, 2010.

[43] G. Ting-Kuo Fey, D. C. Lee, Y. Y. Lin, and T. Prem Kumar. High-capacity disordered carbons derived from peanut shells as lithium-intercalating anode materials. *Synthetic metals*, 139(1):71–80, 2003.

[44] Yun Ju Hwang, Soo Kyung Jeong, Kee Suk Nahm, Jae Sun Shin, and A Manuel Stephan. Pyrolytic carbon derived from coffee shells as anode materials for lithium batteries. *Journal of Physics and Chemistry of Solids*, 2(68):182–188, 2007.

[45] Xinliang Yu, Kaiyou Zhang, Ning Tian, Aimiao Qin, Lei Liao, Rui Du, and Chun Wei. Biomass carbon derived from sisal fiber as anode material for lithium-ion batteries. *Materials Letters*, 142:193–196, 2015.

[46] A Manuel Stephan, T. Prem Kumar, R. Ramesh, Sabu Thomas, Soo Kyung Jeong, and Kee Suk Nahm. Pyrolitic carbon from biomass precursors as anode materials for lithium batteries. *Materials Science and Engineering: A*, 430(1):132–137, 2006.

[47] Liping Wang, Zoe Schnepp, and Maria Magdalena Titirici. Rice husk-derived carbon anodes for lithium ion batteries. *Journal of Materials Chemistry A*, 1(17):5269–5273, 2013.

[48] George Ting-Kuo Fey and Chung-Lai Chen. High-capacity carbons for lithium-ion batteries prepared from rice husk. *Journal of power sources*, 97:47–51, 2001.

[49] Feng Zhang, Kai-Xue Wang, Guo-Dong Li, and Jie-Sheng Chen. Hierarchical porous carbon derived from rice straw for lithium ion batteries with high-rate performance. *Electrochemistry Communications*, 11(1):130–133, 2009.

[50] XingLong Wu, LiLi Chen, Sen Xin, YaXia Yin, YuGuo Guo, QingShan Kong, and YanZhi Xia. Preparation and Li storage properties of hierarchical porous carbon fibers derived from alginic acid. *ChemSusChem*, 3(6):703–707, 2010.

[51] Alvaro Caballero, Lourdes Hernán, and Julián Morales. Limitations of Disordered Carbons Obtained from Biomass as Anodes for Real LithiumIon Batteries. *ChemSusChem*, 4(5):658–663, 2011.

[52] J. C. Arrebola, A Caballero, L. Hernán, J. Morales, M. Olivares-Marín, and V. Gómez-Serrano. Improving the performance of biomass-derived carbons in Li-ion batteries by controlling the lithium insertion process. *Journal of The Electrochemical Society*, 157(7):A791–A797, 2010.

[53] Jian Jiang, Jianhui Zhu, Wei Ai, Zhanxi Fan, Xiaonan Shen, Chenji Zou, Jinping Liu, Hua Zhang, and Ting Yu. Evolution of disposable bamboo chopsticks into uniform carbon fibers: a smart strategy to fabricate sustainable anodes for Li-ion batteries. *Energy & Environmental Science*, 7(8):2670–2679, 2014.

[54] Li Chen, Yongzhi Zhang, Chaohong Lin, Wen Yang, Yan Meng, Yong Guo, Menglong Li, and Dan Xiao. Hierarchically porous nitrogen-rich carbon derived from wheat straw as an ultra-high-rate anode for lithium ion batteries. *Journal of Materials Chemistry A*, 2(25):9684–9690, 2014.

[55] Vitaly Budarin, James H. Clark, Jeffrey J. E. Hardy, Rafael Luque, Krzysztof Milkowski, Stewart J. Tavener, and Ashley J. Wilson. Starbons: New StarchDerived Mesoporous Carbonaceous Materials with Tunable Properties. *Angewandte Chemie*, 118(23):3866–3870, 2006.

[56] Food Agriculture Organization of the United Nations. Crops National Production : Cereal. Technical report, Rome, Italy, 2014.

[57] J. J. M Swinkels. Composition and properties of commercial native starches. *StarchStärke*, 37(1):1–5, 1985.

[58] B E Warren. XRay Diffraction Study of Carbon Black. *The Journal of Chemical Physics*, 2(9):551–555, 1934.

[59] Wojciech Ciesielski, Bohdan Achremowicz, Piotr Tomasik, Malgorzata Baczkowicz, and Jaroslaw Korus. Starch radicals. Part II: cerealsnative starch complexes. *Carbohydrate polymers*, 34(4):303–308, 1997.

[60] Wojciech Ciesielski and Piotr Tomasik. Starch radicals. Part I. Thermolysis of plain starch. *Carbohydrate polymers*, 31(4):205–210, 1996.

[61] Xingxun Liu, Long Yu, Hongsheng Liu, Ling Chen, and Lin Li. In situ thermal decomposition of starch with constant moisture in a sealed system. *Polymer Degradation and Stability*, 93(1):260–262, 2008.

[62] Poonam Aggarwal and David Dollimore. A thermal analysis investigation of partially hydrolyzed starch. *Thermochimica Acta*, 319(1):17–25, 1998.

[63] Andrea C. Ferrari and J.F. Robertson. Interpretation of Raman spectra of disordered and amorphous carbon. *Physical review B*, 61(20):14095, 2000.

[64] Vilas G. Pol and Michael M. Thackeray. Spherical carbon particles and carbon nanotubes prepared by autogenic reactions: evaluation as anodes in lithium electrochemical cells. *Energy & Environmental Science*, 4(5):1904–1912, 2011.

[65] Michael Mowry, Dennis Palaniuk, Claudia C. Luhrs, and Sebastian Osswald. In situ Raman spectroscopy and thermal analysis of the formation of nitrogen-doped graphene from urea and graphite oxide. *RSC Advances*, 3(44):21763–21775, 2013.

[66] Vilas G. Pol, Jianguo Wen, Kah Chun Lau, Samantha Callear, Daniel T. Bowron, Chi-Kai Lin, Sanket A Deshmukh, Subramanian Sankaranarayanan, Larry A Curtiss, and William I F David. Probing the evolution and morphology of hard carbon spheres. *Carbon*, 68:104–111, 2014.

[67] B. M. Jenkins, L. L. Baxter, T. R. Miles Jr, and T. R. Miles. Combustion properties of biomass. *Fuel processing technology*, 54(1-3):17–46, 1998.

[68] R. K. Sharma, J. B. Wooten, V. L. Baliga, and M. R. Hajaligol. Characterization of chars from biomass-derived materials: pectin chars. *Fuel*, 80(12):1825–1836, 2001.

[69] Andrea Monti, Nicola Di Virgilio, and Gianpietro Venturi. Mineral composition and ash content of six major energy crops. *Biomass and Bioenergy*, 32(3):216–223, 2008.

[70] Charan Masarapu, Venkatachalam Subramanian, Hongwei Zhu, and Bingqing Wei. Long-cycle electrochemical behavior of multiwall carbon nanotubes synthesized on stainless steel in li ion batteries. *Advanced Functional Materials*, 19(7):1008–1014, 2009.

[71] Tiehua Piao, Su-Moon Park, Chil-Hoon Doh, and Seong-In Moon. Intercalation of lithium ions into graphite electrodes studied by ac impedance measurements. *Journal of The Electrochemical Society*, 146(8):2794–2798, 1999.

[72] Yu-Chi Chang, Jyh-Hwa Jong, and George Ting-Kuo Fey. Kinetic characterization of the electrochemical intercalation of lithium ions into graphite electrodes. *Journal of The Electrochemical Society*, 147(6):2033–2038, 2000.

[73] Tao Zheng, W. R. McKinnon, and J. R. Dahn. Hysteresis during Lithium Insertion in Hydrogen-Containing Carbons. *Journal of the Electrochemical Society*, 143(7):2137–2145, 1996.

[74] Edward Buiel and J. R. Dahn. Li-insertion in hard carbon anode materials for Li-ion batteries. *Electrochimica acta*, 45(1):121–130, 1999.

[75] M. Stanley Whittingham. Lithium batteries and cathode materials. *Chemical Reviews*, 104(10):4271–4301, 2004.

[76] Jing Xu, Feng Lin, Marca M. Doeff, and Wei Tong. A review of Ni-based layered oxides for rechargeable Li-ion batteries. *J. Mater. Chem. A*, 5(3):874–901, 2017.

[77] J. S. Braithwaite, C. R. A. Catlow, J. D. Gale, and J. H. Harding. Lithium Intercalation into Vanadium Pentoxide : a Theoretical Study. *Chemistry of Materials*, 11(15):1990–1998, 1999.

[78] K. West, B. Zachau-Christiansen, T. Jacobsen, and S. Skaarup. Lithium insertion into vanadium pentoxide bronzes. *Solid State Ionics*, 76(1-2):15–21, 1995.

[79] B. J. Hwang, Y. W. Tsai, D. Carlier, and G. Ceder. A combined computational/experimental study on $LiNi_{1/3}Co_{1/3}Mn_{1/3}O_2$. *Chemistry of Materials*, 15(19):3676–3682, 2003.

[80] Naoaki Yabuuchi and Tsutomu Ohzuku. Novel lithium insertion material of $LiCo_{1/3}Ni_{1/3}Mn_{1/3}O_2$ for advanced lithium-ion batteries. *Journal of Power Sources*, 119-121:171–174, 2003.

[81] Y. M. Chiang, H. Wang, and Y. I. Jang. Electrochemically induced cation disorder and phase transformations in lithium intercalation oxides. *Chemistry of Materials*, 13(1):53–63, 2001.

[82] Do Kyung Kim, P. Muralidharan, Hyun-Wook Lee, Riccardo Ruffo, Yuan Yang, Candace K. Chan, Hailin Peng, Robert A. Huggins, and Yi Cui. Spinel $LiMn_2O_4$ Nanorods as Lithium Ion Battery Cathodes. *Nano Letters*, 8(11):3948–3952, 2008.

[83] Takashi Watanabe, Yuji Ikeda, Takashi Ono, Mitsuhiro Hibino, Maiko Hosoda, Keiji Sakai, and Tetsuichi Kudo. Characterization of vanadium oxide sol as a starting material for high rate intercalation cathodes. *Solid State Ionics*, 151(1-4):313–320, 2002.

[84] Jörg Muster, Gyu Tae Kim, Vojislav Krstic, Jin Gyu Park, Yung Woo Park, Siegmar Roth, and Marko Burghard. Electrical Transport Through individual Vanadium Pentoxide Nanowires.pdf. *Advanced Materials*, 12(6):420–424, 2000.

[85] J M Cocciantelli, M. Ménétrier, C. Delmas, J. P. Doumerc, M. Pouchard, M. Broussely, and J. Labat. On the delta to gamma irreversible transformation in Li//V$_2$O$_5$ secondary batteries. *Solid State Ionics*, 78(1-2):143–150, 1995.

[86] C. Delmas, H. Cognac-Auradou, J. M. Cocciantelli, M. Ménétrier, and J. P. Doumerc. The Li$_x$V$_2$O$_5$ system: An overview of the structure modifications induced by the lithium intercalation. *Solid State Ionics*, 69(3-4):257–264, 1994.

[87] Anqiang Pan, Ji-Guang Zhang, Zimin Nie, Guozhong Cao, Bruce W. Arey, Guosheng Li, Shu-quan Liang, and Jun Liu. Facile synthesized nanorod structured vanadium pentoxide for high-rate lithium batteries. *Journal of Materials Chemistry*, 20(41):9193–9199, 2010.

[88] Liqiang Mai, Fei Dong, Xu Xu, Yanzhu Luo, Qinyou An, Yunlong Zhao, Jie Pan, and Jingnan Yang. Cucumber-like V$_2$O$_5$/poly (3, 4-ethylenedioxythiophene) & MnO$_2$ nanowires with enhanced electrochemical cyclability. *Nano letters*, 13(2):740–745, 2013.

[89] Yue Zhang, Yizhi Wang, Zhihong Xiong, Yongming Hu, Weixing Song, Qiu-an Huang, Xiaoxing Cheng, Long-Qing Chen, Chunwen Sun, and Haoshuang Gu. V$_2$O$_5$ Nanowire Composite Paper as a High-Performance Lithium-Ion Battery Cathode. *ACS Omega*, 2(3):793–799, 2017.

[90] D. W. Su, S. X. Dou, and G. X. Wang. Hierarchical orthorhombic V$_2$O$_5$ hollow nanospheres as high performance cathode materials for sodium-ion batteries. *Journal of Materials Chemistry A*, 2(29):11185, 2014.

[91] Suqing Wang, Zhenda Lu, Da Wang, Chunguang Li, Chunhua Chen, and Yadong Yin. Porous monodisperse V$_2$O$_5$ microspheres as cathode materials for lithium-ion batteries. *Journal of Materials Chemistry*, 21(17):6365, 2011.

[92] Xiaochuan Ren, Yanjun Zhai, Lin Zhu, Yanyan He, Aihua Li, Chunli Guo, and Liqiang Xu. Fabrication of Various V$_2$O$_5$ Hollow Microspheres as Excellent Cathode for Lithium Storage and the Application in Full Cells. *ACS Applied Materials and Interfaces*, 8(27):17205–17211, 2016.

[93] Jie Shao, Xinyong Li, Zhongming Wan, Longfei Zhang, Yuanlei Ding, Li Zhang, Qunting Qu, and Honghe Zheng. Low-cost synthesis of hierarchical V$_2$O$_5$ microspheres as high-performance cathode for lithium-ion batteries. *ACS Applied Materials and Interfaces*, 5(16):7671–7675, 2013.

[94] Jun Liu, Hui Xia, Dongfeng Xue, and Li Lu. Double-Shelled Nanocapsules of V$_2$O$_5$ -Based Composites as High-Performance Anode and Cathode Materials for Li Ion Batteries. *J. Am. Chem. Soc.*, 131:12086–12087, 2009.

[95] Hong-En Wang, Dai-Song Chen, Yi Cai, Run-Lin Zhang, Jun-Meng Xu, Zhao Deng, Xian-Feng Zheng, Yu Li, Igor Bello, and Bao-Lian Su. Facile synthesis of hierarchical and porous V$_2$O$_5$ microspheres as cathode materials for lithium ion batteries. *Journal of Colloid and Interface Science*, 418:74–80, 2014.

[96] Hongwei Bai, Zhaoyang Liu, Darren Delai Sun, and Siew Hwa Chan. Hierarchical 3d micro-/nano- V_2O_5 (vanadium pentoxide) spheres as cathode materials for high-energy and high-power lithium ion-batteries. *Energy*, 76:607–613, 2014.

[97] Feifan Guo, Meihong Fan, Panpan Jin, Hui Chen, Yuanyuan Wu, Guo-Dong Li, and Xiaoxin Zou. Precursor-mediated synthesis of double-shelled V_2O_5 hollow nanospheres as cathode material for lithium-ion batteries. *CrystEngComm*, 18(22):4068–4073, 2016.

[98] Candace K. Chan, Hailin Peng, Ray D. Twesten, Konrad Jarausch, Xiao Feng Zhang, and Yi Cui. Fast, completely reversible Li insertion in vanadium pentoxide nanoribbons. *Nano Letters*, 7(2):490–495, 2007.

[99] V. M. Mohan, Bin Hu, Weiliang Qiu, and Wen Chen. Synthesis, structural, and electrochemical performance of V_2O_5 nanotubes as cathode material for lithium battery. *J. Appl. Electrochem.*, 39:2001–2006, 2009.

[100] Xianhong Rui, Ziyang Lu, Hong Yu, Dan Yang, Huey Hoon Hng, Tuti Mariana Lim, and Qingyu Yan. Ultrathin V_2O_5 nanosheet cathodes: realizing ultrafast reversible lithium storage. *Nanoscale*, 5(2):556–560, 2013.

[101] Xiang Peng, Xuming Zhang, Lei Wang, Liangsheng Hu, Samson Ho Sum Cheng, Chao Huang, Biao Gao, Fei Ma, Kaifu Huo, and Paul K. Chu. Hydrogenated V_2O_5 nanosheets for superior lithium storage properties. *Advanced Functional Materials*, 26(5):784–791, 2016.

[102] Xinyi Chen, Hongli Zhu, Yu-Chen Chen, Yuanyuan Shang, Anyuan Cao, Liangbing Hu, and Gary W. Rubloff. MWCNT/V_2O_5 core/shell sponge for high areal capacity and power density Li-ion cathodes. *ACS nano*, 6(9):7948–7955, 2012.

[103] M. Sathiya, A. S. Prakash, K. Ramesha, J. M. Tarascon, and A. K. Shukla. V_2O_5-anchored carbon nanotubes for enhanced electrochemical energy storage. *Journal of the American Chemical Society*, 133(40):16291–16299, 2011.

[104] Yuqiang Qian, Anh Vu, William Smyrl, and Andreas Stein. Facile preparation and electrochemical properties of V_2O_5-graphene composite films as free-standing cathodes for rechargeable lithium batteries. *Journal of the Electrochemical Society*, 159(8):A1135–A1140, 2012.

[105] Yang Yang, Lei Li, Huilong Fei, Zhiwei Peng, Gedeng Ruan, and James M. Tour. Graphene nanoribbon/V_2O_5 cathodes in lithium-ion batteries. *ACS Applied Materials and Interfaces*, 6(12):9590–9594, 2014.

[106] Qi Liu, Zhe-Fei Li, Yadong Liu, Hangyu Zhang, Yang Ren, Cheng-Jun Sun, Wenquan Lu, Yun Zhou, Lia Stanciu, Eric A. Stach, and Jian Xie. Graphene-modified nanostructured vanadium pentoxide hybrids with extraordinary electrochemical performance for Li-ion batteries. *Nature Communications*, 6:6127, 2015.

[107] Maxim Koltypin, Vilas Pol, Aharon Gedanken, and Doron Aurbach. The Study of Carbon-Coated V_2O_5 Nanoparticles as a Potential Cathodic Material for Li Rechargeable Batteries. *Journal of The Electrochemical Society*, 154(7):A605, 2007.

[108] Xiao-Fei Zhang, Kai-Xue Wang, Xiao Wei, and Jie-Sheng Chen. Carbon-coated V_2O_5 nanocrystals as high performance cathode material for lithium ion batteries. *Chemistry of Materials*, 23(24):5290–5292, 2011.

[109] H. Yamada, K. Tagawa, M. Komatsu, I. Moriguchi, and T. Kudo. High Power Battery Electrodes Using Nanoporous V_2O_5/Carbon Composites. *Journal of Physical Chemistry C*, 111(23):8397–8402, 2007.

[110] Hongmei Zeng, Deyu Liu, Yichi Zhang, Kimberly A. See, Young Si Jun, Guang Wu, Jeffrey A. Gerbec, Xiulei Ji, and Galen D. Stucky. Nanostructured Mn-Doped V_2O_5 Cathode Material Fabricated from Layered Vanadium Jarosite. *Chemistry of Materials*, 27(21):7331–7336, 2015.

[111] Yanwei Li, Jinhuan Yao, Evan Uchaker, Ming Zhang, Jianjun Tian, Xiaoyan Liu, and Guozhong Cao. Sn-doped V_2O_5 film with enhanced lithium-ion storage performance. *Journal of Physical Chemistry C*, 117(45):23507–23514, 2013.

[112] Xinyuan Li, Chaofeng Liu, Changkun Zhang, Haoyu Fu, Xihui Nan, Wenda Ma, Zhuoyu Li, Kan Wang, Haibo Wu, and Guozhong Cao. Effects of Preinserted Na Ions on Li-Ion Electrochemical Intercalation Properties of V_2O_5. *ACS Applied Materials and Interfaces*, 8(37):24629–24637, 2016.

[113] Wenda Ma, Changkun Zhang, Chaofeng Liu, Xihui Nan, Haoyu Fu, and Guozhong Cao. Impacts of Surface Energy on Lithium Ion Intercalation Properties of V_2O_5. *ACS Applied Materials and Interfaces*, 8(30):19542–19549, 2016.

[114] Dawei Liu, Yanyi Liu, Anqiang Pan, Kenneth P. Nagle, Gerald T. Seidler, Yoon Ha Jeong, and Guozhong Cao. Enhanced lithium-ion intercalation properties of V_2O_5 xerogel electrodes with surface defects. *Journal of Physical Chemistry C*, 115(11):4959–4965, 2011.

[115] Yun Xu, Marco Dunwell, Ling Fei, Engang Fu, Qianglu Lin, Brian Patterson, Bin Yuan, Shuguang Deng, Paul Andersen, Hongmei Luo, and Guifu Zou. Two-dimensional V_2O_5 sheet network as electrode for lithium-ion batteries. *ACS Applied Materials and Interfaces*, 6(22):20408–20413, 2014.

[116] J. S. Gnanaraj, V. G. Pol, A. Gedanken, and D. Aurbach. Improving the high-temperature performance of $LiMn_2O_4$ spinel electrodes by coating the active mass with MgO via a sonochemical method. *Electrochemistry Communications*, 5(11):940–945, 2003.

[117] V. G. Pol, M. Motiei, A. Gedanken, J. Calderon-Moreno, and Y. Mastai. Sonochemical deposition of air-stable iron nanoparticles on monodispersed carbon spherules. *Chemistry of Materials*, 15(6):1378–1384, 2003.

[118] V. G. Pol, R. Reisfeld, and A. Gedanken. Sonochemical synthesis and optical properties of europium oxide nanolayer coated on titania. *Chemistry of Materials*, 14(9):3920–3924, 2002.

[119] Aharon Gedanken. Using sonochemistry for the fabrication of nanomaterials. *Ultrasonics Sonochemistry*, 11(2):47–55, 2004.

[120] Cristina Leonelli and Timothy J. Mason. Microwave and ultrasonic processing: Now a realistic option for industry. *Chemical Engineering and Processing: Process Intensification*, 49(9):885–900, 2010.

[121] Giancarlo Cravotto and Pedro Cintas. Power ultrasound in organic synthesis: moving cavitational chemistry from academia to innovative and large-scale applications. *Chem. Soc. Rev.*, 35(2):180–196, 2006.

[122] Jin Ho Bang and Kenneth S. Suslick. Applications of ultrasound to the synthesis of nanostructured materials. *Advanced Materials*, 22(10):1039–1059, 2010.

[123] S. H. Xie, Y. Y. Liu, and J. Y. Li. Comparison of the effective conductivity between composites reinforced by graphene nanosheets and carbon nanotubes. *Applied Physics Letters*, 92(24), 2008.

[124] Dmitry G. Shchukin, Ekaterina Skorb, Valentina Belova, and Helmuth Möhwald. Ultrasonic cavitation at solid surfaces. *Advanced Materials*, 23(17):1922–1934, 2011.

[125] S. I. Nikitenko, L. Venault, and P. H. Moisy. Scavenging of OH^- radicals produced from H_2O sonolysis with nitrate ions. *Ultrasonics Sonochemistry*, 11(3-4):139–142, 2004.

[126] P. K. Chendke and H. S. Fogler. Second-order sonochemical phenomena-extensions of previous work and applications in industrial processing. *The Chemical Engineering Journal*, 8(3):165–178, 1974.

[127] Fabrice Guittonneau, Abdesselam Abdelouas, Bernd Grambow, and Sandrine Huclier. The effect of high power ultrasound on an aqueous suspension of graphite. *Ultrasonics Sonochemistry*, 17(2):391–398, 2010.

[128] Rita Baddour-Hadjean and Jean-Pierre Pereira-Ramos. Raman Microspectrometry Applied to the Study of Electrode Materials for Lithium Batteries. *Chemical Reviews*, 110(3):1278–1319, 2009.

[129] R Baddour-Hadjean, E Raekelboom, and JP Pereira-Ramos. New structural characterization of the $Li_xV_2O_5$ system provided by raman spectroscopy. *Chemistry of materials*, 18(15):3548–3556, 2006.

[130] Gregory a. Horrocks, Maliek F. Likely, Jesus M. Velazquez, and Sarbajit Banerjee. Finite size effects on the structural progression induced by lithiation of V_2O_5: a combined diffraction and Raman spectroscopy study. *Journal of Materials Chemistry A*, 1:15265, 2013.

[131] Franklin D. Hardcastle and Israel E. Wachs. Determination of vanadium-oxygen bond distances and bond orders by raman spectroscopy. *The Journal of Physical Chemistry*, 95(13):5031–5041, 1991.

[132] Eric A. Meulenkamp, W. Van Klinken, and A. R. Schlatmann. In-situ X-ray diffraction of Li intercalation in sol-gel V_2O_5 films. *Solid State Ionics*, 126(3):235–244, 1999.

[133] M. Umeda, K. Dokko, Y. Fujita, M. Mohamedi, I. Uchida, and J. R. Selman. Electrochemical impedance study of Li-ion insertion into mesocarbon microbead single particle electrode: Part I. Graphitized carbon. *Electrochimica Acta*, 47(6):885–890, 2001.

[134] D. G. Lim, D.-W. Chung, R. Kohler, J. Proell, C. Scherr, W. Pfleging, and R. E. Garcia. Designing 3D Conical-Shaped Lithium-Ion Microelectrodes. *Journal of the Electrochemical Society*, 161(3):A302–A307, 2013.

[135] Satria Zulkarnaen Bisri, Sunao Shimizu, Masaki Nakano, and Yoshihiro Iwasa. Endeavor of iontronics: From fundamentals to applications of ion-controlled electronics. *Advanced Materials*, 2017.

[136] AL Krick and SJ May. Evidence for oxygen vacancy manipulation in $La_{1/3}Sr_{2/3}FeO_3$-δ thin films via voltage controlled solid-state ionic gating. *APL Materials*, 5(4):042504, 2017.

[137] John Christopher Bachman, Sokseiha Muy, Alexis Grimaud, Hao-Hsun Chang, Nir Pour, Simon F Lux, Odysseas Paschos, Filippo Maglia, Saskia Lupart, Peter Lamp, et al. Inorganic solid-state electrolytes for lithium batteries: mechanisms and properties governing ion conduction. *Chemical reviews*, 116(1):140–162, 2015.

[138] Yoshikatsu Seino, Tsuyoshi Ota, Kazunori Takada, Akitoshi Hayashi, and Masahiro Tatsumisago. A sulphide lithium super ion conductor is superior to liquid ion conductors for use in rechargeable batteries. *Energy & Environmental Science*, 7(2):627–631, 2014.

[139] Yuki Kato, Satoshi Hori, Toshiya Saito, Kota Suzuki, Masaaki Hirayama, Akio Mitsui, Masao Yonemura, Hideki Iba, and Ryoji Kanno. High-power all-solid-state batteries using sulfide superionic conductors. *Nature Energy*, 1(4):16030, 2016.

[140] R Prasada Rao and S Adams. Studies of lithium argyrodite solid electrolytes for all-solid-state batteries. *Physica Status Solidi (a)*, 208(8):1804–1807, 2011.

[141] Hisanori Yamane, Shinichi Kikkawa, and Mitsue Koizumi. Preparation of lithium silicon nitrides and their lithium ion conductivity. *Solid State Ionics*, 25(2-3):183–191, 1987.

[142] Gholamabbas Nazri. Preparation, structure and ionic conductivity of lithium phosphide. *Solid State Ionics*, 34(1-2):97–102, 1989.

[143] Yaoyu Ren, Kai Chen, Rujun Chen, Ting Liu, Yibo Zhang, and Ce-Wen Nan. Oxide electrolytes for lithium batteries. *Journal of the American Ceramic Society*, 98(12):3603–3623, 2015.

[144] AR Rodger, J Kuwano, and AR West. Li^+ ion conducting γ solid solutions in the systems Li_4XO_4-Li_3O_4: X= Si, Ge, Ti; Y= P, As, V; Li_4XO_4-$LiZO_2$: Z= Al, Ga, Cr and Li_4GeO_4-Li_2CaGeO_4. *Solid State Ionics*, 15(3):185–198, 1985.

[145] Hiromichi Aono, Eisuke Sugimoto, Yoshihiko Sadaoka, Nobuhito Imanaka, and Gin-ya Adachi. Ionic conductivity of solid electrolytes based on lithium titanium phosphate. *Journal of the electrochemical society*, 137(4):1023–1027, 1990.

[146] Xiaohua Yu, JB Bates, GE Jellison, and FX Hart. A stable thin-film lithium electrolyte: Lithium phosphorus oxynitride. *Journal of the electrochemical society*, 144(2):524–532, 1997.

[147] AM Glass, Kurt Nassau, and TJ Negran. Ionic conductivity of quenched alkali niobate and tantalate glasses. *Journal of Applied Physics*, 49(9):4808–4811, 1978.

[148] Yoshiyuki Inaguma, Chen Liquan, Mitsuru Itoh, Tetsurō Nakamura, Takashi Uchida, Hiromasa Ikuta, and Masataka Wakihara. High ionic conductivity in lithium lanthanum titanate. *Solid State Communications*, 86(10):689–693, 1993.

[149] Carlos Bernuy-Lopez, William Manalastas Jr, Juan Miguel Lopez del Amo, Ainara Aguadero, Frederic Aguesse, and John A Kilner. Atmosphere controlled processing of ga-substituted garnets for high li-ion conductivity ceramics. *Chemistry of Materials*, 26(12):3610–3617, 2014.

[150] José A Alonso, Jesús Sanz, Jacobo Santamaría, Carlos León, Alejandro Várez, and Maria T Fernández-Díaz. On the location of Li^+ cations in the fast Li-cation conductor $La_{0.5}Li_{0.5}TiO_3$ perovskite. *Angewandte Chemie International Edition*, 39(3):619–621, 2000.

[151] Yasuhiro Harada, Yuji Hirakoso, Hiroo Kawai, and Jun Kuwano. Order–disorder of the a-site ions and lithium ion conductivity in the perovskite solid solution $La_{0.67-x}Li_{3x}TiO_3$ (x= 0.11) 1. *Solid State Ionics*, 121(1-4):245–251, 1999.

[152] Yasuhiro Harada, Tsukasa Ishigaki, Hiroo Kawai, and Jun Kuwano. Lithium ion conductivity of polycrystalline perovskite $La_{0.67-x}Li_{3x}TiO_3$ with ordered and disordered arrangements of the a-site ions. *Solid State Ionics*, 108(1-4):407–413, 1998.

[153] Ainhoa Morata-Orrantia, Susana García-Martín, and Miguel Á Alario-Franco. Optimization of lithium conductivity in La/Li titanates. *Chemistry of materials*, 15(21):3991–3995, 2003.

[154] Takashi Teranishi, Michihiro Yamamoto, Hidetaka Hayashi, and Akira Kishimoto. Lithium ion conductivity of Nd-doped (Li, La) TiO_3 ceramics. *Solid State Ionics*, 243:18–21, 2013.

[155] Toyoki Okumura, Koji Yokoo, Tomokazu Fukutsuka, Yoshiharu Uchimoto, Morihiro Saito, and Koji Amezawa. Improvement of Li-ion conductivity in a-site disordering lithium-lanthanum-titanate perovskite oxides by adding LiF in synthesis. *Journal of Power Sources*, 189(1):536–538, 2009.

[156] S Stramare, V Thangadurai, and W Weppner. Lithium lanthanum titanates: a review. *Chemistry of materials*, 15(21):3974–3990, 2003.

[157] R Jaramillo, Sieu D Ha, DM Silevitch, and Shriram Ramanathan. Origins of bad-metal conductivity and the insulator–metal transition in the rare-earth nickelates. *Nature Physics*, 10(4):304, 2014.

[158] Jian Shi, You Zhou, and Shriram Ramanathan. Colossal resistance switching and band gap modulation in a perovskite nickelate by electron doping. *Nature communications*, 5:4860, 2014.

[159] Yoshiyuki Inaguma, Liquan Chen, Mitsuru Itoh, and Tetsurō Nakamura. Candidate compounds with perovskite structure for high lithium ionic conductivity. *Solid State Ionics*, 70:196–202, 1994.

[160] Yue Jin Shan, Yoshiyuki Inaguma, and Mitsuru Itoh. The effect of electrostatic potentials on lithium insertion for perovskite oxides. *Solid State Ionics*, 79:245–251, 1995.

[161] Zhen Zhang, Derek Schwanz, Badri Narayanan, Michele Kotiuga, Joseph A Dura, Mathew Cherukara, Hua Zhou, John W Freeland, Jiarui Li, Ronny Sutarto, et al. Perovskite nickelates as electric-field sensors in salt water. *Nature*, 553(7686):68, 2018.

[162] Zhaoyi Li, You Zhou, Hao Qi, Qiwei Pan, Zhen Zhang, Norman Nan Shi, Ming Lu, Aaron Stein, Christopher Y Li, Shriram Ramanathan, et al. Correlated perovskites as a new platform for super-broadband-tunable photonics. *Advanced Materials*, 28(41):9117–9125, 2016.

[163] Joshua L Hertz and Harry L Tuller. Measurement and finite element modeling of triple phase boundary-related current constriction in YSZ. *Solid State Ionics*, 178(13-14):915–923, 2007.

[164] Robert M Palomino, Eli Stavitski, Iradwikanari Waluyo, Yu-chen Karen Chen-Wiegart, Milinda Abeykoon, Jerzy T Sadowski, Jose A Rodriguez, Anatoly I Frenkel, and Sanjaya D Senanayake. New in-situ and operando facilities for catalysis science at NSLS-II: The deployment of real-time, chemical, and structure-sensitive x-ray probes. *Synchrotron Radiation News*, 30(2):30–37, 2017.

[165] Bruce Ravel. Atoms: crystallography for the x-ray absorption spectroscopist. *Journal of synchrotron radiation*, 8(2):314–316, 2001.

[166] Bruce Ravel and MATHENA Newville. Athena, artemis, hephaestus: data analysis for x-ray absorption spectroscopy using IFEFFIT. *Journal of synchrotron radiation*, 12(4):537–541, 2005.

[167] Georg Kresse and Jürgen Furthmüller. Efficient iterative schemes for ab initio total-energy calculations using a plane-wave basis set. *Physical review B*, 54(16):11169, 1996.

[168] Georg Kresse and D Joubert. From ultrasoft pseudopotentials to the projector augmented-wave method. *Physical Review B*, 59(3):1758, 1999.

[169] John P Perdew, Kieron Burke, and Matthias Ernzerhof. Generalized gradient approximation made simple. *Physical review letters*, 77(18):3865, 1996.

[170] AI Liechtenstein, VI Anisimov, and J Zaanen. Density-functional theory and strong interactions: Orbital ordering in mott-hubbard insulators. *Physical Review B*, 52(8):R5467, 1995.

[171] Michele Parrinello and Aneesur Rahman. Polymorphic transitions in single crystals: A new molecular dynamics method. *Journal of Applied physics*, 52(12):7182–7190, 1981.

[172] MP Allen and DJ Tildesley. Computer simulation of liquids oxford univ. press, 1987.

[173] Graeme Henkelman, Blas P Uberuaga, and Hannes Jónsson. A climbing image nudged elastic band method for finding saddle points and minimum energy paths. *The Journal of chemical physics*, 113(22):9901–9904, 2000.

[174] Graeme Henkelman and Hannes Jónsson. Improved tangent estimate in the nudged elastic band method for finding minimum energy paths and saddle points. *The Journal of chemical physics*, 113(22):9978–9985, 2000.

[175] Peter E Blöchl. Projector augmented-wave method. *Physical review B*, 50(24):17953, 1994.

[176] Peter E Blöchl, Ove Jepsen, and Ole Krogh Andersen. Improved tetrahedron method for brillouin-zone integrations. *Physical Review B*, 49(23):16223, 1994.

[177] H-G Von Ribbeck, M Brehm, DW Van der Weide, S Winnerl, O Drachenko, M Helm, and F Keilmann. Spectroscopic THz near-field microscope. *Optics Express*, 16(5):3430–3438, 2008.

[178] J García, J Blasco, MG Proietti, and M Benfatto. Analysis of the x-ray-absorption near-edge-structure spectra of $La_{1-x}Nd_xNiO_3$ and $LaNi_{1-x}Fe_xO_3$ perovskites at the nickel k edge. *Physical Review B*, 52(22):15823, 1995.

[179] Z Hu, MS Golden, J Fink, G Kaindl, SA Warda, D Reinen, Priya Mahadevan, and DD Sarma. Hole distribution between the Ni 3d and O 2p orbitals in $Nd_{2-x}Sr_xNiO_{4-\delta}$. *Physical Review B*, 61(5):3739, 2000.

[180] M Medarde, C Dallera, M Grioni, B Delley, F Vernay, J Mesot, M Sikora, JA Alonso, and MJ Martínez-Lope. Charge disproportionation in $RNiO_3$ perovskites (R= rare earth) from high-resolution x-ray absorption spectroscopy. *Physical Review B*, 80(24):245105, 2009.

[181] B Torriss, J Margot, and M Chaker. Metal-insulator transition of strained $SmNiO_3$ thin films: Structural, electrical and optical properties. *Scientific reports*, 7:40915, 2017.

[182] Xinyu Li and Nicole A Benedek. Enhancement of ionic transport in complex oxides through soft lattice modes and epitaxial strain. *Chemistry of Materials*, 27(7):2647–2652, 2015.

[183] Néstor E Massa, Aline Y Ramos, Helio CN Tolentino, Narcizo M Sousa-Neto, Jairo Fonseca Jr, and José Antonio Alonso. Temperature and high-pressure dependent x-ray absorption of $SmNiO_3$ at the Ni K and Sm L_3 edges. *Materials Research Express*, 2(12):126301, 2015.

[184] Dario Marrocchelli, Sean R Bishop, Harry L Tuller, and Bilge Yildiz. Understanding chemical expansion in non-stoichiometric oxides: Ceria and zirconia case studies. *Advanced Functional Materials*, 22(9):1958–1965, 2012.

[185] Dario Marrocchelli, Sean R Bishop, Harry L Tuller, Graeme W Watson, and Bilge Yildiz. Charge localization increases chemical expansion in cerium-based oxides. *Physical Chemistry Chemical Physics*, 14(35):12070–12074, 2012.

[186] Xingfeng He, Yizhou Zhu, and Yifei Mo. Origin of fast ion diffusion in superionic conductors. *Nature communications*, 8:15893, 2017.

[187] Akihiro Kushima and Bilge Yildiz. Oxygen ion diffusivity in strained yttria stabilized zirconia: where is the fastest strain? *Journal of Materials Chemistry*, 20(23):4809–4819, 2010.

[188] Bilge Yildiz. stretching the energy landscape of oxideseffects on electrocatalysis and diffusion. *Mrs Bulletin*, 39(2):147–156, 2014.

[189] Alan C Luntz, Johannes Voss, and Karsten Reuter. Interfacial challenges in solid-state li ion batteries, 2015.

VITA

Daw Gen Lim moved to West Lafayette, Indiana from Malaysia. He first received his Bachelor of Science Degree in Materials Engineering, with two minors in Economics and Nuclear Engineering, from Purdue University in May 2014. With his passion for sustainable energy, Daw Gen joined multiple energy storage and conversion related research group, starting with Dr. R. Edwin Garcias research group in computational modeling of Li-ion micro electrodes; Dr. Carol Handwerkers research group in developing hydrothermal synthesis of ZnO films; and Dr. Rakesh Agrawals research group on solution synthesis of CZTS/Se Kesterite based thin-film solar-cells.

Daw Gen is also a keen advocate for improving Asian STEM students participation on campus events and fostering cross-cultural understanding in the Purdue community; joining the Purdue Society of Asian Scientists and Engineers in its early days (2012 - 2013), as an internal marketing leadership trainee. As a highly motivated entrepreneur, Daw Gen and his team developed an innovative aluminum extrusion die cleaning method and participated in the 24th Burton D Morgan Business Plan Competition in 2014, winning 1st place in the Black Division.

August 2014, Daw Gen continued his PhD. in Materials Engineering at Purdue University. Joining Osswald Advanced Materials Group, and later Vilas Pol Energy Research group, working on various Li-ion and Na-ion electrochemical active materials and components ranging from: cathodes, thin-film solid state electrolytes, and anodes. He is guided by Adj. Prof. Sebastian Osswald, Prof. Vilas G. Pol, and Prof. Jeffrey P. Youngblood.